EFFECT OF SUPERIMPOSED PRESSURE ON DAMAGE EVOLUTION AND FRACTURE BEHAVIOUR OF AUTOMOTIVE ALUMINUM ALLOYS

EFFECT OF SUPERIMPOSED PRESSURE ON DAMAGE EVOLUTION AND FRACTURE BEHAVIOUR OF AUTOMOTIVE ALUMINUM ALLOYS

By

Jeff Gimple, B. Eng

A Thesis

Submitted to the School of Graduate Studies

In Partial Fulfillment of the Requirements

For the Degree

Masters of Engineering

McMaster University

Masters of Engineering
(Materials Science and Engineering)

McMASTER UNIVERSITY
Hamilton, Ontario

TITLE:	Effect of Superimposed Pressure on Damage Evolution and Fracture Behaviour of Automotive Aluminum Alloys
AUTHOR:	Jeff Gimple
SUPERVISORS:	Dr. D. S. Wilkinson and Professor J. D. Embury
NUMBER OF PAGES:	xix, 161

ABSTRACT

This study examined the damage evolution and fracture behaviour of two aluminum automotive alloys as a function of various material and testing variables. When applicable, the observations were plotted in stress-strain space in order to construct fracture mechanism maps as functions of pressure and temperature.

The influence of iron content was examined through the use of two different iron contents for each of the two alloy systems. For the solution hardened 5754 alloy, it was found that the presence of increasing iron content led to more rapid void nucleation, growth and coalescence which produced a decrease in ductility, and change in fracture mode from cup and cone to shear MVC. No change in fracture mode was observed with increasing iron content for the age hardenable 6111 alloy in the T4 temper. However, a decrease in ductility was observed. The low-Fe 6111 T6 alloy was found to fail intergranularly, while the high-Fe variant was observed to fail by shear MVC. It was proposed that this was the result of the grain refining effects of the increased iron content.

The evolution of damage was examined by performing uniaxial tensile test under superimposed hydrostatic pressure. In this way, the amount of damage generated within the sample during straining could be controlled and its effect on the fracture process examined. The application of pressure was found to decrease the amount of damage present in all samples tested and universally increased the observed ductility. When tested under sufficient pressure, it was found that the 5754 and 6111 T4 alloys would change fracture modes and fail by ductile rupture, with the damage processes suppressed or completely eliminated. Pressure was found to suppress the intergranular fracture mode in the low-Fe 6111 alloy, causing a transition to the shear MVC mode of failure.

The effect of temperature on the flow behaviour of the 5754 was also examined, as this alloy was found to exhibit the temperature sensitive Portevin Le Chatelier effect. The serrated yielding associated with the effect was found to be greatly reduced testing at 77 K, and grain scale and large scale shear processes within the material were observed to be almost completely eliminated. This was found to lead to large increases in uniform elongation, and a change in fracture mode from cup and cone to shear MVC for the low-Fe variant.

This thesis is dedicated to my fiancée Amy. For your love, support and patience throughout our many years together, I am and always will be in your debt. I would not be where I am today, without you.

Thank you.

ACKNOWLEDGEMENTS

I wish to express my sincerest gratitude to both my supervisors Dr. David Wilkinson and Dr. David Embury for their encouragement, advice and most of all their patience. Throughout the course of this thesis, you have helped me gain so much knowledge, experience and confidence, but most importantly you helped teach me to think. To do all this, and all the while keep a keen sense of humour is quite a feat.

Many thanks go out to Dr. John Lewandowski of Case Western Reserve University, for whom without his generous donation of time, equipment and guidance none of this work would have been possible. I would of course be remiss to neglect thanking Dr. Lewandowski's two graduate students whom made the experiments happen. A big thanks to Joel Larose and Nishad Prabhu. Good luck in your new career Nishad. Joel, I wish you luck as you endure another four years of grad school, though I'm sure the company of your girlfriend will help you survive. I wish you both the very best.

And lastly, but certainly not least a thanks to my friends, cohorts, and accomplices in A206. I couldn't have asked for better people to work, study and play with. You made the bad days better and good days great. You know who you are and I will miss you all very much, but not to worry, I am sure we will all get over it soon ☺.

Funding for the work carried out at McMaster University was provided by Alcan International, National Science and Engineering Research Council of Canada and McMaster University. Support for work at Case Western Reserve University provided by MTS fellowship (NP) and ONR-N00014-99-1-0327 (JL).

TABLE OF CONTENTS

LIST OF FIGURES

LIST OF TABLES

1 INTRODUCTION

In the current climate of environmental sensitivity, the demand for better performing vehicles, with higher fuel economy has led to an increase in the use of aluminum as an automotive material. This increase in demand has acted as the impetus for the study of the effects of alloy composition, heat treatment and stress-state on ductility as these factors have been shown to greatly affect the formability of some aluminum alloys. While many aluminum alloys have been successfully used in automotive applications (Burger, 1975), only two, AA 5754 and AA 6111 will be examined in this study. The AA 5754 alloy is a solution hardened alloy, offering moderate strengths, and is typically used in structural applications where its poor-post forming surface finish, a result of strain localization is not an issue. The age-hardenable AA 6111 alloy is primarily used for body panels where its combination of good formability, post heat treatment strength and surface finish are of value (Miller et al, 2000).

In the application of aluminum to automotive purposes, there is a desire to use recycled materials in an effort to reduce material cost and waste. Unfortunately, it has proven very difficult under typical recycling conditions to separate aluminum from other materials, particularly iron (Carle and Blount, 1999). The major problem with iron is that it is thermodynamically stable within the melt and cannot be removed (Spencer, 2000). At issue, is that the iron contaminant forms iron-aluminum intermetallics which have been shown to have a detrimental effect on ductility (Spencer, 2000; Sarkar, 2000), acting as a source of damage within the material, leading to potential difficulties for achieving good formability and consistent forming results. Adding to this problem, study of fracture processes of the alloys is made difficult by the rapid onset of failure, typically upon nucleation of only a few voids (Spencer, 2000).

The objective of this study was to characterize the damage evolution and fracture behaviour of both the 5754 and 6111 alloys. In order to accomplish this within the scope of these materials' application to the automotive industry, the effects of iron content, heat treatment and stress state were examined.

The study was setup with the goal of isolating these variables, such that their individual contributions to the fracture behaviour can be identified. Standard tensile samples were tested for both available iron contents, the variation representing approximately twice that expected to be seen in commercial production. In addition, samples of the 6111 alloys were tested in both the T4 and T6 conditions representing the range of strengths likely to be seen commercially. Lastly, samples of both iron contents, and when applicable, differing heat treatments were tested under the application of superimposed pressure in order to use stress state to identify the effects of damage on the fracture behaviour.

From these results models, encompassing the changes in both fracture mode and ductility were developed. This allowed the generation of fracture maps, based on true-stress true-strain, to be developed for specific alloy systems.

2 LITERATURE REVIEW

The following section will review the pertinent literature related to this study. It will be divided up into several sections which will cover the individual fracture modes and their characteristics for the materials, and then examine the effect pressure has on these fracture modes. In an effort to be concise, detailed presentation of specific models will be limited to those used within the discussion of the work.

2.1 MECHANISMS OF FRACTURE

2.1.1 Intergranular Fracture

Intergranular fracture is characterized by the propagation of cracks along grain boundaries. There are three primary mechanisms that typically cause intergranular failure. However, only the one observed in this study, localized ductile fracture along grain boundary precipitates will be reviewed.

In this failure mode, grain boundary fracture is initiated by the nucleation of voids at the grain boundaries. The resultant fracture surface appears macroscopically brittle, with the faceted appearance typically associated with the intergranular fracture mode. However, on the grain boundaries faces, sheets of coalesced voids are evident, indicating the process has an inherently local ductile component. This fracture is typically associated with aluminum alloys, and has been reported for several alloy systems including:

- Al-Zn-Mg (Ryder and Smale, 1963; Kawabata and Izumi, 1967)
- Al-Mg-Si (Evensen et al., 1975; Dowling and Martin, 1973; Vasudevan and Doherty, 1987)
- Al-Cu (Martin, 1982)

As the nucleation event requires some measure of local plasticity, this form of intergranular fracture can be effectively suppressed by any means which acts to homogenize slip in the material. This can include the refinement of the grain size, or the use of dispersoids (Evensen et al, 1975).

In the model presented by Evensen et. al (1975), an intergranular fracture criterion was derived under the assumption that failure will occur when a critical stress occurs at a grain boundary. The fracture condition was expressed as:

$$\sigma_{app} + \Phi(\sigma_{app} - \sigma_o) > \sigma_c \qquad \text{Eqn. 2.1}$$

where σ_{app} is the applied stress, Φ is a stress concentration factor and σ_o is the resistance to plastic flow which the precipitates exert. Assuming the stress concentration at the head of the slip band to be much greater than unity, Φ will be equal to $(L/W)^{1/2}$, where L is the length of the slip band, which corresponds to the grain size, and W is the width of the slip band. Then the fracture condition can be expressed as:

$$\sigma_{app} > \sigma_o + \sigma_c\left(W/L\right)^{1/2} \qquad \text{Eqn. 2.2}$$

This model predicts that finer grain scales act to suppress the intergranular fracture mode. In addition, by considering the precipitate resistance to slip, it implies that a peak aged material, will have a higher tendency to fail by intergranular fracture.

2.1.2 Ductile Fracture

The process of ductile fracture, also known as microvoid coalescence (MVC) is understood to occur due to the nucleation, growth and coalescence of voids associated with heterogeneities in the microstructure such as second phase particles (Puttick, 1959; Rogers, 1960). This failure mode is most commonly observed as a fibrous region in the center of a sample that has failed via cup and cone failure, or on the fracture surface of a specimen which has failed in shear due to MVC.

As there is typically a size distribution present among the second phase particle distribution, nucleation and growth of voids typically occur simultaneously, each contributing a specific amount of strain to the fracture process. However, due to the complexities of both these processes occurring simultaneously, most models of fracture processes consider each individually. Lastly, the final process of fracture, coalescence, adds a finite amount of strain to the fracture process such that the total fracture strain can be expressed as a sum of the strain contributions of all the fracture processes:

$$\varepsilon_f = \varepsilon_N + \varepsilon_g + \varepsilon_c \qquad \text{Eqn.2.3}$$

where ε_N is the nucleation strain, ε_g is the strain required to grow the voids from their initial size to the critical coalescence size, and ε_c is the strain associated with coalescence (though this tends to be negligible and is typically ignored).

2.1.2.1 Nucleation

The process of void nucleation has been shown to be the result of strain incompatibilities of the second phase particles and the matrix (Blum and Morrisey, 1966;

Palmer and Smith, 1966). The presence of these strain incompatibilities causes the generation of stresses around second phase particles which can result in nucleation of a void via decohesion of the particle/matrix interface, or cracking of the particle (Ashby, 1970). Decohesion is typically associated with small spherical particles (< 1μm), and cracking with larger or more elongated and angular particles.

Many models have been proposed to understand the nucleation process (Gurland and Plateau, 1963; Brown and Stobbs, 1971 and 1976; Goods and Brown, 1979; Tanaka et al., 1970; Ashby, 1966; Argon et al., 1975).

Gurland and Plateau (1963) considered nucleation in terms of an energy balance, where nucleation was assumed to occur when the elastic energy (ΔE_{el}) in the particle of radius R_o released by cracking or decohesion is equal to the work required to create the new surfaces associated with the void (ΔW):

$$\Delta E_{el} + \Delta W \leq 0 \qquad \text{Eqn. 2.4}$$

Gurland and Plateau took the values of ΔE_{el} and ΔW to be:

$$\begin{aligned} \Delta E_{el} &= \frac{1}{2} E\varepsilon^2 \frac{4}{3}\pi R_o^3 \\ \Delta W &= 4\pi R_o^2 \gamma \end{aligned} \qquad \text{Eqn. 2.5 and 2.6}$$

where E is the elastic modulus (assumed to be the same for particle and matrix), and γ is the work of separation of the interface and is taken as (Rosenfield, 1968):

$$\begin{aligned} \gamma &= \gamma_m + \gamma_p - \gamma_{mp} \quad &\text{(Dechosion)} \\ \gamma &= 2\gamma_p &\text{(Cracking)} \end{aligned} \qquad \text{Eqn. 2.7 and 2.8}$$

where m, p, and mp refer to matrix, particle, and matrix-particle respectively. This results in the expression for predicted nucleation strain:

$$\varepsilon_N = \frac{6\gamma}{ER_o} \qquad \text{Eqn. 2.9}$$

This model predicts the more accepted notion of strain being inversely dependent on particle size. Two earlier models by Brown and Stobbs (1971, 1976) indicated either an $R_o^{1/4}$ or no dependence, however this is opposite to what is typically seen experimentally. Several other models have been proposed based on incomplete nucleation around a particle (Goods and Brown, 1979), and strain energy calculations (Tanaka et. al, 1970).

What is important to note with all these criteria, is that when typical values are entered, they predict that the nucleation will be able to occur at strain typically on the order of yield strain when particles are larger than 25 nm, which for most situations of interest is typical (Tanaka et. al, 1970). This implies then, that the energy criterion while a required condition, is met early in almost all useful cases, and it is the critical local stress condition that can be regarded as limiting condition.

The local stress criterion considers decohesion, or particle cracking to take place when a critical local stress at the particle/matrix interface is met. For decohesion to occur, the critical local stress must exceed the particle/matrix interfacial strength (typically $\sigma_c \cong E/100$). A useful feature of a stress-based criterion is the ease at which the effects of hydrostatic pressures, both applied and induced by necking can be considered. Ashby (1966) examined nucleation for large particles using a dislocation model, where he assumed that complete plastic relaxation occurred by the punching out of dislocation loops around second phase particles. Interfacial stresses were thought to be generated due to the back stresses generated by the piling up of these dislocations. The local stress at the interface due to the pile-ups was expressed as:

$$\sigma_{loc} = \alpha \frac{\varepsilon R_o}{2kb} \qquad \text{Eqn. 2.10}$$

where α is a constant, k is the length of the dislocation pile up (typically taken as one half the inter-particle spacing (λ), b is the burgers vector. The nucleation strain can then be found to be:

$$\varepsilon_N = \frac{\sigma_c}{R_o} \frac{2kb}{\alpha} \qquad \text{Eqn. 2.11}$$

This model predicts the expected inverse relation between nucleation strain and particle size.

Argon et al. (1975), also examined nucleation for large particles, with a continuum approach being used which assumed the maximum interfacial stress would be generated from pure shear loading of the particle. The shear stress generated is found to be nearly equivalent to the strain dependant flow stress of the material, and hydrostatic stresses can be included via the addition of the mean stress (σ_m), so the local stress at the interface can be taken as:

$$\sigma_{loc} = Y\left(\bar{\varepsilon}_p\right) + \sigma_m \qquad \text{Eqn. 2.12}$$

where $Y(\bar{\varepsilon}_p)$ is the strain dependant flow stress. This model, however is limited to large particles (effectively particle size independent), and is not particularly useful in the current work.

Brown and Stobbs (1976) proposed a dislocation model, where relaxation was assumed to occur by secondary slip only. Work hardening is expected, and the local interfacial stresses are generated by dislocation pile-ups and hence will be proportional to the dislocation density:

$$\sigma_{loc} = \alpha\mu b\sqrt{\rho_l} \qquad \text{Eqn. 2.13}$$

where $\alpha \approx 1/7$, μ is the shear modulus of the matrix, and ρ_l is the dislocation density:

$$\rho_l = 1.7\frac{\varepsilon}{R_o b} \qquad \text{Eqn. 2.14}$$

This then gives a nucleation strain of:

$$\varepsilon_N \geq \frac{1}{30}\left(\frac{\sigma_{loc}}{\alpha\mu}\right)^2 \frac{R_o}{b} \qquad \text{Eqn. 2.15}$$

This however incorrectly implies a linear relationship between particle size and nucleation strain, contrary to what is most often seen.

The final model reviewed, is the one published by Goods and Brown (1979). This model examines the nucleation strain, by considering all the various contribution to the stress state, including the presence of superimposed hydrostatic pressure. The nucleation condition was given as:

$$\varepsilon_N^{1/2} \geq K(\sigma_c - \sigma_H) \qquad \text{Eqn. 2.16}$$

where K is a constant that is calculated for a given particle volume fraction and size and σ_H is the total hydrostatic stress, excluding the component due to the applied stress itself.

What is apparent from this review is that there are several important factors that can promote or deter the occurrence of void nucleation, and for a nucleation event to occur, two conditions must be satisfied. The first required condition is that the energy released by decohesion or particle cracking must be at least equal to the energy required to produce the new surfaces. The second condition requires that a critical stress be generated at the interface that is greater than the particle matrix interfacial strength to cause decohesion, or greater the fracture strength of the particle to cause particle cracking.

The models presented indicate that in general a larger particle should have a lower nucleation stress, though this appears to depend on the experimental system studied. For most systems, it is found that the energy criterion is met at strains of the order of those required for matrix yielding for particles larger than 25 nm, hence the critical stress condition can be considered to be the defining condition for nucleation. With this in mind, then large particle/matrix interfacial strength, extremely strong, small and non-angular particles will tend to delay nucleation to larger stresses, and hence larger strains, and conversely the opposite of these conditions will tend to promote the occurrence of nucleation. In addition, the presence of relaxation mechanisms promoted by high temperatures and spherical particles, and the reduction coarse slip in the matrix will help to reduce the occurrence of nucleation.

Of note, these models tend to consider only one size particle when defining a specific critical nucleation strain, however most materials will have a specific distribution of particle sizes, and hence a range of nucleation strains. Fisher and Gurland (1981) presented results, and produced a model which supports the idea of a range of nucleation strains corresponding to a specific distribution of particle sizes, and this should be taken into account when modeling actual materials.

2.1.2.2 Growth

Upon nucleation of a void, growth will ensue with further straining. This process has been modeled by several workers using continuum plasticity (McClintock, 1968; Rice and Tracey, 1969) for several different initial void geometries. The purpose of these models is to relate some value of damage, which can be taken as an area or volume fraction of voids, or a variation in sample density with the axial strain applied to the sample. Observations and determination of the value of damage is typically done by careful metallographic observation of longitudinal sections of deformed samples (Puttick, 1959; Gurland and Plateau, 1963; Palmer and Smith, 1966; Atkinson, 1973; LeRoy, 1978; Fisher and Gurland, 1981; Teirlinck, 1983), or by density measurements (Schmitt and Jalinier, 1982).

Gurland and Plateau (1963) performed an empirical analysis to examine the growth of an initially spherical void for a variety of materials. Their models assumes an initially spherical void which becomes ellipsoidal upon straining. They calculate the macroscopic strains associated with the void growth, by assuming the strain concentrations at the sides of voids (taken as the ratio of void elongation over specimen elongation) is proportional to the radius of curvature of the void, $R_c = b^2 / c$, Figure 2.1.

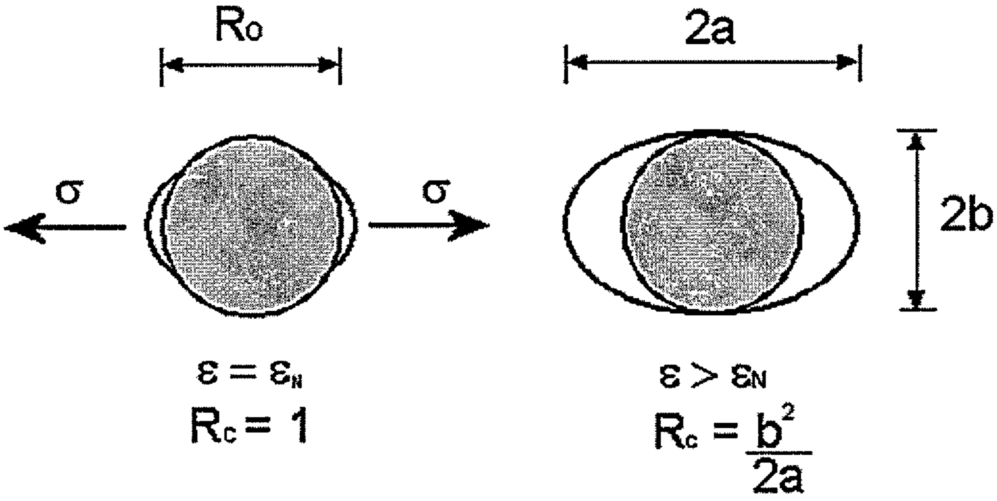

Figure 2.1: **Geometry for the Gurland and Plateau model of void growth. Adapted from Gurland and Plateau (1963).**

The major and minor axis of the growing voids can then be expressed as:

$$a = ka_0\left(\varepsilon^{2(\varepsilon-\varepsilon_N)} - 1\right)^{1/2}$$
$$b = R_0$$

Eqn. 2.17 and 2.18

where k is an adjustable parameter.

A simpler approach to void growth was taken by Ashby (1966), and later by Brown and Embury (1973). In their work, it was assumed that the void growth was proportional to the macroscopic strain. This, however simplistic, was apparently sufficiently accurate for the uniform tensile deformation of the systems being studied.

The growth of long cylindrical voids parallel to the tensile axis, Figure 2.2, was considered by McClintock (1968), through the study of a model system consisting of polystyrene spheres embedded in plasticene. He was able to show the strain at failure (defined by the moment of the on-set of void coalescence) could be expressed as:

$$\varepsilon_f = \frac{2}{\sqrt{3}} \frac{\ln F_f}{\sinh\left(\sqrt{3}\sigma_r / (\sigma_r - \sigma_z)\right)} \qquad \text{Eqn. 2.19}$$

where F_f is:

$$F_f = \frac{(D/\lambda)}{(D_o/\lambda_o)} \qquad \text{Eqn. 2.20}$$

where D_o is the initial void diameter, and λ_o is the initial void spacing. This model can be modified to examine cylindrical holes with elliptical cross-sections, Figure 2.2, in addition to adding the presence of work hardening:

$$\varepsilon_f = \frac{(1-n)\ln F_f}{\sinh\left((1-n)(\sigma_1 + \sigma_2)/(2\overline{\sigma}/\sqrt{3})\right)} \qquad \text{Eqn. 2.21}$$

where n is the strain hardening exponent and σ_1 and σ_2 are unequal stress components.

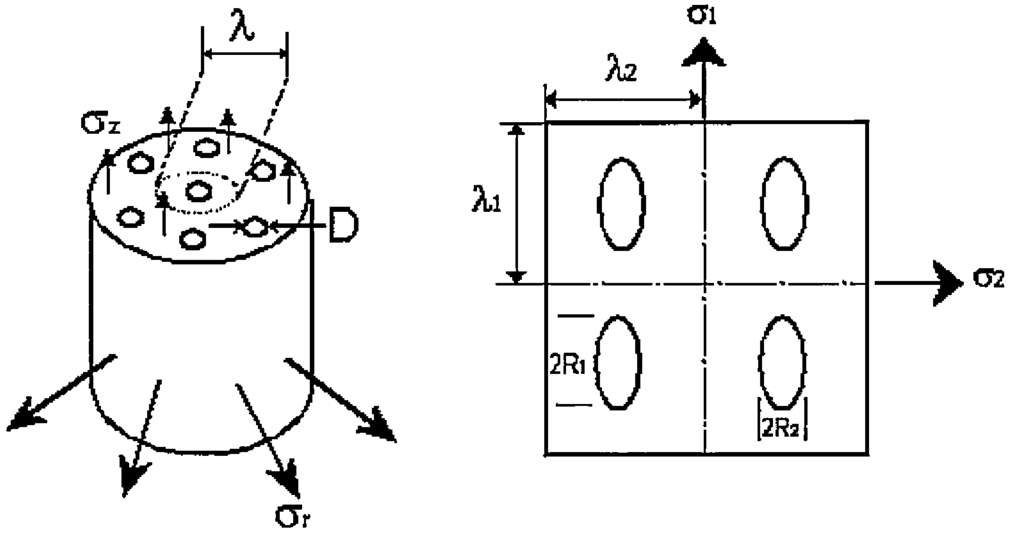

Figure 2.2: Growth of long cylindrical holes. Adapted from McClintock (1968).

A useful feature of this model is that it illustrates the dependence of void growth on the stress triaxiality, where the triaxiality is measured by the term:

$$\frac{\sigma_1 + \sigma_2}{\overline{\sigma}} \qquad \text{Eqn. 2.22}$$

Additionally, the presence of the hyperbolic sin term in Eqn. 2.21 indicates that work hardening will become important under conditions of high stress triaxiality.

The last model reviewed and probably the most realistic in terms of actual materials is from the work by Rice and Tracey (1969). In their model, Rice and Tracey considered the initial growth of an isolated spherical void of radius R_o, in a non-hardening material. The growth rate for this system was shown to have the form:

$$\dot{R}_i = R_o\left(\gamma\dot{\varepsilon}_i^{\infty} + \left(\tfrac{2}{3}\dot{\varepsilon}_j^{\infty}\dot{\varepsilon}_j^{\infty}\right)^{1/2} D\right) \qquad \text{Eqn. 2.23}$$

where

- $\dot{R}_i$ is the growth rate in direction i
- $\dot{\varepsilon}_i^\infty, \dot{\varepsilon}_j^\infty$ are the remote strain rates in direction i and j respectively
- γ is an amplification factor due to the strain at the edge of the voids which can be taken as:
  - $\approx 5/3$ for linear hardening, and low values of σ_m with non-hardening
  - 2 for high values of σ_m with non-hardening
- $D = 0.56 \sin\left(\frac{\sqrt{3}}{2}\frac{\sigma_m^\infty}{\tau_o}\right)$, where σ_m^∞ is the remote mean stress and τ_o is the shear yield stress

This model was considered for the case of uniaxial tensile deformation by Brown (1976), where he showed the integrated growth for the void was:

$$\Delta R_{II} = R_o\left(2 + 0.56\sinh\left(\frac{\sqrt{3}}{2}\frac{\sigma_m}{\tau_o}\right)\right)\Delta\varepsilon_p$$

$$\Delta R\perp = R_o\left(-1 + 0.56\sinh\left(\frac{\sqrt{3}}{2}\frac{\sigma_m}{\tau_o}\right)\right)\varepsilon_p \qquad \text{Eqn. 2.24 and 2.25}$$

where II and $\perp$ indicate parallel and perpendicular to the tensile axis respectively, $\Delta\varepsilon_p$ is the plastic strain increment, and σ_m the mean stress is taken as:

$$\sigma_m = \frac{1}{3}\sigma_{kk}^\infty = P \qquad \text{Eqn. 2.26}$$

where P is the remote hydrostatic pressure.

LeRoy (1978) considered the change in the amplification factor γ, where a spherical void is assumed to elongate initially at twice the rate of the matrix. He showed the void dimensions in an axisymmetric tensile test would be:

$$R_1 = R_0 \exp(D\varepsilon)\left[2\exp\left(\frac{3}{2}\varepsilon\right)-1\right]^{-1/3}$$

$$R_3 = R_0 \exp(D\varepsilon)\left[2\exp\left(\frac{3}{2}\varepsilon\right)-1\right]^{2/3}$$

Eqn. 2.27 and 2.28

where 1 and 3 refer to the tensile and radial directions respectively.

The process of void growth has been extensively studied and appears to be reasonably well understood. As long as the voids are sufficiently spaced so no interaction between stress fields associated with the voids occurs, models are available which can to a reasonable accuracy, predict the growth of voids.

From the models, two important factors affecting void growth are apparent:

1. The void expansion rate is proportional to the initial void size
2. High stress triaxialities will promote more rapid void growth

These factors are important as the first one is directly related to the microstructure of the material being studied, and the second factor is affected largely by the presence of superimposed hydrostatic pressures as will be discussed later.

2.1.2.3 Coalescence

Once nucleation and growth of voids has occurred within a sample, the process of void coalescence leading to the final fracture of the sample will eventually occur. As an upper limit, void coalescence can be considered to occur when two voids impinge on each other, which will be limited by the interparticle spacing (Rogers, 1960). Alternatively, coalescence can occur due to localization of the deformation to a single shear band between two voids (Palmer and Smith, 1966; Chin et. al., 1964; Baker and Charles, 1971; Brown and Embury, 1973), or local necking between voids can occur (Thomason, 1968, 1971, 1990). For alloys with 2 populations of void sizes, or a distribution of particle sizes, voids can nucleate at larger particles, and then linkage can occur though coalescence of voids formed at smaller particles within a shear band (Rogers, 1960; Broek, 1971).

It is useful to note that within the context of total failure strain which includes the contribution from the nucleation, growth and coalescence processes, the coalescence stage adds negligible strain, as coalescence is typically a rapid and catastrophic process (Blum and Morissey, 1966).

The simplest model of void coalescence was proposed by McClintock (1968). In this work, it was assumed that linkage of adjacent voids would occur when growing voids physically came into contact. However, this model tends to lead to large overestimation's of ε_f (Hancock and Mackenzie, 1976), as it ignores the possibility of localization between voids prior to contact, in addition to ignoring the interaction of the associated stress fields of closely spaced voids.

A geometric approach to void coalescence was taken by Brown and Embury (1973). Here, the linkage of voids was assumed to occur when the void length in the tensile direction equals the interparticle spacing.

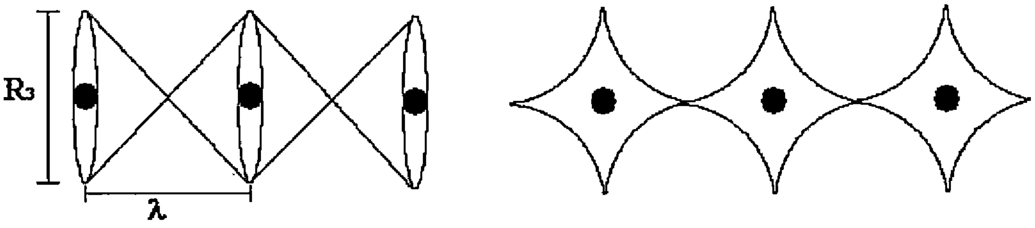

Figure 2.3: Geometry for the Brown and Embury void Coalescence Model. Adapted from Brown and Embury (1973).

where λ is the interparticle spacing and R_3 is the void length in the tensile direction. When the coalescence condition is met, they proposed that a 45° slip line field could be drawn between the voids, and the plastic constraint would be relaxed such that linkage could occur. The fracture strain then is a function of the growth strain which is the strain required to grow the void from its initial size (R_o) to the critical size ($R_3 = \lambda$) where the growth strain is assumed to be proportional to the macroscopic strain of the sample, and nucleation strain. The contribution of coalescence to the overall fracture strain is assumed to be negligible, and the result then is:

$$\varepsilon_f = \ln\left[\sqrt{\frac{\pi}{6f_v}} - \sqrt{\frac{2}{3}} + \varepsilon_N\right] \qquad \text{Eqn. 2.29}$$

where f_v is the particle volume fraction. Some important points this model elucidates is the dependence of the failure strain on the volume fraction of particles, where an increase in the volume fraction effectively decreases the interparticle spacing. The model does however assume a single nucleation strain, which is unrealistic for most materials, in addition to the assumption of the void growth strain being proportional to the macroscopic strain, which is also questionable. Nonetheless, the model was shown to be reasonably accurate for several systems including spheroidized steels and copper-silica alloys.

The approach taken by Thomason (1968, 1971, 1990) is to consider a material which deforms homogeneously until localization along a fracture path of voids becomes more energetically favourable. The localization process takes place via local necking between voids, where the failure condition is described by the following condition:

$$\frac{\sigma_n}{2k_n}\left(1+\sqrt{f_v}\right)^{-1} = \frac{\sigma_1}{2k} = \frac{1}{2} + \frac{\sigma_m}{2k} \qquad \text{Eqn. 2.30}$$

where σ_n is a critical value of mean stress to cause local necking, σ_m is the mean stress, k is the matrix shear yield strength, k_n is the shear yield strength of the intervoid matrix (assumed to equal k for $f_v < 0.01$), and σ_1 is the applied tensile stress. The advantage of this approach over the Brown and Embury (1973) model is the inclusion of the mean stress, which allows for coalescence to occur for $R_3 < \lambda$ for high σ_m.

Work by LeRoy extended the model of Brown and Embury by eliminating the assumption that the void growth strain is proportional to the macroscopic strain. LeRoy instead applied the Rice-Tracey model of void growth, to derive the following failure condition:

$$2R_3^f = \phi\lambda \qquad \text{Eqn. 2.31}$$

where R_3^f is the void dimension in the tensile direction from the Rice-Tracey model, ϕ is a constant taken as 1 for a spherical void and 2 for a long cylinder, and λ is the interparticle spacing.

Melander (1980) considered a 3-D distribution of voids in a work hardening matrix. By assuming the voids to have a softening effect on the matrix, the fracture condition can be taken as the instant when the work hardening of the matrix equals the softening effect of the voids, i.e. an instability condition similar to the Considère criterion. Or in terms of energy, when the energy consumption per unit effective strain no longer increases with effect strain, $\bar{\varepsilon}$:

$$\frac{d^2W}{d\bar{\varepsilon}} = 0, \qquad dW = \bar{\sigma} d\bar{\varepsilon} - \sigma_m d\varepsilon_{nn} \qquad \text{Eqn. 2.32}$$

where ε_{nn} is the macroscopic dilation or variation in volume. This model then attempts to apply a continuum approach to what is effectively a process controlled by microscopic factors such as particle spacing and void growth rate.

Two important aspects of the void coalescence process should be noted from this review. First, coalescence is heavily affected by the stress state around a void, where hydrostatic tension should increase the tendency to coalesce, while hydrostatic compression should conversely suppress coalescence. Secondly, the strain to failure will be dependent on the particle volume fraction, which effectively defines the interparticle spacing. In addition, when considering particle spacing, it should be remembered that most models only consider a uniform distribution of voids; however in most real systems, significant amounts of clustering will occur. In these cases it is useful to use the local volume fraction instead of a global average.

2.1.2.4 Ductile Fracture Failure Geometries

The final catastrophic failure can generate one of two final failure geometries, double cup and cone, or shear MVC. In the double cup and cone mode geometry, Figure 2.4, the fracture surface is characterized by a central portion within the "cupped" region, which contains ruptured voids. The remainder of the deformation is localized to the periphery of the fracture surface on shear lips, which are relatively smooth. This process typically occurs by a process of conjugate shear, or ductile cutting (Rogers, 1967). The fracture mode is initiated by the formation of a central void at the intersection of the conjugate shear bands. Once this void is formed, strain continues in the form of ductile cutting, which is effectively a form of ductile rupture.

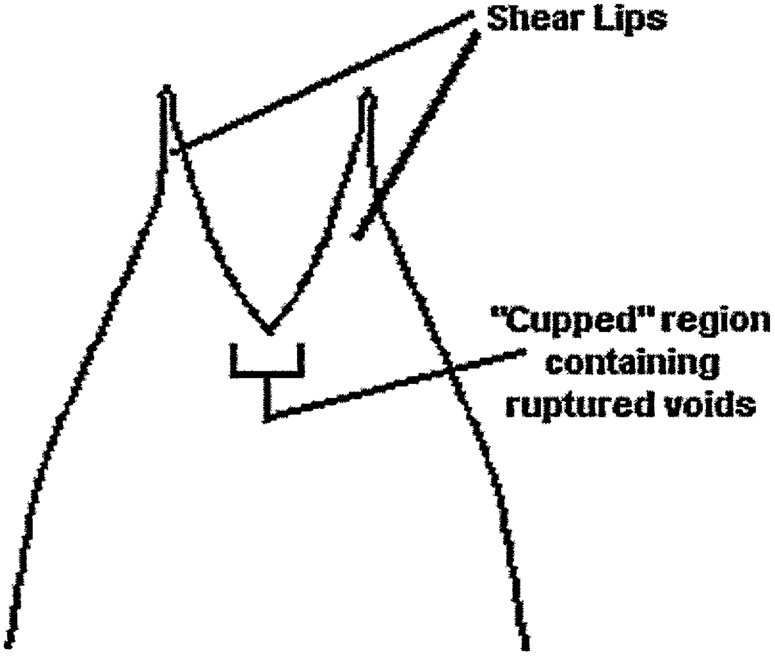

Figure 2.4: Schematic of the double cup and cone fracture geometry. Taken from Introduction to Ductility, Rogers, H.C. in "Ductility", 1967.

Alternatively, the material can fail via the shear MVC process, where the fracture surface is characterized by flat surface inclined 50 to 60° to the tensile axis. The surface will exhibit extensive sheets of voids that are elongated in the tensile direction. This process will supercede the double cup and cone geometry when certain microstructural conditions are met, the major one being an increased inclusion content. The presence of high inclusion content acts to localize the shear process at earlier strains, and has been described by McClintock (1967). In his work, he attempted to define a criterion, which predicts the termination of the ductile fracture process by localized shear. Two critical conditions required for the shift from homogenous flow to localized flow were identified. The first states that the loads for both modes must be equal. Once this condition is met, localization will then commence when the load for shearing becomes less than the load required for homogenous deformation. By equating the work required for homogenous deformation and for the inhomogeneous shear, for the geometry shown in Figure 2.5, an upper bound for localization was given as:

$$\left(1-\frac{\pi ab}{l_a l_b}\sqrt{\frac{2}{(1+a^2/b^2)}}\right)\Bigg/\left(1-\frac{4}{3}\pi\frac{a}{l_b}\left(\frac{b}{l_b}\right)^2\right)<\frac{\sqrt{3}}{2} \qquad \text{Eqn. 2.33}$$

where a and b are the major and minor void axis, l_a and l_b are the voids spacing perpendicular and parallel to the tensile axis respectively. From this analysis it is apparent that any increase in either the void size, through an increase in a or b, or a decrease in the void spacing, through a decrease in l_a or l_b will cause more rapid onset of shear localization. Both of these conditions will occur with increasing inclusion contents, hence are a significant contribution to the failure process.

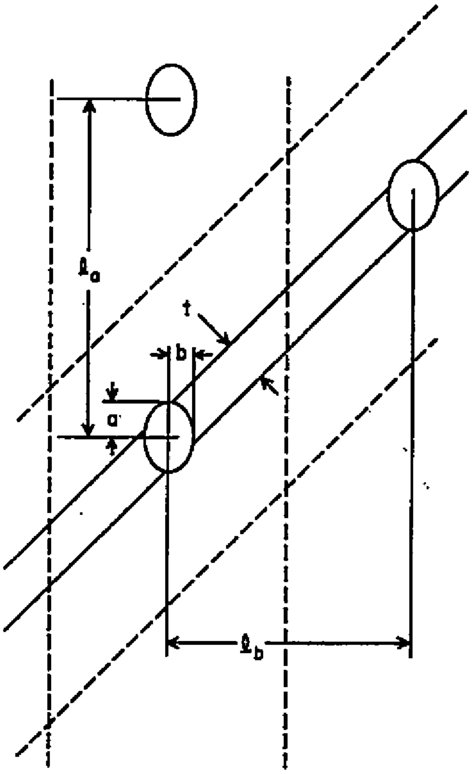

Figure 2.5: Geometry for localization to shear due to the presence of voids. Taken from McClintock, 1967.

In summary, the ductile fracture process can be divided into three stages: nucleation, growth and coalescence of voids. As most materials contain some distribution of particle sizes and spacing, the nucleation and growth processes are found to occur simultaneously, with large angular particles tending to fail or decohere first followed by smaller, less angular particles at increasing strains. Both of these processes are affected by the stress state around the particle, whereby a state of tension will promote them to occur at lower strains. At a critical void size and spacing, the process of coalescence will occur with the predominant variable being the actual spacing of the voids. However, a tensile state of stress triaxiality will also promote more rapid failure. This final failure process can occur via one of two geometries, cup and cone or shear MVC, depending on the microstructural features of the material tested.

2.1.3 Plastic Rupture

The plastic rupture mode of failure is characterized by a one hundred percent reduction in area at failure, where due to continued straining, the material geometrically necks down to a knife-edge or a point depending on the geometry of the sample. As damage mechanisms, cracking or shear instabilities will limit the ability of a material to rupture, plastic rupture can be considered to be the predominant mode when all other mode are suppressed. Plastic rupture has been observed in several situations:

- High purity metals where there are few inclusions present to nucleate voids
- Deformation at high temperature where dynamic recovery and recystallization mechanisms can occur (Ghandi and Ashby, 1979)
- When large hydrostatic pressures are superimposed, nucleation of voids and cracks will be suppressed allowing plastic rupture to occur (Bridgman, 1952; Pugh and Green, 1964; French and Weinrich, 1975)

2.2 THE EFFECT OF PRESSURE ON FLOW BEHAVIOUR AND FRACTURE

2.2.1 General Flow Behaviour

Through the application of superimposed imposed hydrostatic pressure, significant changes in ductility and fracture can occur. In understanding pressure effects, it is useful to follow the approach taken by Lewandowski and Lowhaphandu (1998) in their review on the effects of pressure on the mechanical behaviour and deformation of materials.

In their review, the entire stress-strain history of the sample was divided into two conditions, those present before and those present after necking. Before necking, the sample will be deforming due to the motion of dislocations in response to an applied stress, whereby plastic deformation will occur when the effective stress ($\bar{\sigma}$) is greater than the yield strength and the effective stress is given by:

$$\bar{\sigma} = \frac{1}{\sqrt{2}}\left[(\sigma_1 - \sigma_2)^2 + (\sigma_2 - \sigma_3)^2 + (\sigma_3 - \sigma_1)^2\right]^{1/2} \qquad \text{Eqn. 2.34}$$

where σ_1, σ_2, and σ_1, are the principal stresses. For isotropic materials, defined as those having homogenous microstructures, with low inclusion contents and no differences in shear modulus with crystallographic orientation, the presence of the superimposed pressure, described by $\sigma_1 = \sigma_2 = \sigma_3$, will generate no additional shear stresses and thus will not effect the yielding behaviour. However, if a material deviates from the isotropic conditions defined above, then superimposed pressure can cause significant changes in yielding and flow behaviour. This typically occurs in composites or materials with very high inclusion contents, where the differences in the compressibility between the matrix and reinforcement or inclusions can generate dislocations and cause local work hardening of the material. This can also occur as a result of anisotropy of the elastic constant, where the pressure may induce shape changes. For isotropic materials, specifically most monolithic metals such as those studied in this work, no appreciable difference in yielding and flow behaviour will be caused by the application of hydrostatic pressure, Figure 2.6.

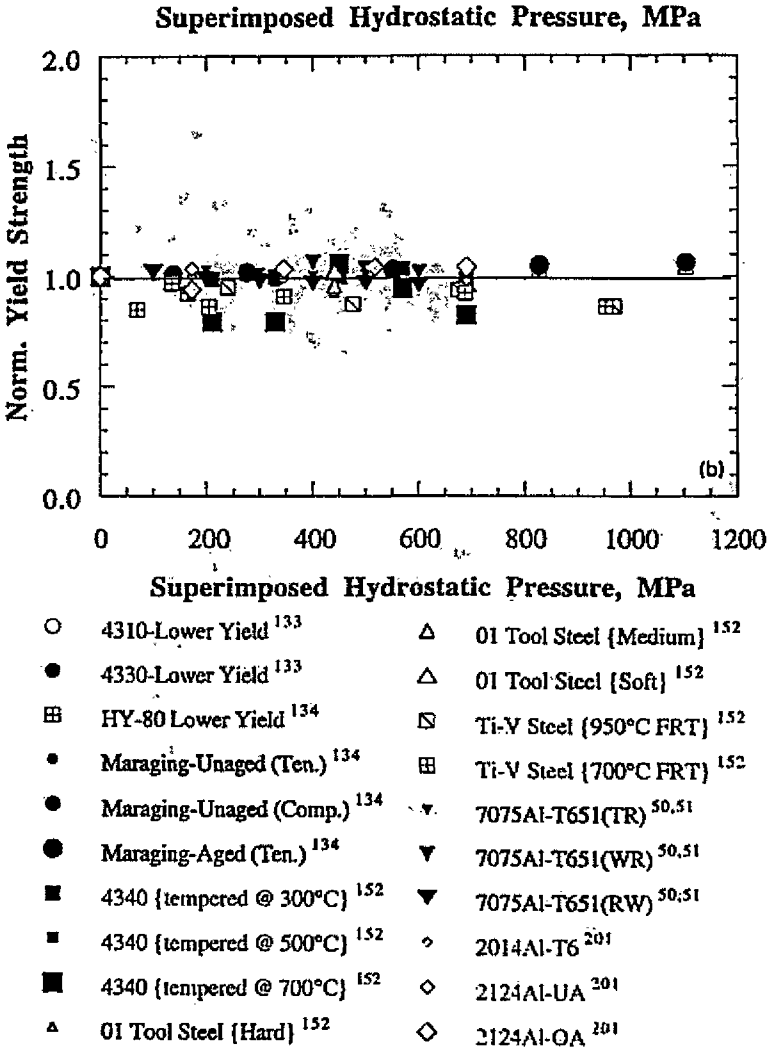

Figure 2.6: Influence of pressure on the normalized yield strength of materials. The horizontal line represents pressure independent flow (Lewandowski and Lowhaphandu, 1998).

After necking, the stress state in a material becomes one of triaxial tension, where the triaxiality can be described according to the work of Bridgman, (1952). The stress-state of the material then becomes a function of both the effective stress due to the applied tensile load in addition to the necking induced triaxial tension. Thus, with the development of the triaxial tension, the application of superimposed pressure will act to reduce its magnitude and may completely eliminate or reverse its presence. This is of considerable importance, as most modes of failure are dilatant processes, hence will have some dependence, often significant, on the presence of triaxial tensions, where typically these will act to accelerate failure.

2.2.2 Intergranular Fracture

Pressure has been shown to have a significant effect on intergranular failure, depending on whether the failure is nucleation or propagation-controlled (Lewandowski and Lowhaphandu, 1998). As nucleation controlled brittle fracture is yield dependent, pressure should not have a significant effect. However, in considering the work of Evenson et. al (1975) presented earlier where intergranular fracture was initiated by void formation but was propagation controlled, the initial nucleation events are dilatant and hence will be pressure dependent. Therefore in general nucleation-controlled cracking is independent of the presence of superimposed pressure. However, in some limited circumstances, where the initial crack initiation is dilatant, pressure can have a significant effect. For propagation-controlled intergranular failure, it has been shown that many alloy systems fail when a critical maximum principal stress is met.(Knott, and Cottrell, 1963; Knott, 1966a; Knott, 1966b; Knott, 1967). Where the failure condition can be described by:

$$\overline{\sigma} = \sigma_f + P \qquad \text{Eqn. 2.35}$$

where $\overline{\sigma}$ is the effective stress, σ_f is the brittle fracture stress in tension and P is the superimposed pressure, indicating a strong dependence of fracture on the level of superimposed pressure applied. In many instances, more than one mode of failure is available to a straining material. For example a material in tension may be able to fail intergranularly, by MVC shear or by ductile rupture, with each of these modes governed by a critical stress state. As the process of intergranular fracture is affected to a different degree by the presence of superimposed pressure than other process, at sufficient pressures the effective stress required for intergranular fracture can be increased such that intergranular fracture can no longer occur, because a different fracture mode with a lower required stress may occur.

2.2.3 Ductile Fracture

The fracture strain of many ductile metals, including aluminum alloys, have been shown be very dependent on the presence of superimposed hydrostatic pressure, (Figure 2.7), primarily due to the inherent dilatancy of the nucleation, growth and coalescence of voids associated with the ductile fracture process.

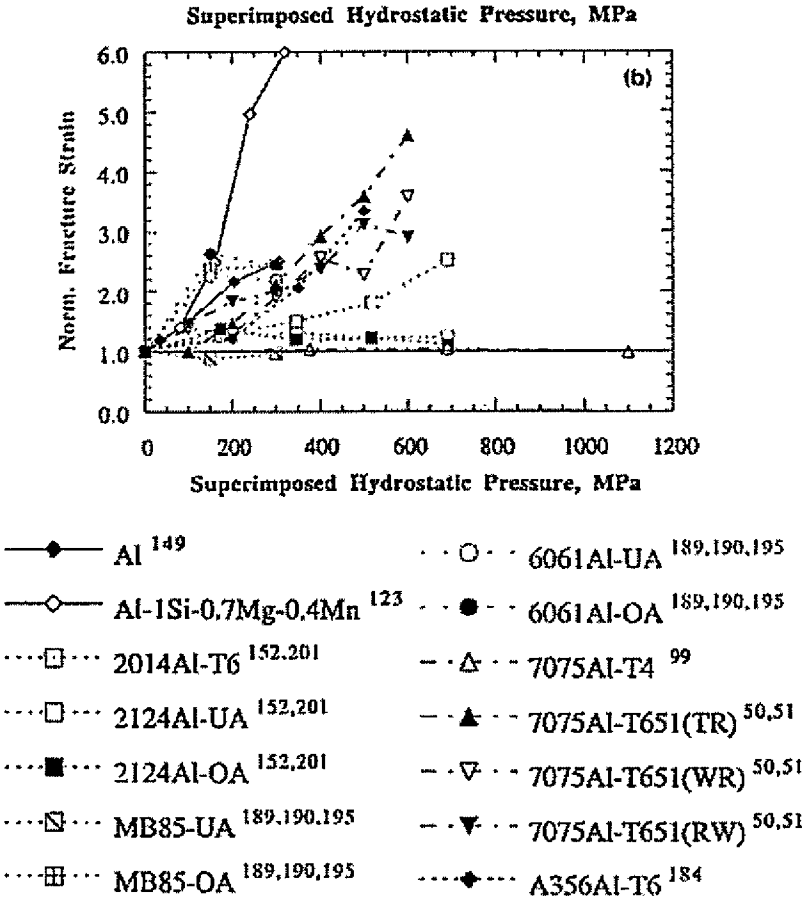

Figure 2.7: Influence of pressure on the normalized fracture strain of materials. The horizontal line represents pressure independent flow. Taken from Lewandowski and Lowhaphandu, 1998.

In their review of the nucleation of voids around second phase inclusions, Goods and Brown (1979), the critical condition for void nucleation is taken to occur when all the stresses contributing to the particle cracking or particle/matrix decohesion are greater than the particle strength, or the particle/matrix interfacial strength:

$$\sigma_c + \sigma_f + \sigma_H > \sigma_I$$

Eqn. 2.36

where σ_c is the local stress acting to open the interface, σ_f is the flow stress, σ_H is the hydrostatic tension (or compression, where tension is taken as positive), and σ_I is the particle/matrix interfacial strength or particle fracture stress. Several workers have confirmed this pressure dependence experimentally for spheroidized steel, Figure 2.8.

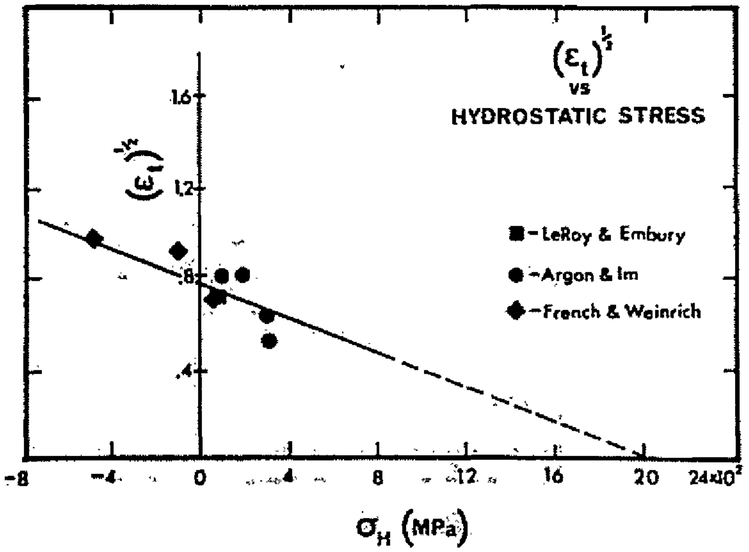

Figure 2.8: The effect of pressure on the void nucleation strain for spheroidized steels. Taken from Goods and Brown, 1979.

In examining the growth of voids Brown (1976) considered the Rice-Tracey model (1969) for the case of uniaxial tension, where he showed the integrated growth for the void was:

$$\Delta R_{II} = R_o\left(2 + 0.56\sinh\left(\frac{\sqrt{3}}{2}\frac{\sigma_m}{\tau_o}\right)\right)\Delta\varepsilon_p$$

$$\Delta R\perp = R_o\left(-1 + 0.56\sinh\left(\frac{\sqrt{3}}{2}\frac{\sigma_m}{\tau_o}\right)\right)\varepsilon_p$$

Eqn. 2.37 and 2.38

where II and ⊥ indicate parallel and perpendicular to the tensile axis respectively, $\Delta\varepsilon_p$ is the plastic strain increment, and σ_m the mean stress is taken as:

$$\sigma_m = \frac{1}{3}\sigma_{kk}^{\infty} = P \qquad \text{Eqn. 2.39}$$

where P is the remote hydrostatic pressure. Then under the presence of superimposed pressure, the growth of voids will be significantly retarded, and at sufficient pressures the mean stress term can become dominant in that the growth rate is effectively reduced to zero.

In the case of ductile fracture, it must be remembered that the two modes discussed earlier are both inherently ductile, where the major difference separating them is the geometry of the final void coalescence, where in cup and cone failure coalescence occurs perpendicular to the tensile axis while in shear MVC it occurs at some angle (~45°). Thus, for these modes of ductile failure, where final fracture is dependant on the attainment of a critical level of damage, pressure will act to delay or completely eliminate the nucleation and growth of voids, such that greater ductility's will be observed.

In this sense, the case of ductile rupture can then be considered as only a special case of ductile fracture, where the presence of superimposed pressure acts to suppress the conditions necessary to allow the sufficient nucleation and growth of voids required for coalescence to occur. Hence, the sample is forced to neck down to a point in the case of a round specimen or a knife-edge in the case of a flat specimen.

3 EXPERIMENTAL PROCEDURES

3.1 MATERIALS

Two aluminum alloys were studied in this work. The first is a solution hardenable 5754 alloy, and the second is an age hardenable 6111 alloy. For each alloy, two iron contents were examined, where these contents represent approximately one half to twice the contents expected to be encountered in commercial production. The specific compositions and designations used for this work are shown in Table 3.1 and Table 3.2.

Table 3.1: Chemical Composition: 5754 in weight %

Designation	Mg	Mn	Si	Fe	Ti
Low Fe	3.21	0.20	0.066	0.08	0.010
High Fe	3.24	0.21	0.055	0.30	0.011

Table 3.2: Chemical Composition: 6111 in weight %

Designation	Si	Cu	Mg	Fe
Low Fe	0.66	0.69	0.70	0.06
High Fe	0.63	0.69	0.70	0.68

The materials were received in the form of 2mm sheet. The 5754 alloys were annealed via a 2 hour soak at 340°C and air cooled resulting in an "O" temper. The 6111 alloys were studied in both the naturally aged (T4) and peak aged (T6) condition. To achieve this, the material was first resolutionized at 560°C for 20 min to dissolve age hardenable particles, then quenched to form a solid solution. Naturally aging occurs by allowing the material to sit at room temperature for 7-10 days (Esmaeli et al., 1999). For the T6 condition, the annealed material is artificially aged at 180°C for 8 hours (Brooks, 1991; Esmaeli et al., 1999).

3.2 STANDARD TENSILE SAMPLES FOR ATMOSPHERIC PRESSURE TESTS

Both alloys were characterized in uniaxial tension at atmospheric pressure. The 6111 alloys were machined in the rolling direction according to Figure 3.1.

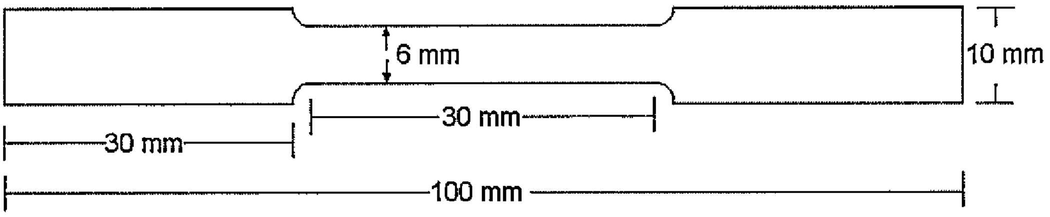

Figure 3.1: Standard Tensile Sample.

The 5754 alloy was machined to a smaller sample size, Figure 3.2 due to a lack of available material, and due to the requirement for samples of these dimensions for use in the high pressure tensile rig.

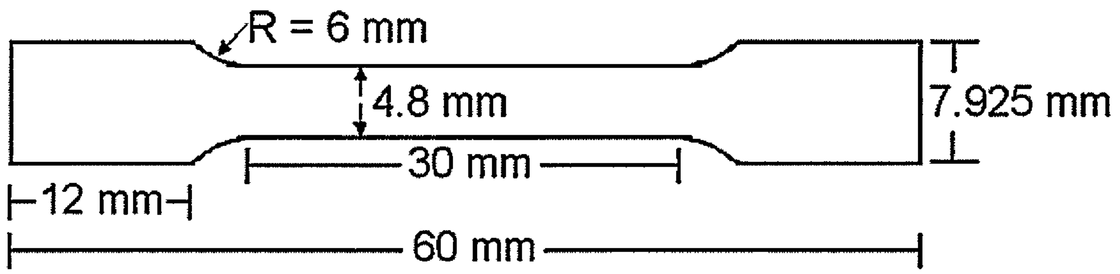

Figure 3.2: 5754 Hydrostatic Test Sample Dimensions.

Ambient pressure tests were conducted on a hydraulic test machine at a strain rate of 0.3 mm/min. Strain measurements were made using a clip-on extensometer with a 12.5 mm gauge length.

In addition to the tests conducted at ambient pressure (0.1 MPa) and temperature (~298 K) tests, the 5754 alloys were also tested at 77K (liquid nitrogen) in order to examine the effect of temperature on the serrated yielding (Portevin-Le Chatelier Effect (PLC)) and work hardening of these alloys. The testing procedure was the same as ambient pressure testing with the exception that samples were submerged in liquid nitrogen throughout the test.

3.3 TENSILE TESTING UNDER SUPERIMPOSED HYDROSTATIC PRESSURE

In an effort to study the effects of damage on fracture behaviour, tensile tests were conducted under superimposed hydrostatic pressure on a rig located at Case Western Reserve University in Cleveland, Ohio. By testing under superimposed pressure, the amount of damage formed within the sample can be controlled, and the ductility increased.

High pressure tensile samples we prepared for both the 5754 and 6111 alloys per Figure 3.2.

Pressure is applied to the samples via compressed Argon gas. The argon is pressurized through the combination of a compressor and intensifier system, and is pumped into a triple walled pressure vessel containing the sample which is held in a set of grips. One grip is locked to the pressure vessel, while the other end is attached to the hydraulic tensile actuator such that tension can be applied. Pressures available with this rig range from 0.1 (ambient) to 500 MPa.

The tests were conducted at a strain rate of 0.03 mm/s. Extension of the samples was measured via crosshead motion, as there were no strain gauges capable of operating within this rig.

3.4 REDUCTION IN AREA (RA) MEASUREMENTS

As no strain gauge measurements were available for the tests conducted under superimposed pressure, in addition to the difference in sizes of the samples tested, no direct comparisons of materials ductility in terms of sample elongation could be made. For these reasons, ductility was measured via the reduction in area of the samples fracture surface.

A fractured end of the sample was first cut off the broken tensile specimen and mounted for SEM examination, being careful that the sample is cut perpendicular to the tensile directions so that viewing occurs directly down the tensile axis of the sample. A digital image of the fracture surfaces was taken, Figure 3.3, and analyzed using the

UTHSCSA ImageTool for Windows Version 2.0 image analysis software. Reduction in area was taken as:

$$RA = \left(\frac{A_i - A_f}{A_i} \right) \times 100 \qquad \text{Eqn. 3.1}$$

where RA is given in as a percent (%). In the case of samples which necked down to a knife edge, , the reduction in area was taken as 100%, Figure 3.4.

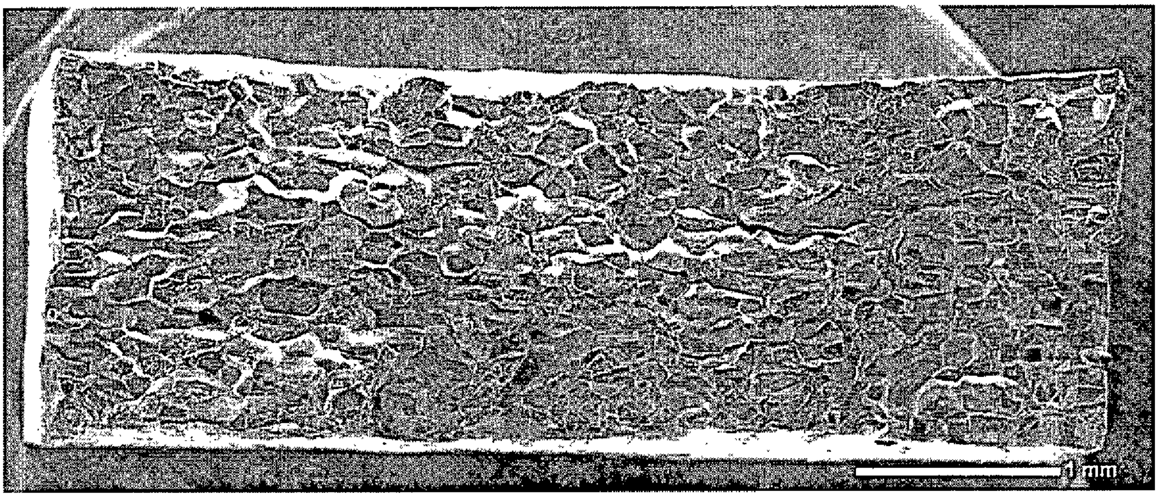

Figure 3.3 SEM image of sample taken for reduction in area measurement.

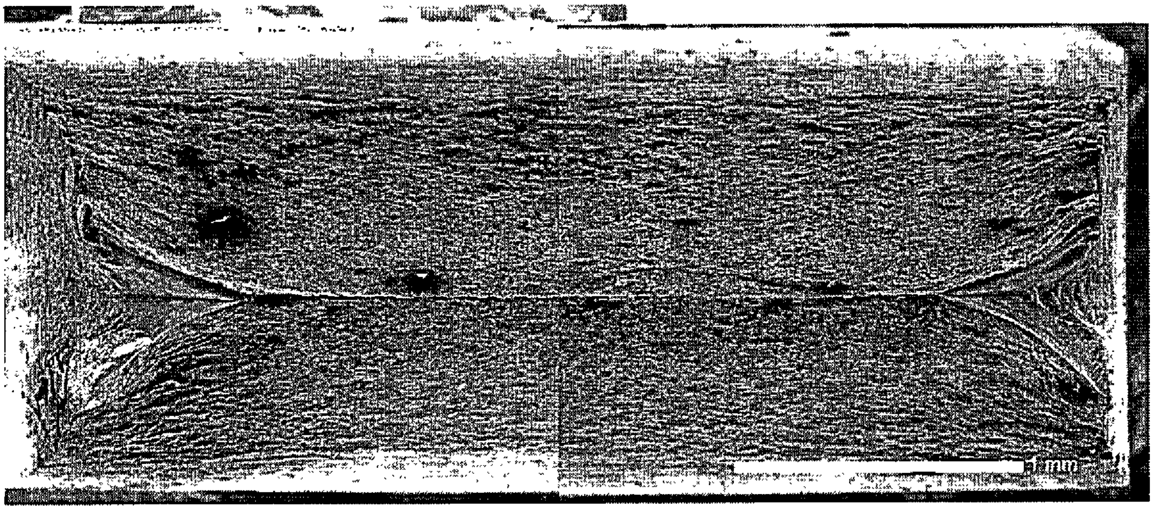

Figure 3.4 Sample which has necked to a knife edge, 100% RA.

3.5 DETERMINATION OF FRACTURE MODE

In order to understand the effect of iron content, damage and heat treatment on fracture behaviour, the fracture surfaces of all the samples tested were examined under the SEM to determine the fracture mode. The specimens used for this purpose were the same ones used for the reduction in area measurements.

3.6 DAMAGE MEASUREMENTS

In order to measure damage, fractured tensile samples were sectioned down their centreline. This was done using a wire EDM in order to ensure no additional damage was formed due to the cutting process. These sections were mounted in epoxy and then wet ground using a 1200 SiC paper to expose the metal surface. Polishing was accomplished with a 15 μm natural diamond slurry, followed by a 3μm natural diamond slurry. Polishing with colloidal silica produced the final mirror finish. The samples were then demounted by dissolution of the mount material in dichloromethane, and then remounted on SEM stubs for SEM examination. Digital images of the samples were taken, starting at the region of the fracture, and then back at regular intervals such that damage as a function of distance from the fracture surface could be obtained.

In order to make damage measurements, the photos of the damaged sections were first edited using Paint Shop Pro Version 7.02 to form a composite image, Figure 3.5. This was then sectioned into smaller images at regular intervals away from the fracture surface. Any colour corrections to the image or removal of artifacts was done at this point. These smaller images were then imported into the image analysis software, and analyzed using standard thresholding methods. Area fraction analysis was performed to measure the area fraction of damage. As can be seen in Figure 3.5, the contrast between the voids, and the matrix/particles was quite good, and only minor brightness and contrast corrections were required, typically only to correct for brightness and contrast variations due to the use of multiple images in the composite.

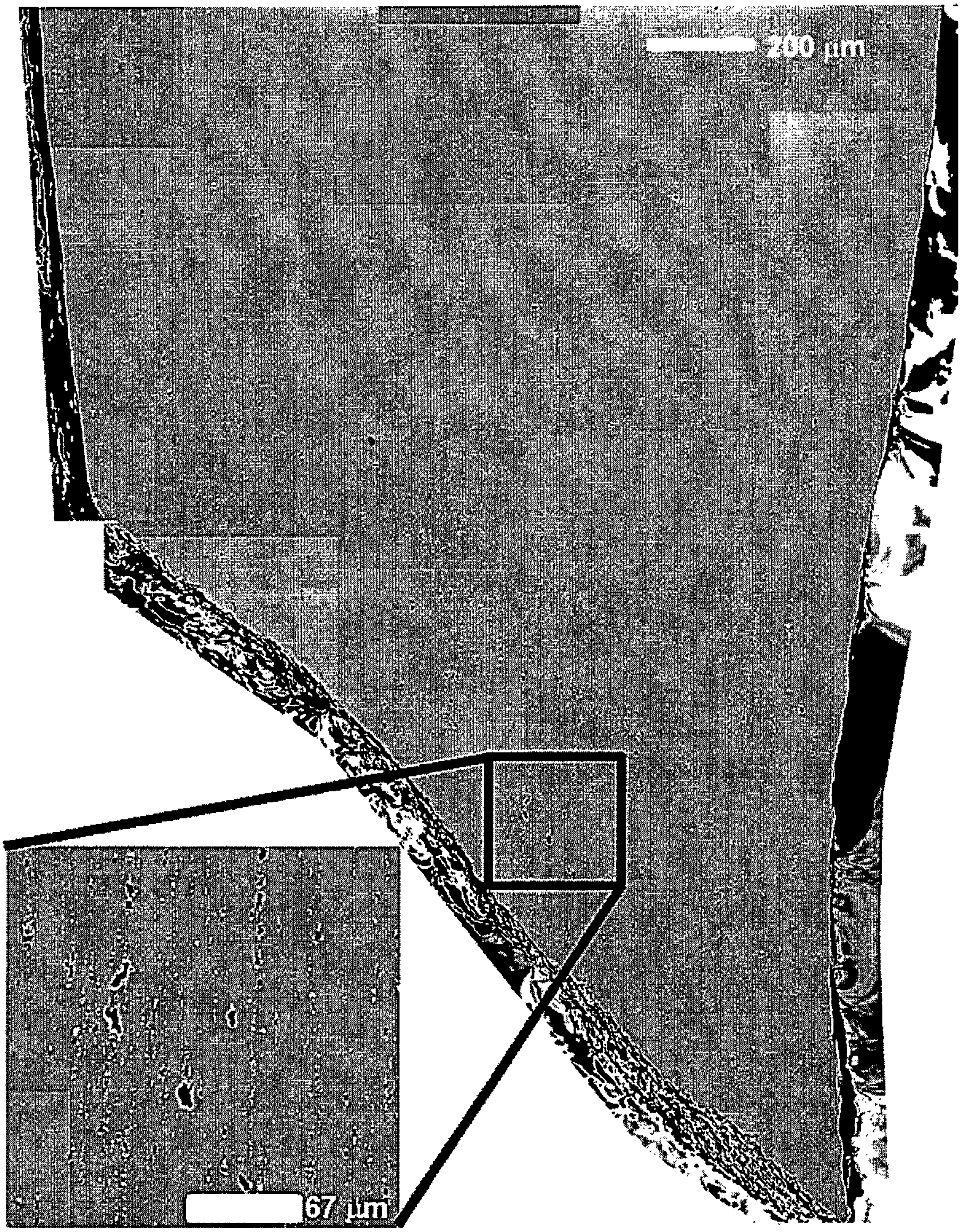

Figure 3.5 Composite image used for damage analysis, with magnified area showing contrast between voids and the particle/matrix, and good resolution.

In addition, low magnification images were taken to produce a composite photo of the entire necked region for the purpose of measuring the necking strains and strain gradients adjacent to the fracture surface, Figure 3.6.

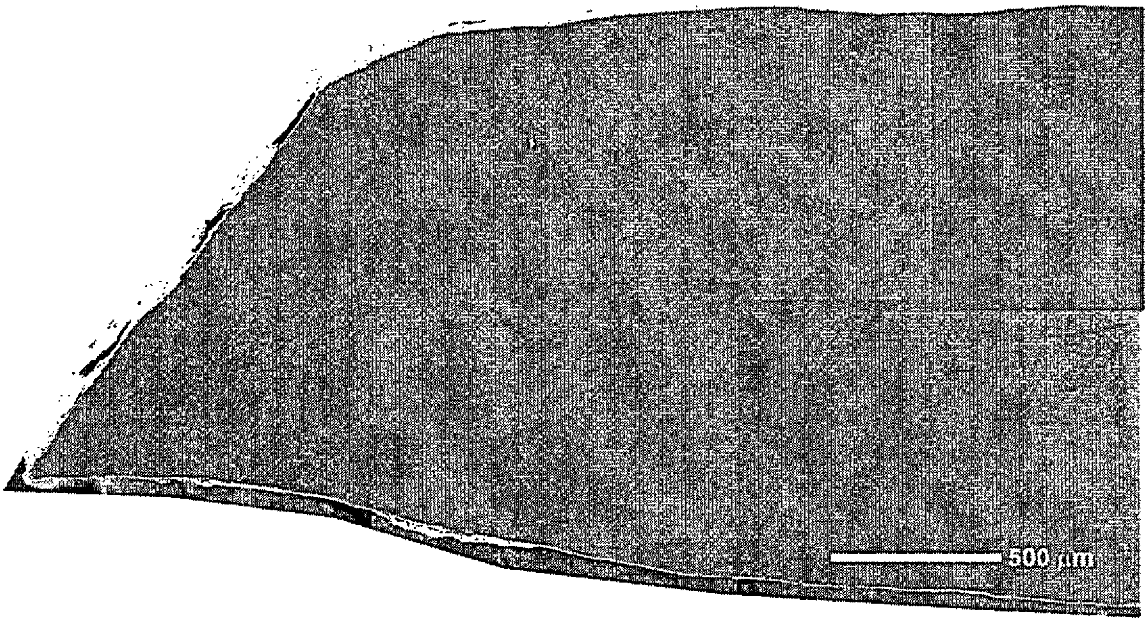

Figure 3.6 Composite photo used for measurement of necking strains.

As the other half of the fractured sample was unavailable to form a complete image of the necked area (it was being used for necking and fracture mode fractography), the original photo was flipped and mirrored to form a new image. This was then lined up with the original to form a complete neck in order to measure the post-necking strains, Figure 3.7.

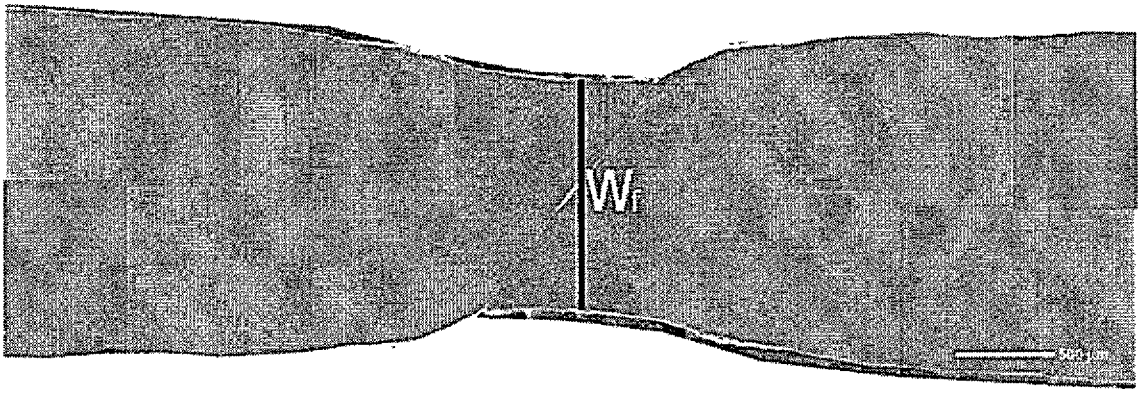

Figure 3.7 Example of image used in necking measurements.

The post-necking strain was then taken to be:

$$\varepsilon_n = \frac{W_i - W_f}{W_i} \qquad \text{Eqn. 3.2}$$

where W_i is the initial sample width, and W_f is the measured width at a given point on the neck.

3.7 ETCHING FOR SHEAR BANDS

In order to identify regions of intense shear, samples were etched via one of two methods. The 5754 alloys received a shear decorating treatment. Polished samples mounted in Bakelite were aged for 14 days at 90° C after the work of Spencer (Spencer, 2000). This allows precipitation of Al-Mg intermetallics in regions of intense deformation, namely the slip and shear bands. Upon completion of the aging treatment, the sample is etched in order to preferentially reveal the precipitates, such that regions of shear are clearly delineated, Figure 3.8. This etching is accomplished by holding the sample in 15% H_3PO_4 at 60° C for 1 to 1.5 minutes.

The Mg content of the 6111 alloys is insufficient for the aging treatment to be used effectively, therefore these sample where etched and viewed under polarized light instead. The samples were first mounted in bakelite and polished. They were then etched for 60 s in Keller's reagent, followed be 15 s in 50% HNO_3. The slip and shear bands can then be revealed through the use of Nomarski Differential Interference Contrast. This method works by accentuating small differences in height that would otherwise be unobservable on a bright-field microscope. As the slip and shear bands are preferentially etched over other regions of the matrix, these are readily resolved, Figure 3.9.

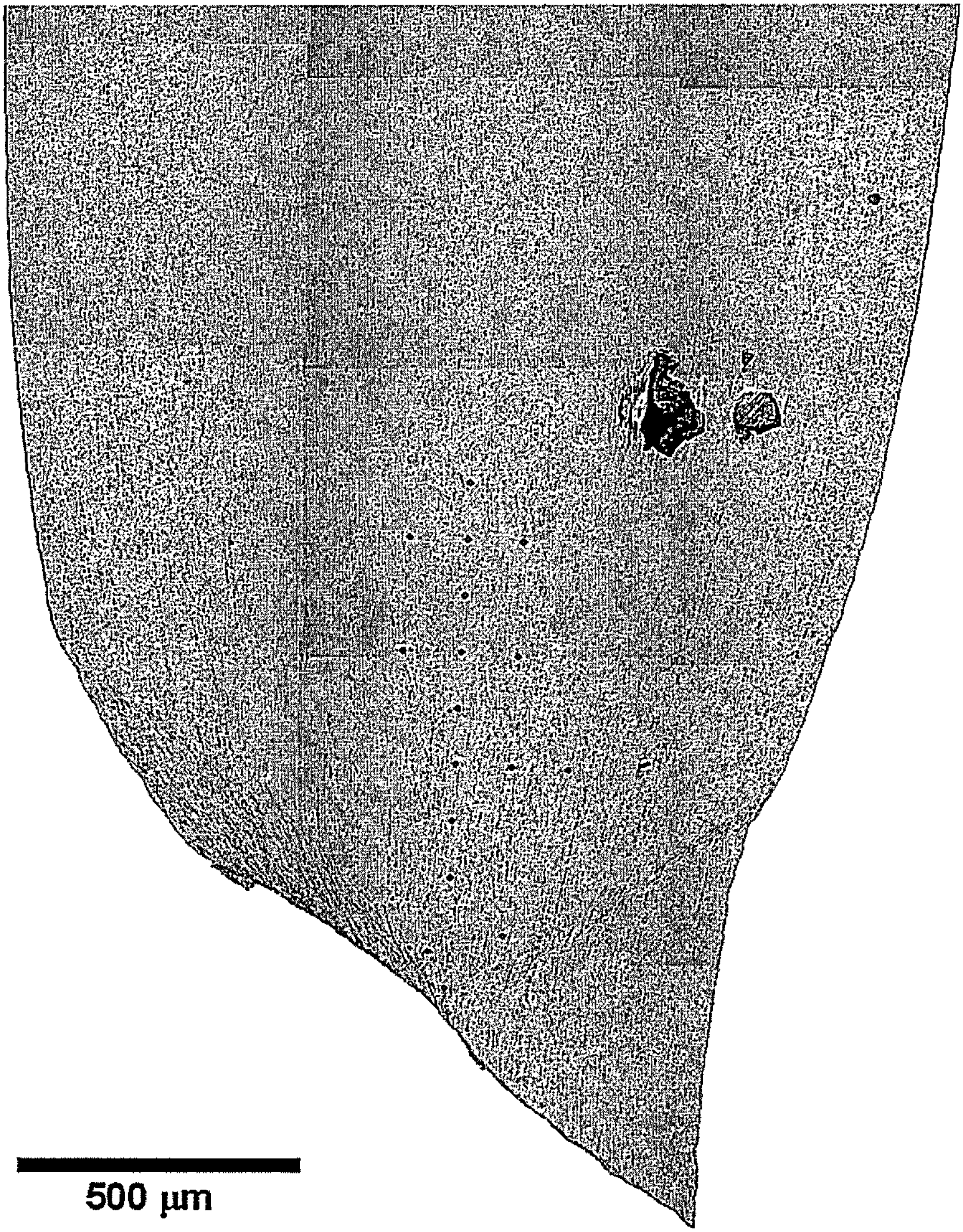

Figure 3.8: Composite image of a 5754 alloy etched to reveal shear.

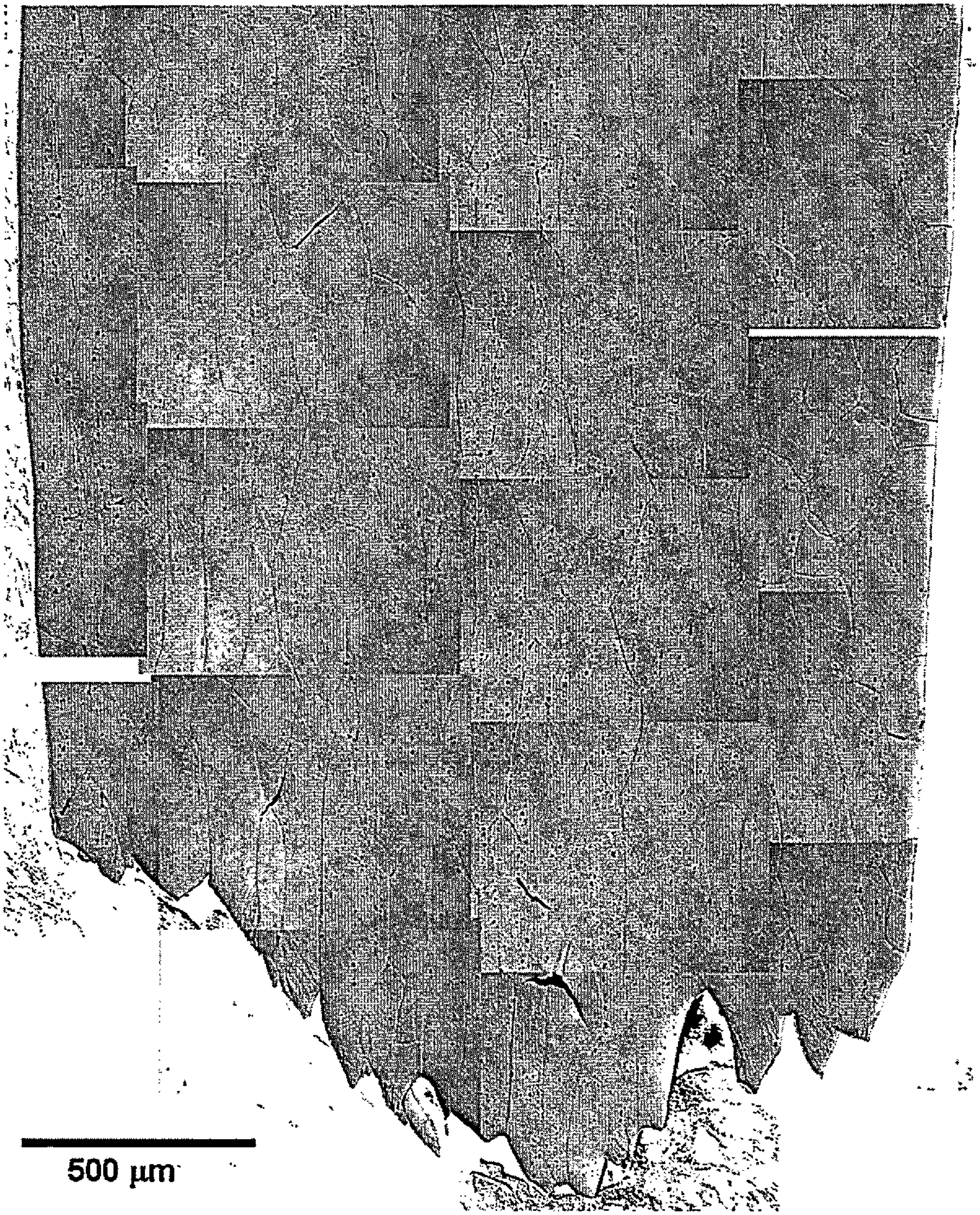

Figure 3.9: Composite image of a 6111 alloy etched to reveal shear.

4 RESULTS

The following section will present the results collected in this study. It is divided into two subsections, one dealing with the 5754 alloy and the other with the 6111 alloy. When appropriate, the experimental errors will be presented with the results, together with the methodology used to estimate these errors.

4.1 AA 5754

Samples of both low and high-Fe contents oriented parallel to the rolling direction, were tested in uniaxial tension. One set of tests was conducted at ambient temperature and pressure and under various superimposed hydrostatic pressures. In addition some tests were conducted at 77K (liquid nitrogen) and ambient pressure. All tensile data is presented in terms of true stress (MPa)-true strain curves.

4.1.1 Ambient Temperature and Pressure Uniaxial Tensile Tests

Figure 4.1 and Figure 4.2 show the uniaxial true stress-strain curves for the low and high-Fe variants respectively. Tensile data derived from these curves are presented in Table 4.1.

Both alloys exhibited discontinuous yielding and a distinct Lüders strain The strain associated with Lüdering for the high-Fe is approximately twice that for the low-Fe alloy which reflects the influence of the differences in grain size, 48 μm for the low-Fe variant and 24 μm for the high-Fe variant. Also evident with both iron contents are the serrations in the tensile curve associated with the Portevin-Le Chatelier (PLC) effect. The serrations begin immediately upon completion of the Lüders strain, and then continue to grow in amplitude with increasing strain up to a maximum of approximately ± 6 MPa for the high-Fe alloy and ± 4 MPa for the low-Fe variant.

It is apparent, with the exception of slightly greater amplitudes of the serrations in the yield curves that there is little difference between the tensile response of either alloy. While there is a significant grain size difference, 48 μm versus 24 μm, between the low and high-Fe variants respectively, this appeared to have little effect on the post-Lüdering deformation behaviour, indicating a small Hall-Petch effect in these alloys.

Table 4.1: Tensile data for 5754 alloys tested at ambient pressure and temperature, in the rolling direction

Material	Uniform Strain	True 0.2% Offset Yield Strength (MPa)	True Ultimate Tensile Strength (MPa)	Strain Hardening Exponent, n
Low Fe	0.2	117	292	0.3
High Fe	0.19	117	290	0.33

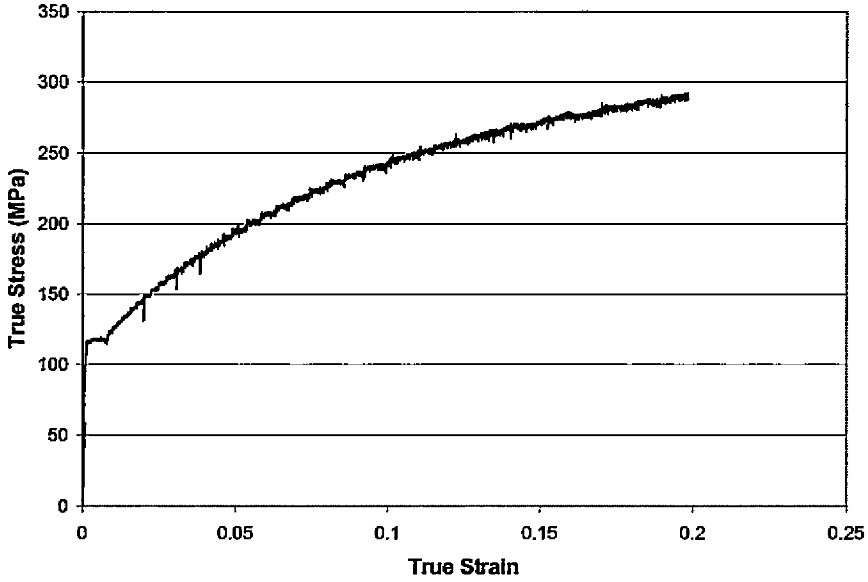

Figure 4.1: True stress-strain curve for low-Fe 5754 alloy tested at ambient pressure and temperature in the rolling direction.

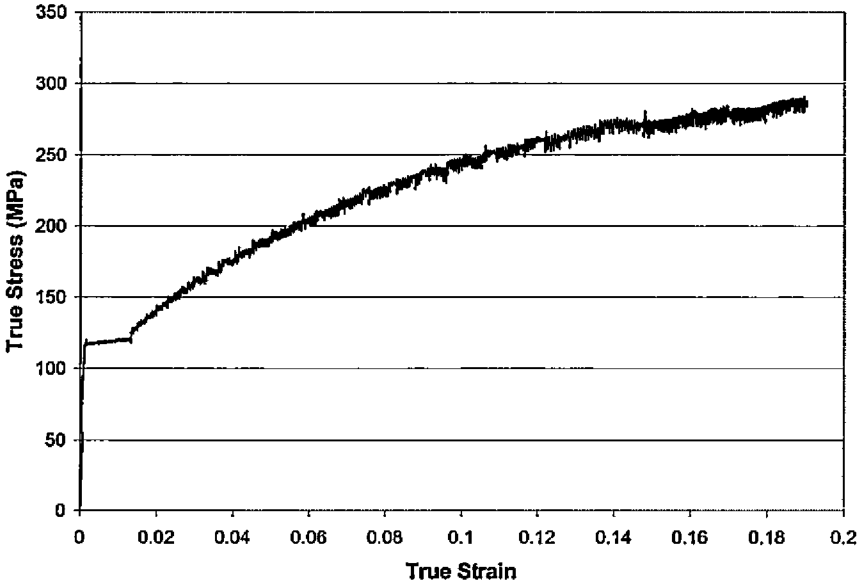

Figure 4.2: True stress-strain curve for high-Fe 5754 alloy tested at ambient pressure and temperature in the rolling direction.

4.1.2 Uniaxial Tensile Tests at 77K and Ambient Pressure

Figure 4.3 and Figure 4.4 show the uniaxial true stress-strain curves for the low and high-Fe variants of the 5754 alloy tested at 77K. Tensile data derived from these curves are presented in Table 4.2.

These samples continued to exhibit Lüdering, with a small increase in the Lüders strains for both the low and high-Fe alloys in comparison with these observed in the ambient temperature tests. Both samples still exhibited serrated yielding, however it was of significantly smaller amplitude initially, and grew at a slower rate. Approaching the fracture condition, there was a large increase in the amplitude of the serrations, up to ± 9 MPa for the high-Fe alloy, exceeding that of the samples tested at ambient temperature. Both alloys exhibited an increase in the strain hardening exponent with decreasing temperature. The related strains to necking increased by approximately a factor of 2 between the samples tested at ambient temperature and those at 77K. There was no marked difference between either sample tested at 77K in terms of n, or necking strain, however the high-Fe variant exhibited a slightly higher true 0.2% offset yield strength, and true ultimate tensile strength.

Table 4.2: Tensile data for 5754 alloys tested at 77k and ambient pressure, in the rolling direction.

Material	Uniform Strain	True 0.2% Offset Yield Strength (MPa)	True Ultimate Tensile Strength (MPa)	Strain Hardening Exponent, n
Low Fe	0.40	116	489	0.43
High Fe	0.44	125	527	0.44

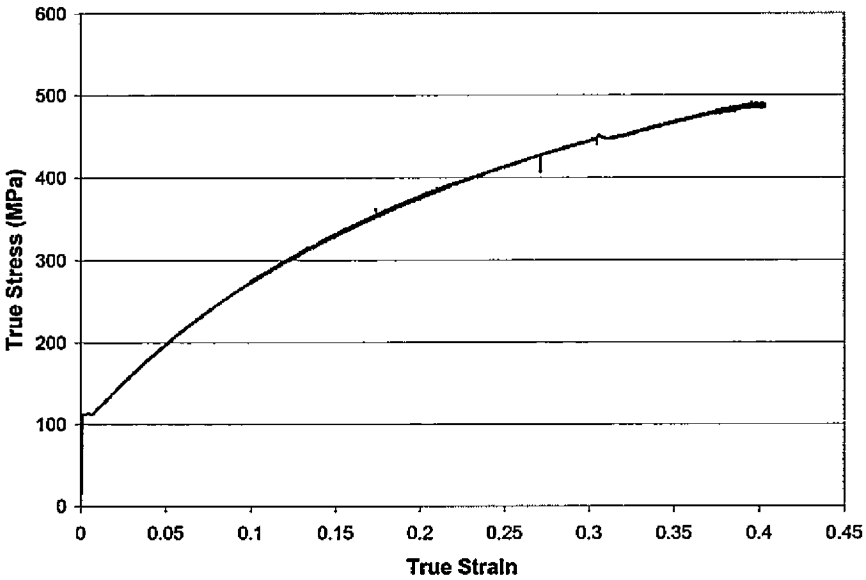

Figure 4.3: True stress-strain curve for low-Fe 5754 alloy tested at 77K and ambient pressure.

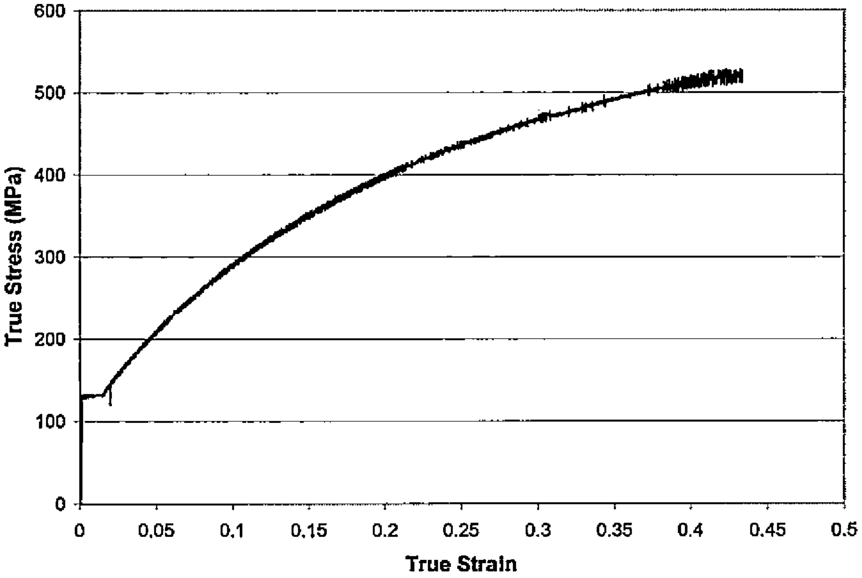

Figure 4.4: True stress-strain curve for high-Fe 5754 alloy tested at 77K and ambient pressure.

4.1.3 Uniaxial Tensile Tests Under Superimposed Pressure

Tests were conducted on the 5754 alloy under various superimposed pressures ranging from atmospheric (0.1 MPa) to 500 MPa. Unfortunately, the tensile strain data collected for these samples was inconsistent, mainly due to persistent slippage of the samples (a result of gripping difficulties) and will not be presented here. Ductility data will be presented based on reduction in area measurements. However, load data was able to be obtained from the tests, and this was used to generate stress values for the fracture maps.

4.1.4 Fracture Behaviour of Uniaxial Tensile Specimens

Depending upon the testing conditions applied to the samples, the main variable being temperature and pressure, various changes in fracture modes occurred for these alloys. Under testing at ambient pressure, the two iron contents exhibited different fracture modes. The low-Fe alloy, consistently fails by a cup and cone mode, Figure 4.5. In contrast, the high-Fe variant fails in a void sheeting mode (microvoid coalescence, shear MVC) when tested at ambient pressure, as shown in Figure 4.6. The failure of the low-Fe alloy is characterized by growth of voids at the centre of the specimen followed by the formation of shear lips, which are relatively featureless, Figure 4.7. The high-Fe alloy showed a much higher concentration of coalesced voids, corresponding to the higher intermetallic content, Figure 4.8.

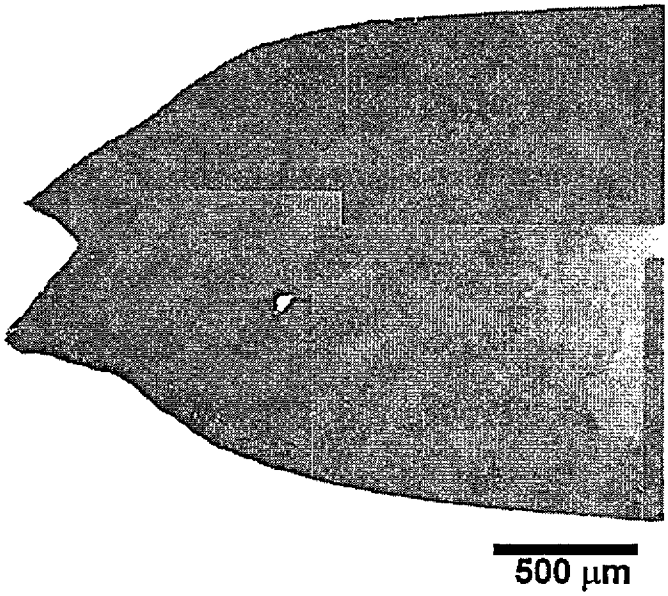

Figure 4.5: SEM Composite image of the necked region of the low-Fe 5754 alloy showing cup and cone failure.

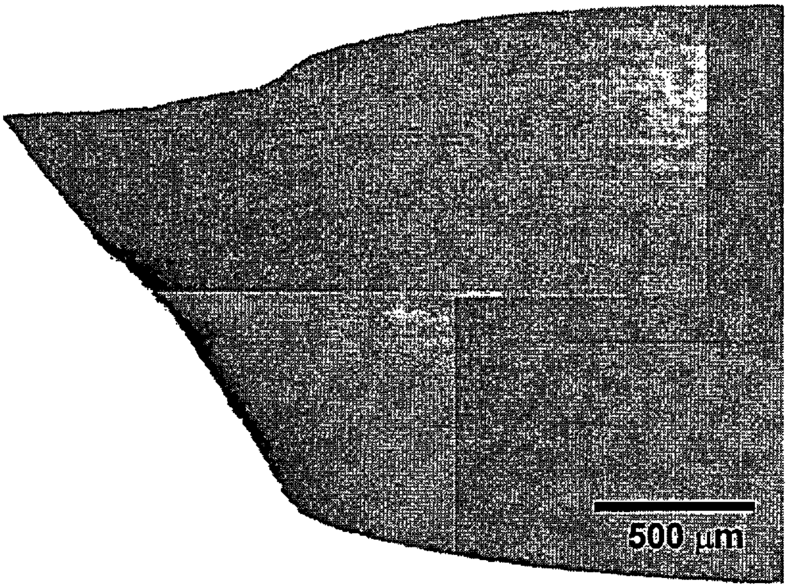

Figure 4.6: **SEM Composite image of the necked region of the high-Fe 5754 alloy showing shear MVC failure.**

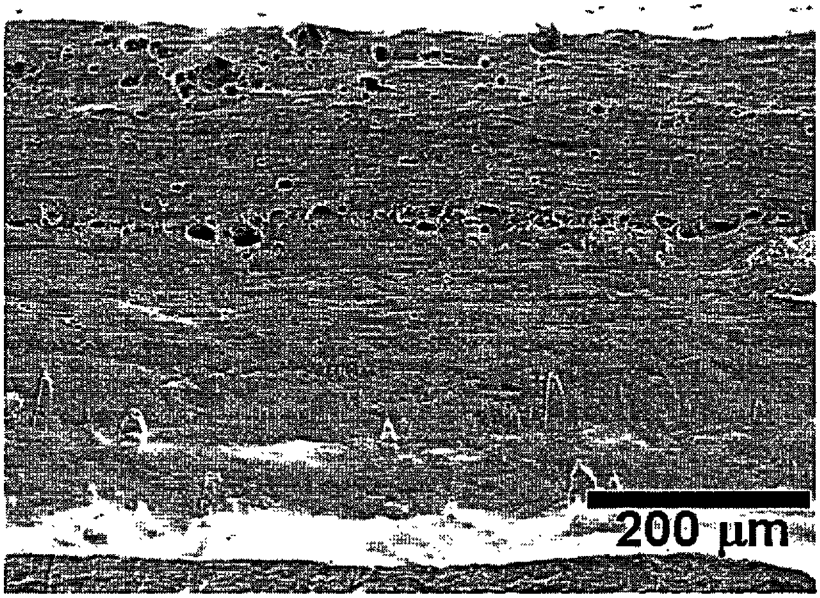

Figure 4.7: **SEM image showing the centre region of the cup on the fracture surface of the low-Fe 5754 alloy. Evident is the voiding present in the central region, while the shear lips contain relatively few voids.**

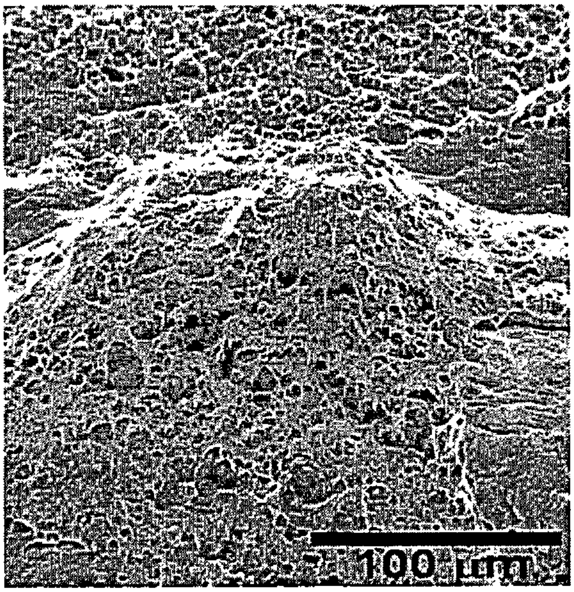

Figure 4.8: SEM image of the high-Fe 5754 alloy showing extensive voiding on the fracture surface.

When tested at 77 K, the low-Fe alloy failed by a combination of cup and cone and shear MVC modes, showing a jagged profile indicative of failure along more that one shear system. The fracture surface exhibited greater damage in the form of a higher void density in comparison to the sample tested at ambient temperature, Figure 4.9. It is also apparent that while the uniform elongation was much higher, the overall ductility of this sample was lower, having undergone significantly less post-necking strain than the sample tested at ambient temperature, Figure 4.10.

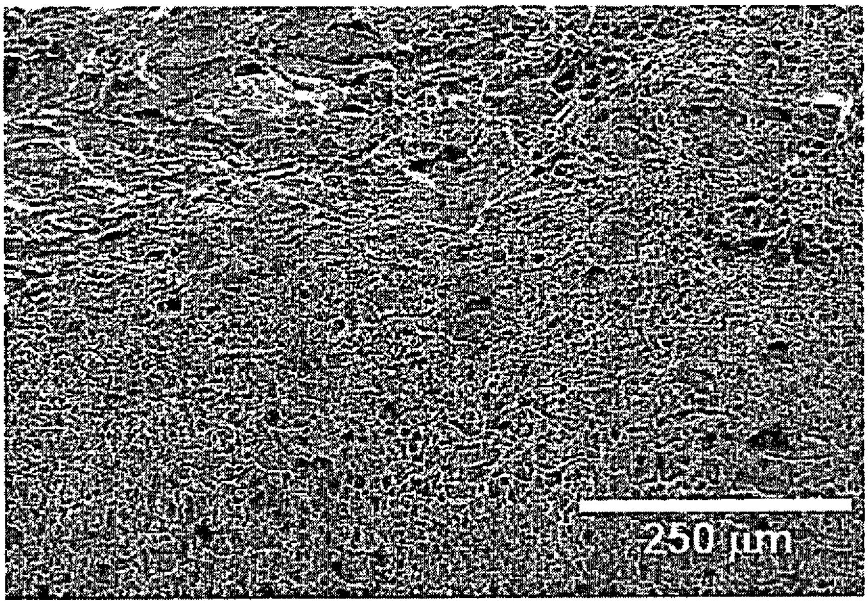

Figure 4.9: SEM image of the low-Fe 5754 alloy tested at 77 K showing extensive voiding of the fracture surface.

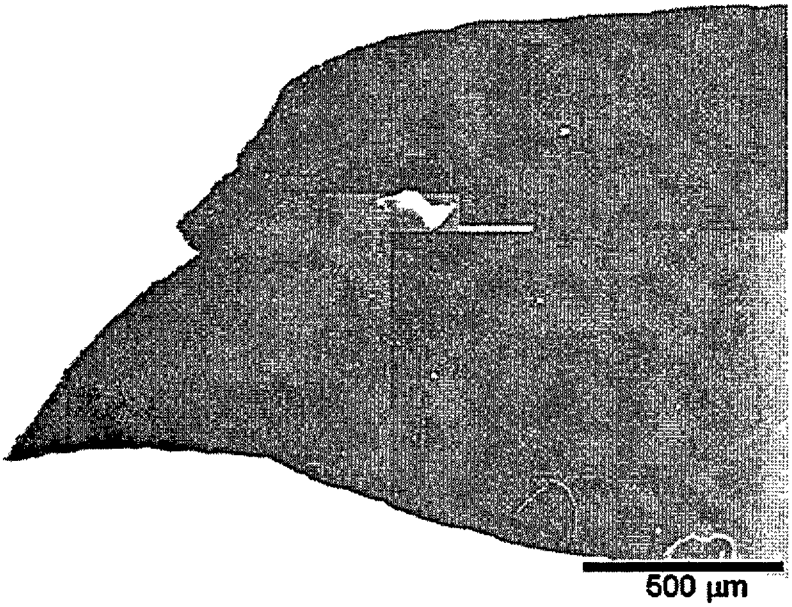

Figure 4.10: SEM Composite image of the necked region of the low-Fe 5754 alloy tested at 77 K, showing shear MCV and cup and cone failure.

The high-Fe alloy also showed changes in fracture mode when tested at 77 K. It exhibited a jagged profile similar to the low-Fe samples, Figure 4.11. This is in contrast to the relatively smooth profile of the high-Fe sample tested at ambient temperature. There was however, little apparent difference in either the overall amount of the reduction in area of the sample or the density of voids when compared to the sample tested at ambient temperature, though uniform elongation was significantly higher.

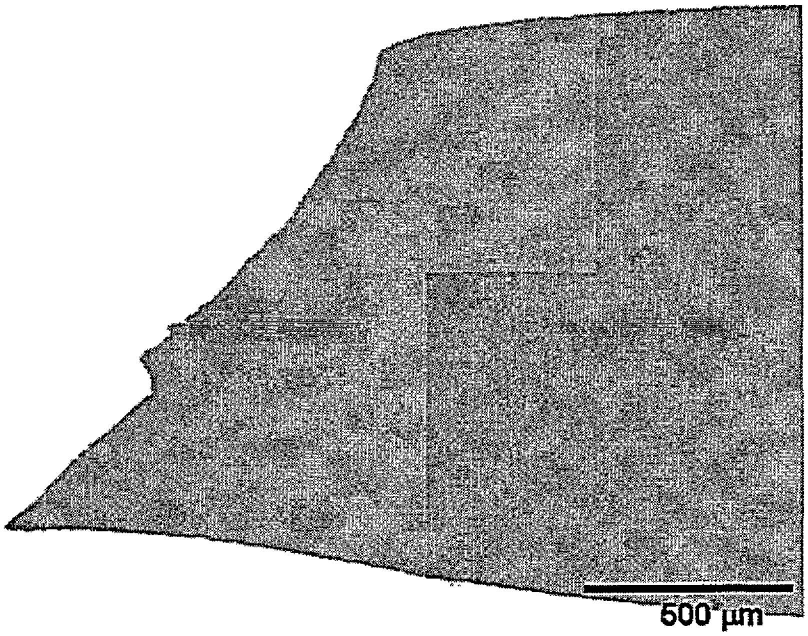

Figure 4.11: Composite image of the necked region of the high-Fe 5754 alloy tested at 77 K, showing shear MCV failure.

The low-Fe alloy showed no drastic changes in fracture mode when tested under 125 MPa of superimposed pressure, simply necking down to a larger degree, Figure 4.12. The high-Fe 5754 alloy showed no significant change in fracture mode when tested under pressure, with the exception of a transition to ductile rupture at 250 MPa, Figure 4.13.

The sample tested at a superimposed pressure of 125 MPa failed by shear MVC, albeit with more extensive post-necking strain than the sample tested at 0.1 MPa, Figure 4.14.

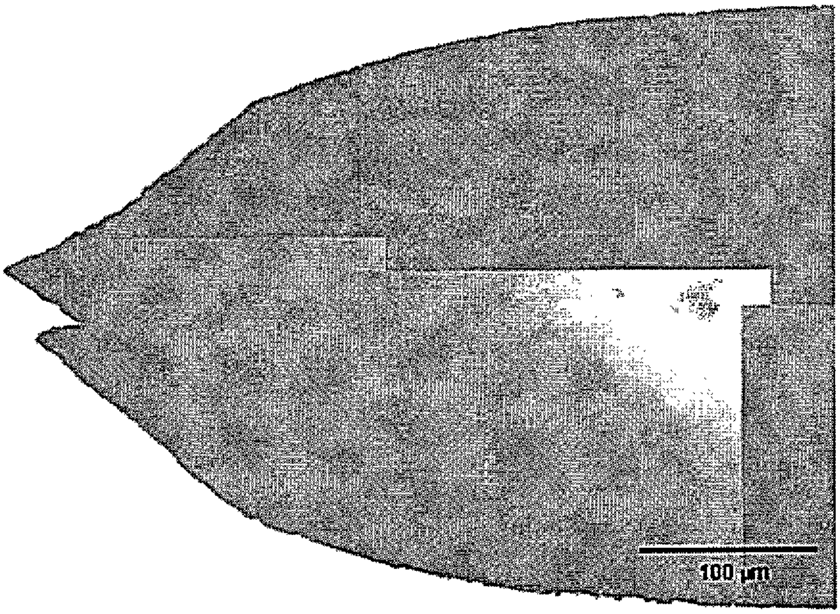

Figure 4.12: Composite image of the necked region of the low-Fe 5754 alloy tested at 125 MPa showing cup and cone failure and severe necking.

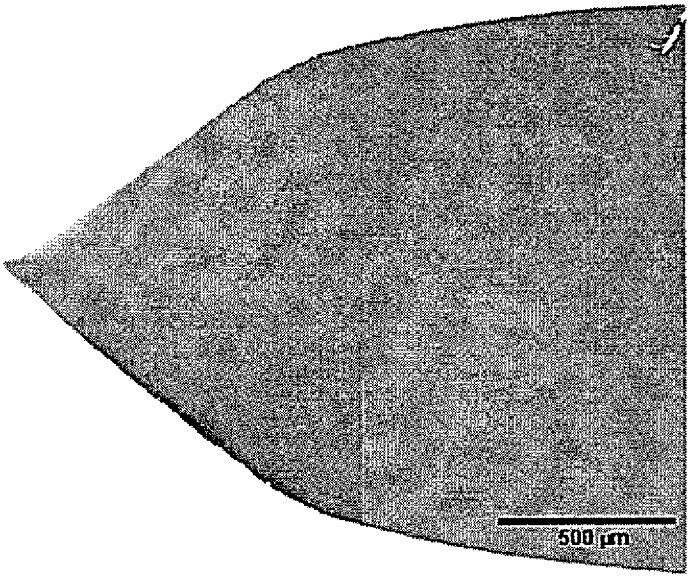

Figure 4.13: Composite image of the necked region of the high-Fe 5754 alloy tested at 250 MPa showing ductile rupture.

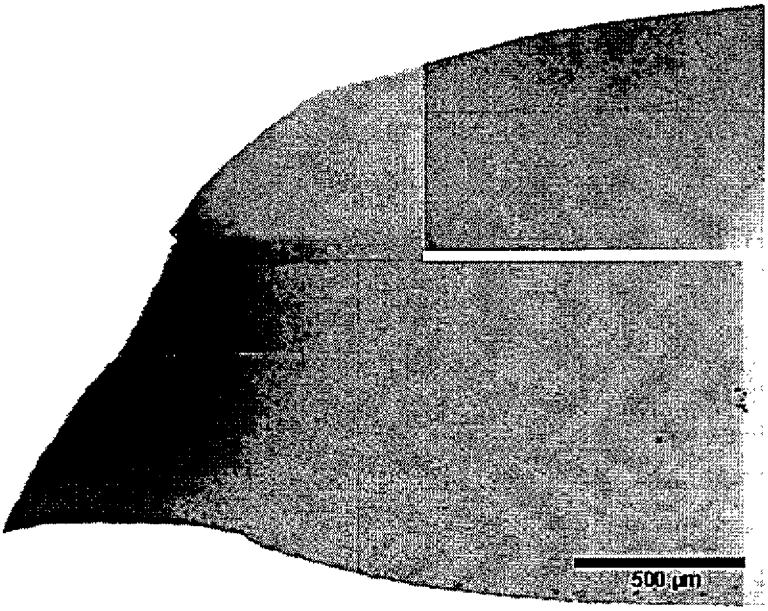

Figure 4.14: Composite image of the necked region of the high-Fe 5754 alloy tested at 125 MPa showing shear MCV failure.

A summary of the fracture modes observed and the associated test conditions for all the 5754 samples tested is shown in Table 4.3.

Table 4.3: Summary of the tests performed on the 5754 alloy and the associated fracture modes

Material	Pressure (MPa)	Temp (K)	Failure Mode
Low Fe	0.1	298	Cup and Cone
Low Fe	0.1	77	Mixed (Cup and Cone/Shear MVC)
Low Fe	125	298	Cup and Cone
High Fe	0.1	298	Shear MVC
High Fe	0.1	77	Shear MVC
High Fe	125	298	Shear MVC
High Fe	250	298	Ductile Rupture
High Fe	500	298	Ductile Rupture

4.1.5 Reduction in Area (RA) Measurements

As consistent elongation data for the tests conducted under superimposed pressure was unavailable, the reduction in area of a samples fracture surface was taken as the measure of ductility. These measurements are summarized in Table 4.4. Error values were calculated by estimating the accuracy to which the image analysis could be done in terms of the correct selection of the fracture surface edge, which was typically about 3X3 pixels for an image of resolution 1024X861. This translates into an error of 6 μm in any measurement. The overall area was then simplified by assuming there was no strain in the width of the tensile sample. Therefore the area can be considered to be equivalent to a rectangle of dimensions x = 6.8 mm (original sample width) by some value y, which is calculated from the actual measured area. The error of 6 μm is then applied to these dimensions, and the experimental error is calculated.

Table 4.4: Reduction in area measurements for 5754 alloys

Material	Pressure (MPa)	Reduction in Area (%)
Low-Fe	0.1	76 ± 0.31
Low-Fe	0.1 @ 77 K	65 ± 0.33
Low-Fe	125	91 ± 0.31
High-Fe	0.1	54 ± 0.34
High-Fe	0.1 @77 K	56 ± 0.34
High-Fe	125	63 ± 0.33
High-Fe	250	100 ± 0
High-Fe	500	100 ± 0

These results show a trend of an increase in the reduction in area, i.e. greater ductility with increasing applied hydrostatic for all iron levels. Of note is the decrease in RA when the low-Fe alloy is tested at 77 K, even though from examination of the stress strain data this is occurring at a much higher stress. This is likely due to the transition to the shear MVC mode of failure. The reduction in area of the high-Fe alloy appears to be relatively insensitive to testing temperature.

4.1.6 Damage Analysis

Polished sections of the samples, as described in the methods sections, were examined under the SEM in order to determine the amount of damage present. In this study, damage was defined specifically as open voids associated with intermetallic particles, and not the number of cracked particles. The reason for this approach was the difficulty in accurately differentiating between those particles that were cracked during tensile testing and those that cracked during the hot and cold rolling, which occurred during processing of the sheet. Secondly, it is felt that it is the presence of open voids that is more important in terms of generating instabilities in material flow. The errors in these measurements were simply calculated as an RMS error. An arbitrary error of 10% was applied to all measurements taken from the image analysis software, as this was considered to be the limit of the accuracy possible. This gave an estimated error of approximately 10% to values of damage, and 1% for the strain measurements.

The damage (%) measured in terms of percentage of the total surface area is presented in Figure 4.15 and Figure 4.16 as a function of true strain. Where damage (%) and true strain are defined as:

$$Damage(\%) = \frac{Area\ of\ Voids}{Total\ Area\ Measured} \times 100$$

$$True\ Strain = \ln\left(1 + \left(\frac{Initial\ Thickness - Measured\ Thickness}{Initial\ Thickness}\right)\right)$$

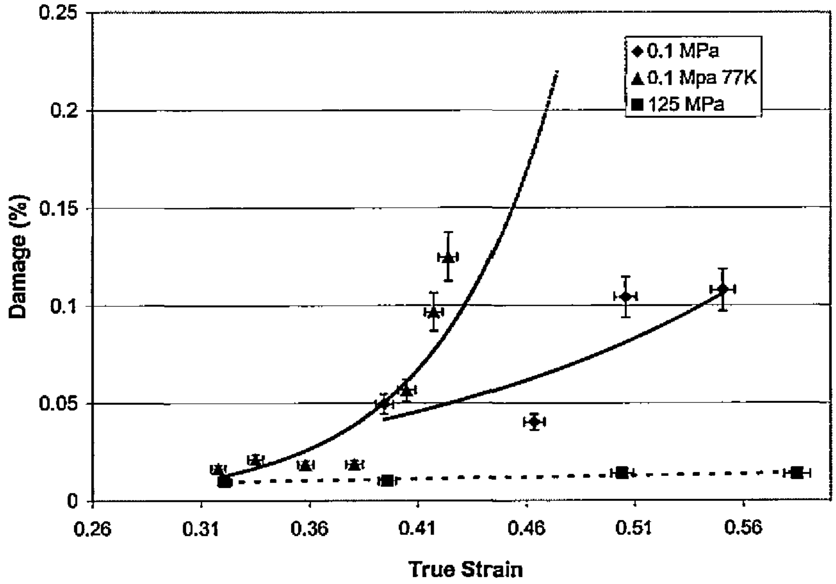

Figure 4.15: Damage (%) as a function of strain in the low-Fe 5754 alloy.

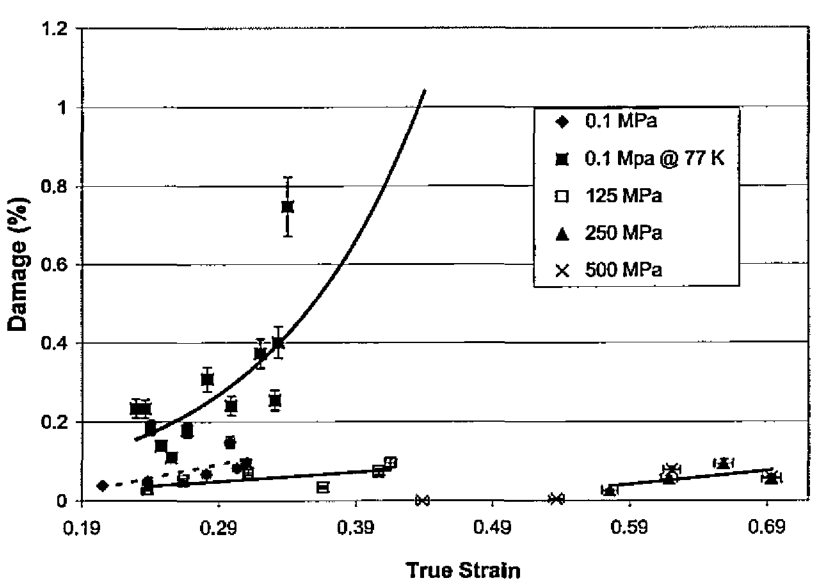

Figure 4.16: Damage (%) as a function of strain in the high-Fe 5754 alloys.

It is apparent from Figure 4.15 that very little damage accumulates in the low-Fe 5754 alloy under any test condition, and is typically less than 0.1 % (close to the limit of what can be realistically analyzed using the methods employed). This may reflect the very low iron content present in the alloy, and thus a low-Fe-aluminum intermetallic content.

Figure 4.17 to Figure 4.22 show SEM images of damage for the low and high-Fe alloys. The overall lack of damage present in these samples is apparent. The damage levels observed for the high-Fe variant are higher than those observed for the low-Fe, reaching a maximum of 0.75% for the sample tested at 77K, concurrent with a much higher intermetallic content. The sample tested at 0.1 MPa showed only slightly more damage present that those tested under pressure, typically less that 0.1 % for any pressure. Significant increases in true necking strain were seen with increasing pressure as expected, up to a maximum of 0.693 (ln2), corresponding to the sample necking to a knife edge. Alignment of particle stringers, corresponding to conjugate shear processes can be seen in the high-Fe samples tested at 250 and 500 MPa.

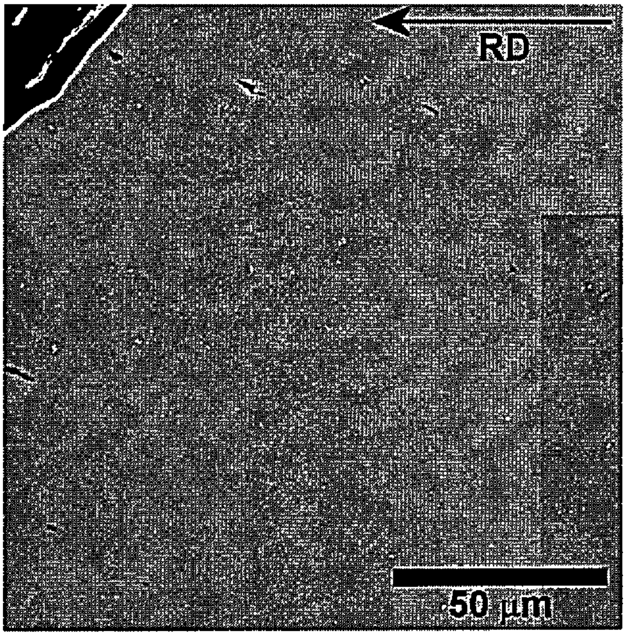

Figure 4.17: SEM image of damage near the fracture surface of the low-Fe 5754 alloy tested at ambient temperature and pressure.

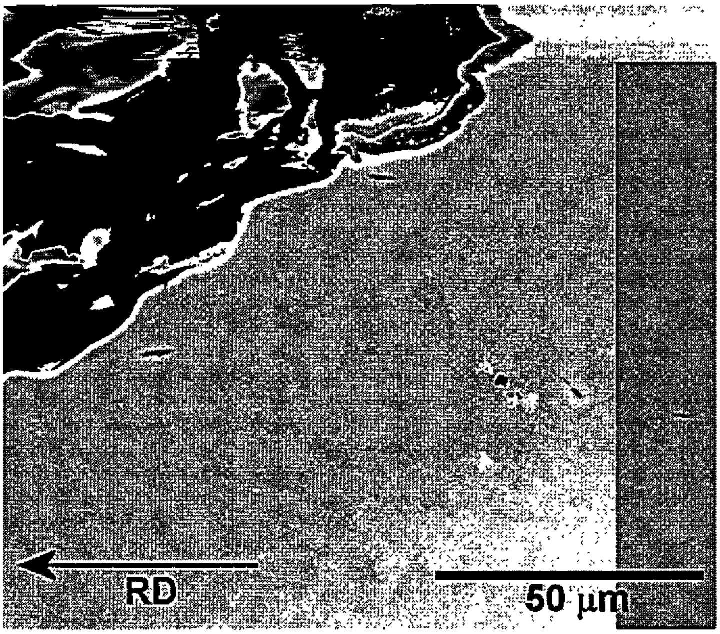

Figure 4.18: SEM image of damage near the fracture surface of the low-Fe 5754 alloy tested at 77 K and ambient pressure.

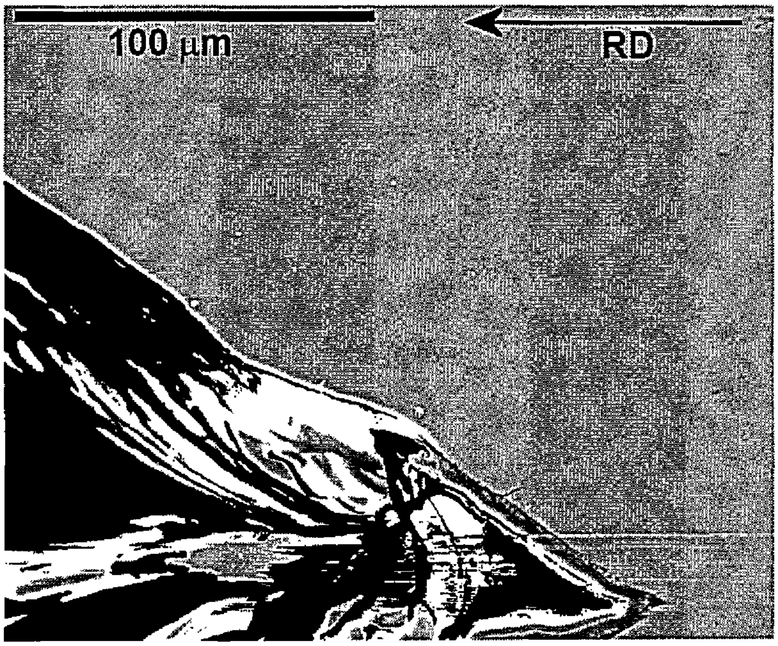

Figure 4.19: SEM image of damage near the fracture surface of the low-Fe 5754 alloy tested at 125 MPa.

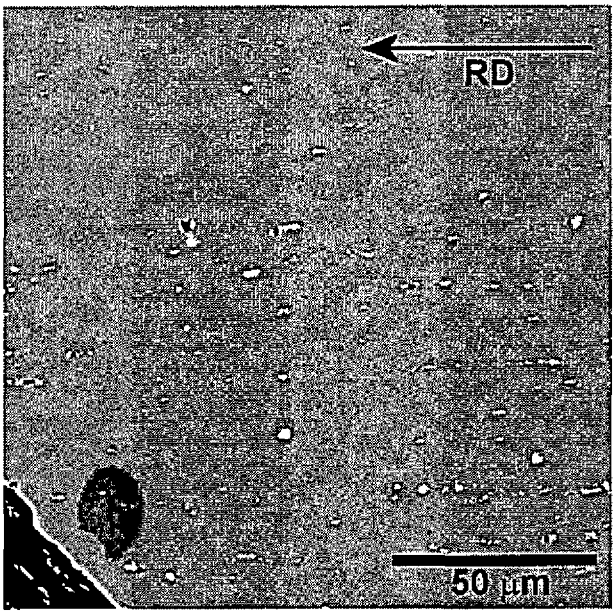

Figure 4.20: SEM image of damage near the fracture surface of the high-Fe 5754 alloy tested at ambient temperature and pressure.

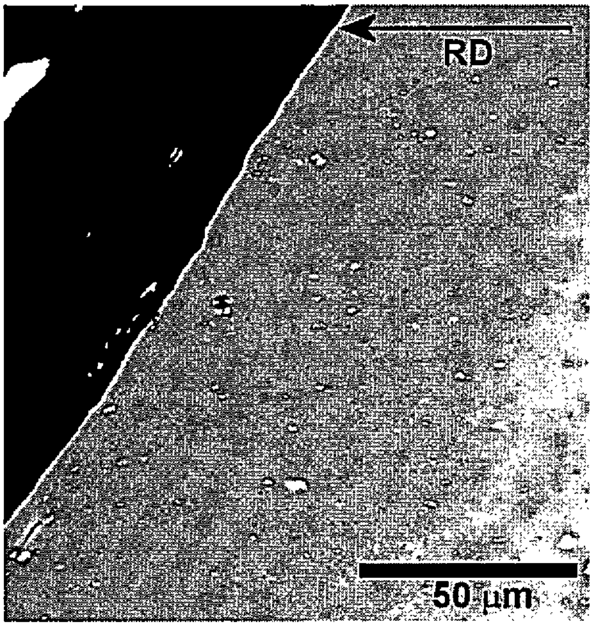

Figure 4.21: SEM image of damage near the fracture surface of the high-Fe 5754 alloy tested at 125 MPa.

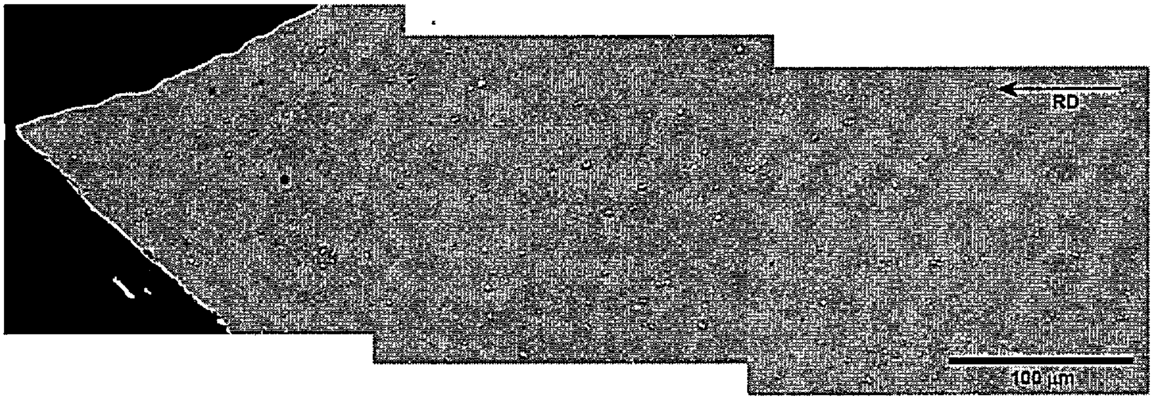

Figure 4.22: SEM image of damage of the high-Fe 5754 alloy tested at 500 MPa.

4.1.7 Shearing Behaviour

An examination of the necked region was made for all the entire 5754 samples, all of which were etched to reveal the presence of slip and shear. Figure 4.23 to Figure 4.29

show full composite micrographs of the necked regions of the low and high-Fe 5754 alloys tested at various temperatures and pressures. At both 0.1 and 125 MPa, the low-Fe variants tested at 298 K show the presence of extensive shear band formation within the necked region across the entire sample. No shearing is visible outside the neck. Within the region where the central void initially forms, the cusp of the cup, the intersection of the conjugate shear bands can be observed, Figure 4.23. Outside this region, the material appears undeformed, indicating the presence of a shear deformation dead zone.

At 77K the low-Fe sample shows significantly less shearing within the necked region, and the presence of a macroscopic shear banding is difficult to identify, although it appears that there is some coordination of slip, Figure 4.24. In comparison to the sample tested at 298 K, it has necked significantly less however, grain scale shearing outside the neck is more apparent.

Large scale shear banding was evident in the high-Fe samples at all pressures tested, Figure 4.25 to Figure 4.29. The major difference between these and the low-Fe samples was the lack of the central void. While conjugate shearing was present similar to that observed in the low-Fe samples, at the intersection of the shear bands no central void is formed. Rather, failure appears to have occurred preferentially along one band. At higher pressures, the high-Fe samples failed by ductile rupture (i.e. with 100% reduction in area). Significant shearing is evident on either side of the knife-edge fracture surface, with a clear intersection of shear bands formed symmetrically at the centreline of the sample. Shearing appears to have been severely retarded when the sample was tested at

77 K. No large changes in fracture mode were apparent and no identifiable grain or large sample scale shearing was evident.

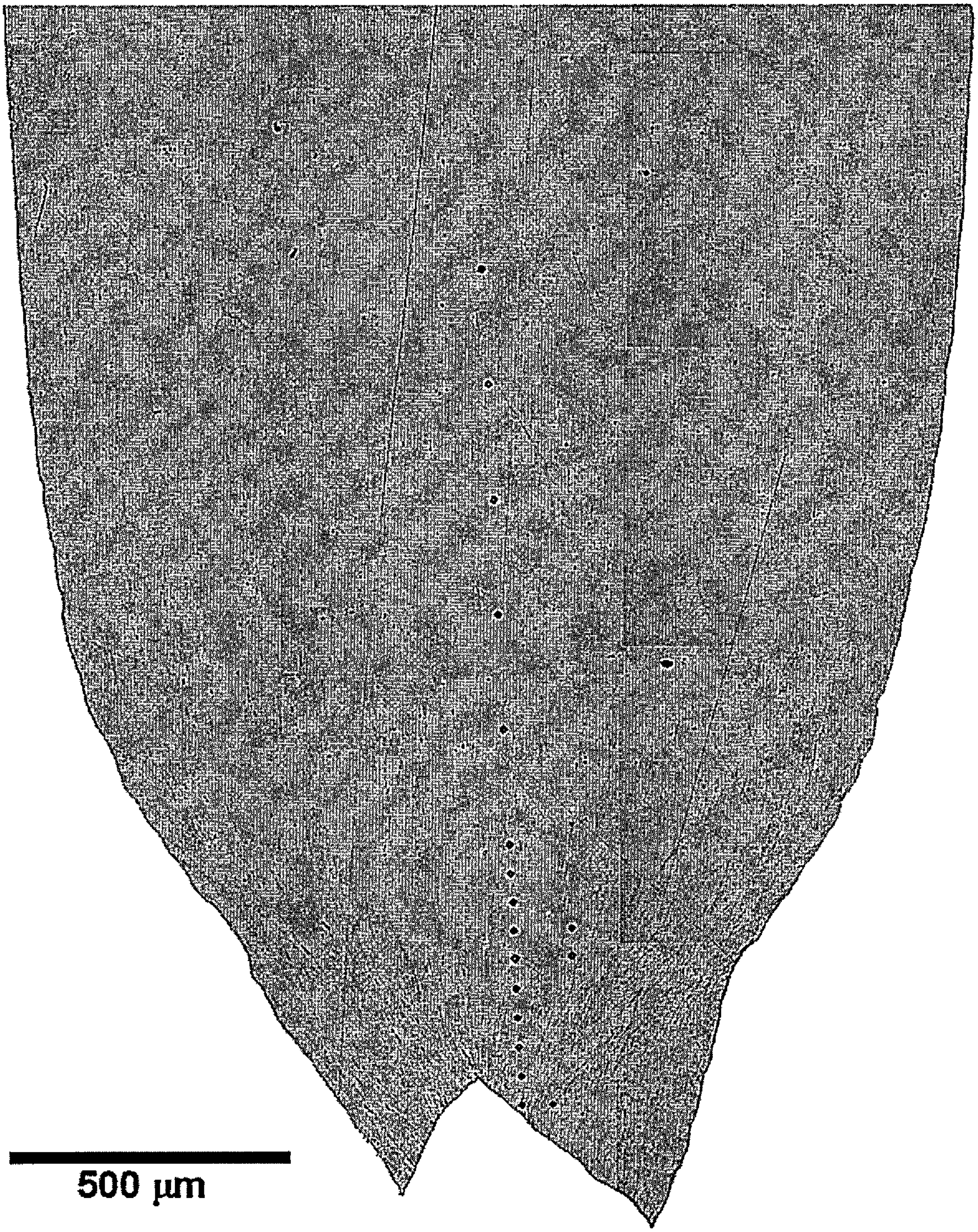

Figure 4.23: Low-Fe 5754 sample tested at 0.1 MPa, etched to reveal shearing and slip.

Figure 4.24: Low-Fe 5754 sample tested at 0.1 MPa and 77 K, etched to reveal shearing and slip.

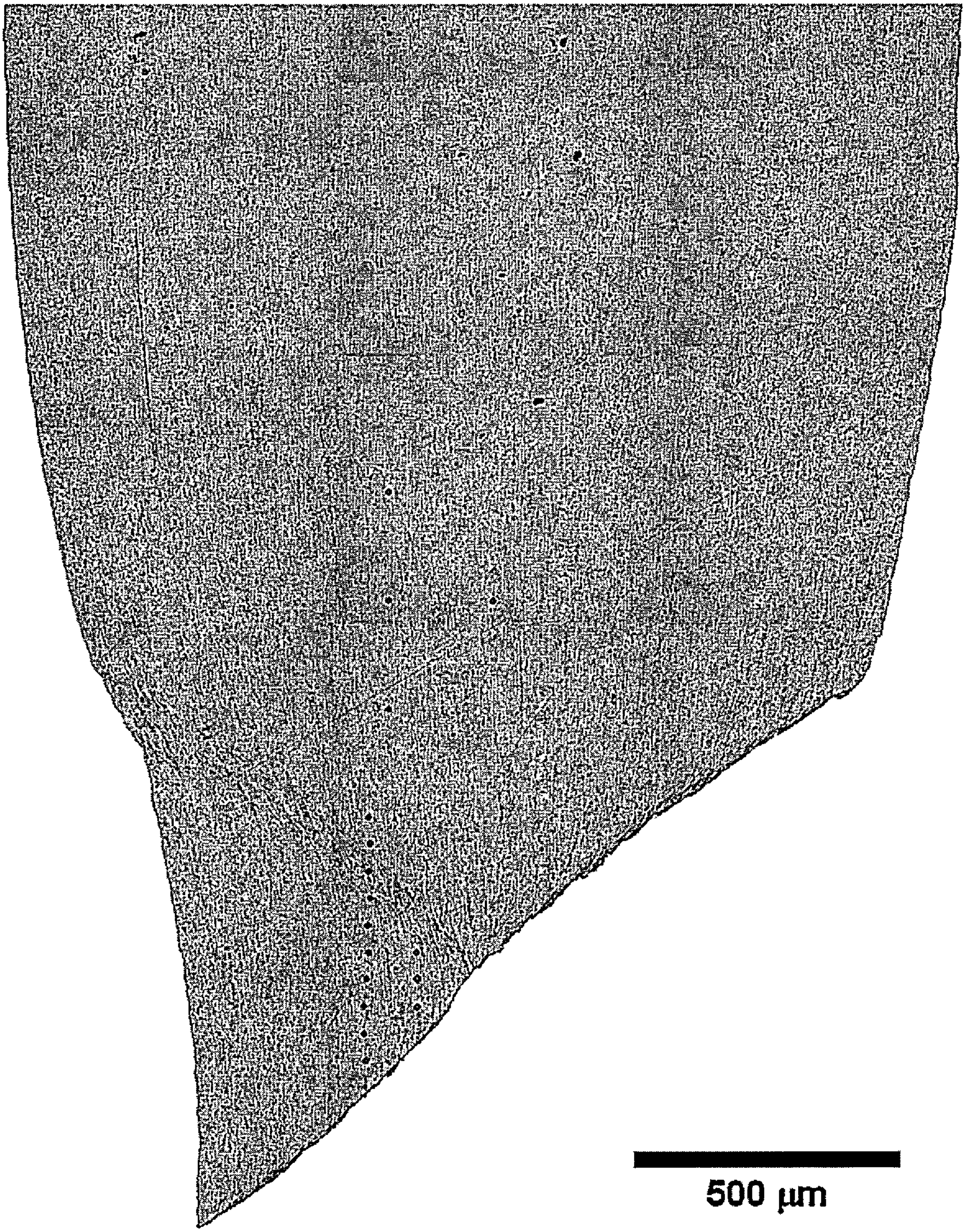

Figure 4.25: High-Fe 5754 sample tested at 0.1 MPa, etched to reveal shearing and slip.

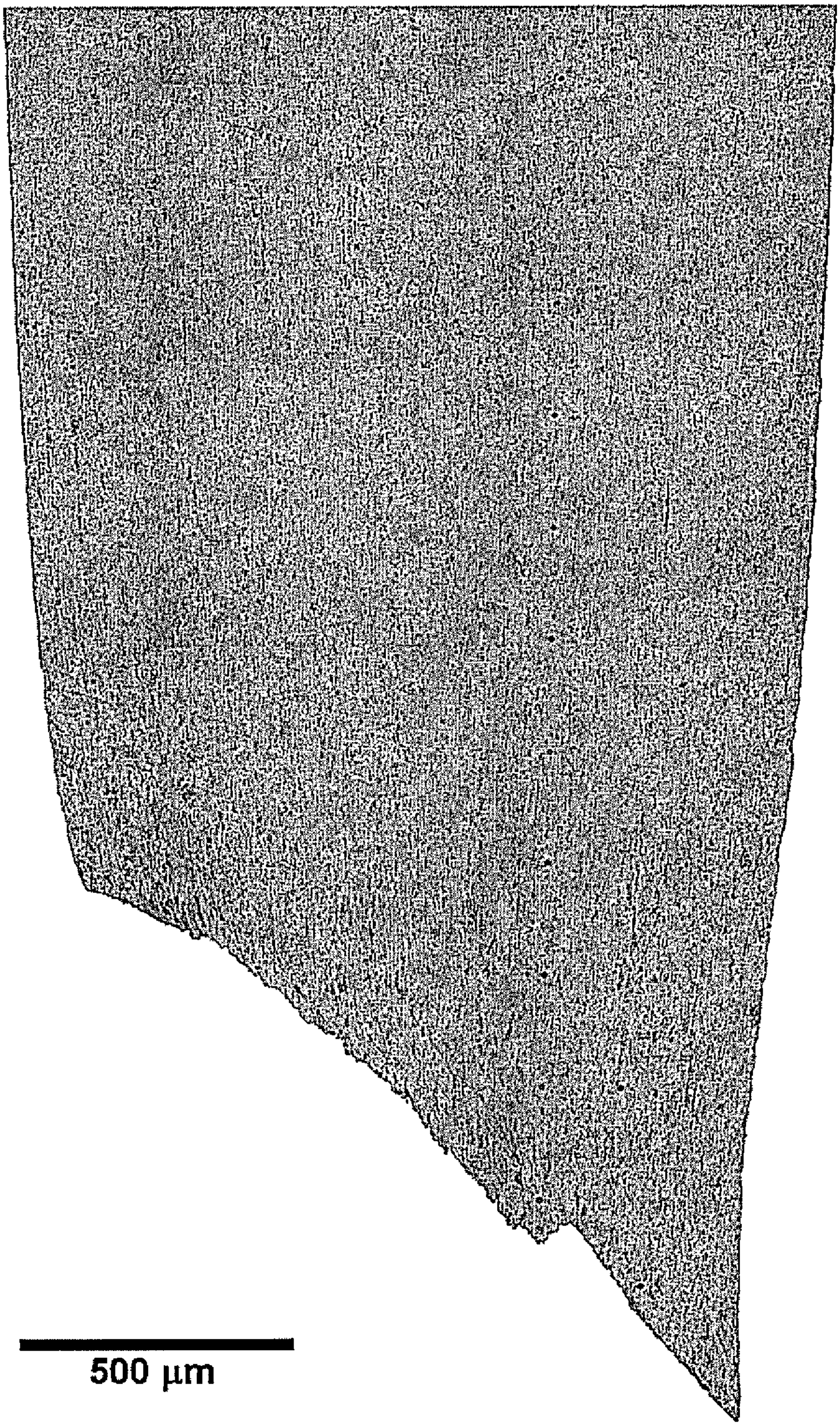

Figure 4.26: High-Fe 5754 sample tested at 0.1 MPa and 77 K, etched to reveal shearing and slip.

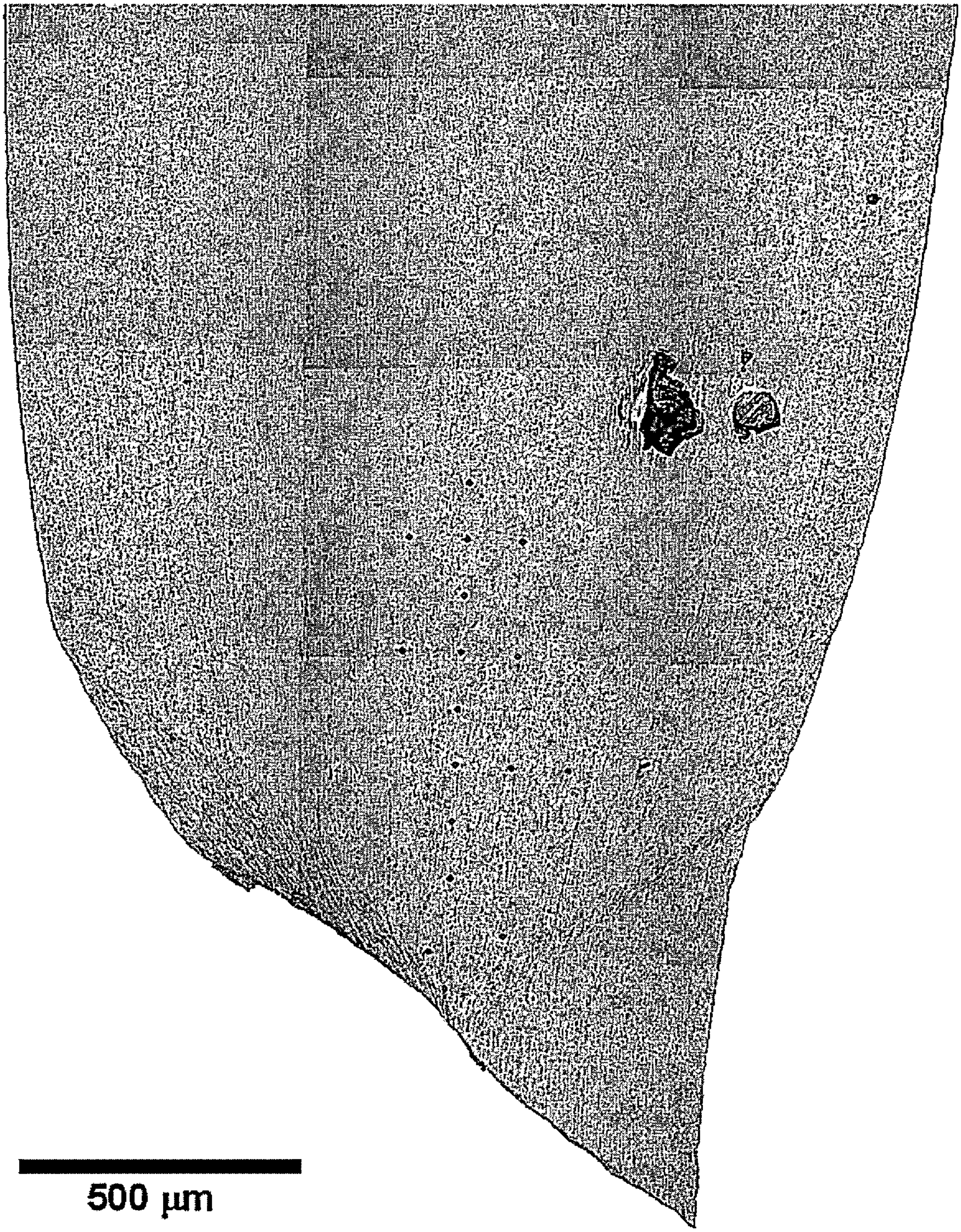

Figure 4.27: High-Fe 5754 sample tested at 125 MPa, etched to reveal shearing and slip.

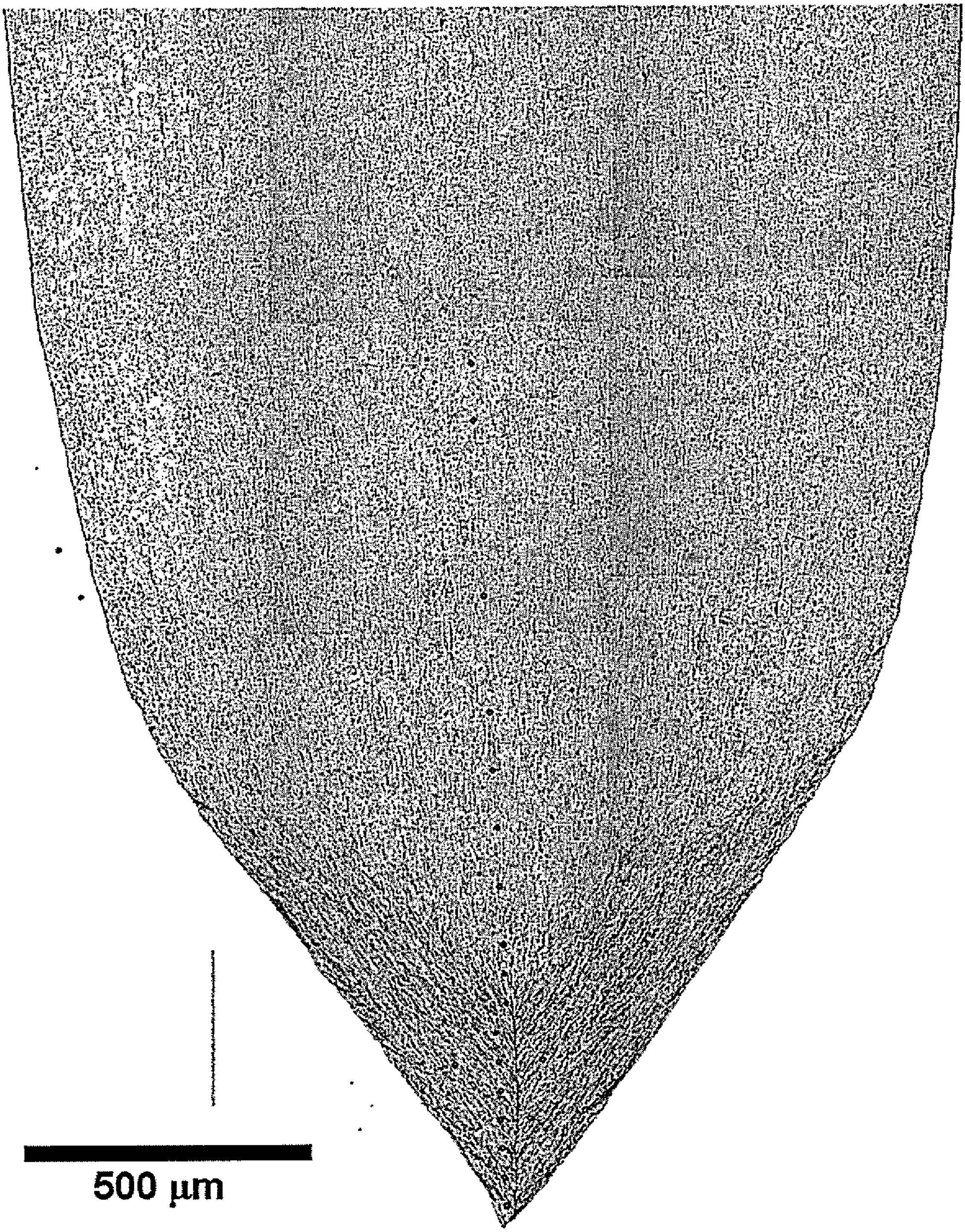

Figure 4.28: High-Fe 5754 sample tested at 250 MPa, etched to reveal shearing and slip.

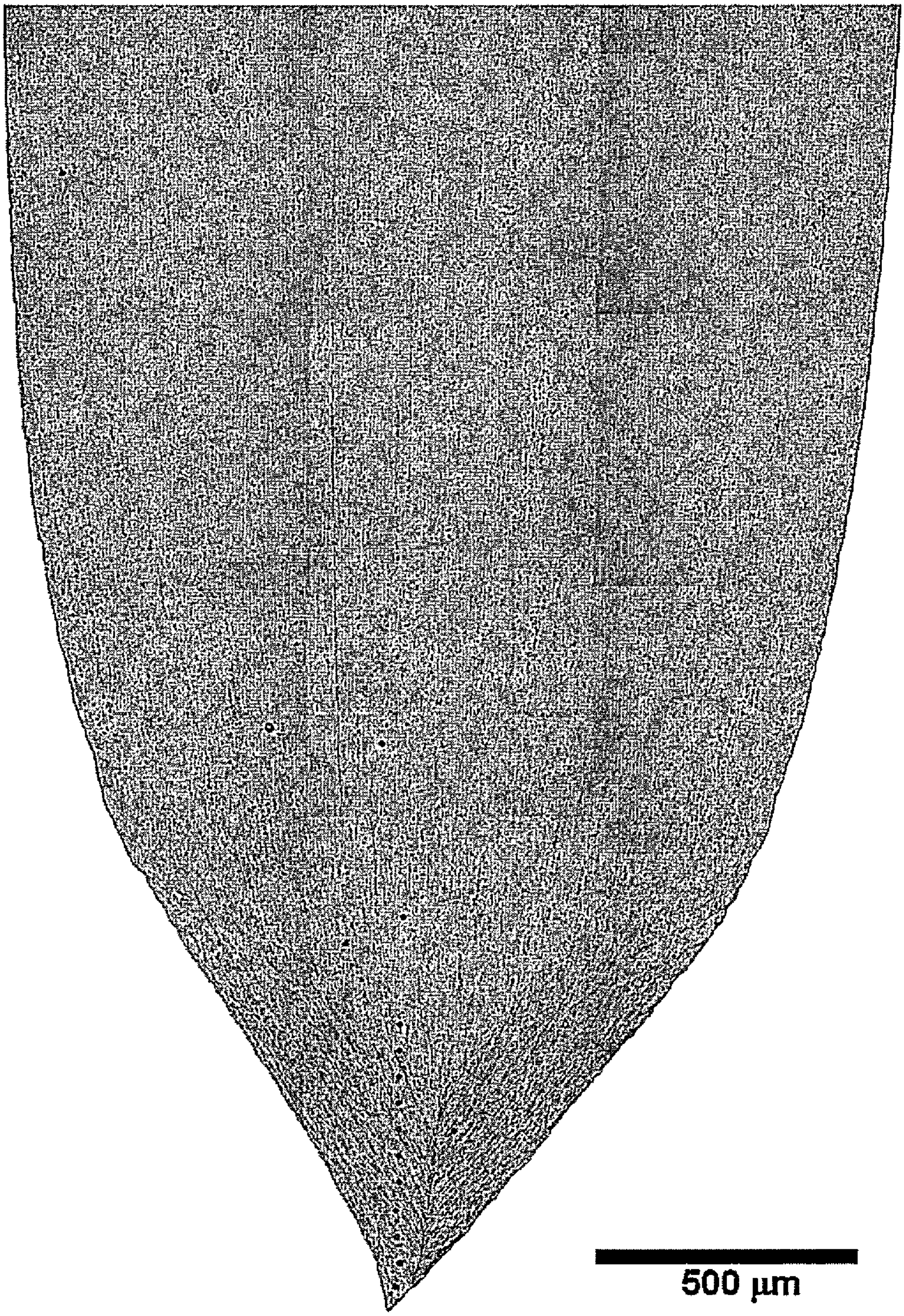

Figure 4.29: High-Fe 5754 sample tested at 500 MPa, etched to reveal shearing and slip.

4.2 AA 6111

Samples of the both low and high-Fe 6111 alloys in the T4 and T6 temper were tested in uniaxial tension in the rolling direction. Tests were conducted at ambient pressure and under various superimposed hydrostatic pressures. No low temperature tests were conducted, as the 6111 alloys do not show the PLC effect. All tensile data is presented in terms of true stress (MPa) and true strain.

4.2.1 Ambient Pressure Uniaxial Tensile Tests

Figure 4.30 and Figure 4.31 show the uniaxial true stress-strain curves for the low and high-Fe T4 alloy and the low and high-Fe T6 alloy respectively. Tensile data derived from these curves is shown in Table 4.5.

The low-Fe T4 alloy shows a larger uniform elongation than the high-Fe variant. Both materials show little apparent difference in their yield strength or ultimate tensile strength however the work hardening rate of the low-Fe alloy was slightly higher.

The T6 materials show significantly higher yield and ultimate tensile strengths due to their peak-aged conditions. The high-Fe variant shows a slightly lower yield strength than the low-Fe T6 alloys, however it had a higher ultimate tensile, this related to its higher work hardening rate. Unexpectedly, the low-Fe variant consistently showed a lower elongation than the high-Fe variant. This was found to be the result of the low-Fe T6 materials failing intergranularly, while the high-Fe T6 material failed exclusively by shear MVC.

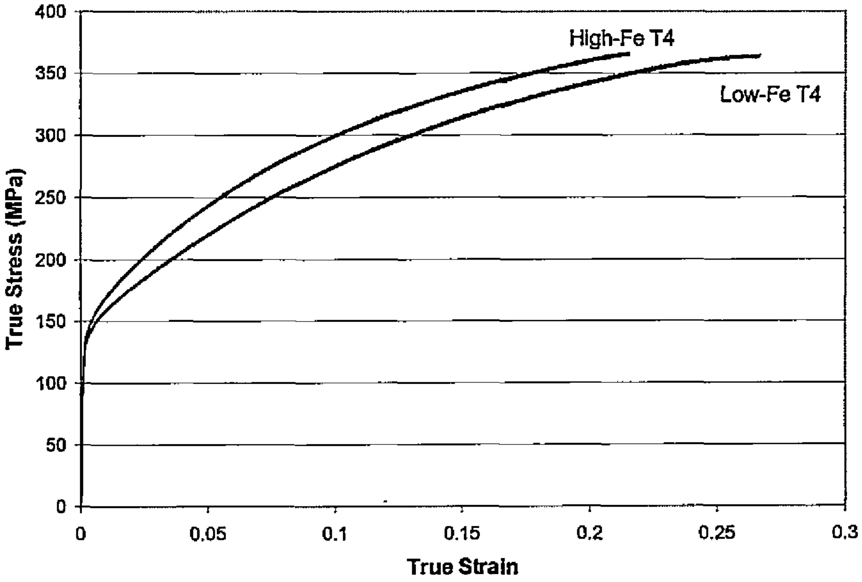

Figure 4.30: True stress-strain curves for the low and high-Fe 6111 alloys in the T4 temper. Tested at ambient pressure and temperature.

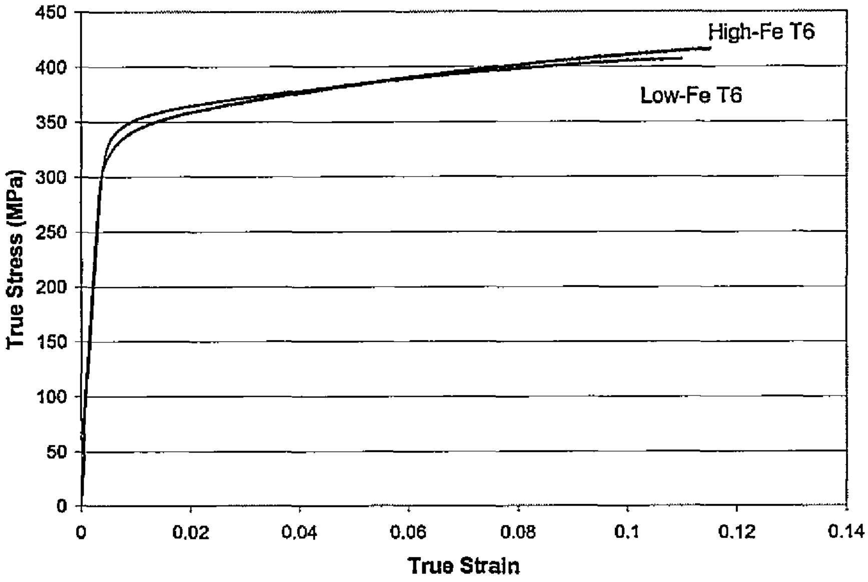

Figure 4.31: True stress-strain curves for the low and high-Fe 6111 alloys in the T6 temper. Tested at ambient pressure and temperature.

Table 4.5: Tensile data for 6111 alloys in both T4 and T6 tempers, tested at ambient pressure and temperature

Material	Uniform Strain	True 0.2% Offset Yield Strength (MPa)	True Ultimate Tensile Strength (MPa)	Strain Hardening Exponent, n
Low-Fe T4	0.27	156	365	0.31
High-Fe T4	0.22	156	367	0.28
Low-Fe T6	0.11	348	407	0.068
High-Fe T6	0.13	337	419	0.088

4.2.2 Uniaxial Tensile Tests Under Superimposed Pressure

Tests under various superimposed pressures ranging from atmospheric (0.1 MPa) to 500 MPa where conducted on the 6111 alloys. As was noted for the 5754 samples, no valid elongation data could be obtained.

4.2.3 Fracture Behaviour of Uniaxial Tensile Specimens

The fracture behaviour of the 6111 alloys was examined through SEM fractography for both the T4 and T6 tempers at a variety of applied superimposed hydrostatic pressures.

Figure 4.32 to Figure 4.35 show the fracture response of the low-Fe T4 alloy when tested at various pressures. This material consistently failed by shear MVC for all pressures tested until 500 MPa, where it failed by ductile rupture. It is apparent that the post-necking strain of the samples increased consistently with increasing superimposed pressure. Similarly, the high-Fe T4 alloy also failed by shear MVC up to 250 MPa, along with a corresponding increase in the post-necking strain, Figure 4.36 to Figure 4.38. No transition to ductile rupture was observed for the high-Fe samples, indicating a sufficient superimposed pressure was not reached.

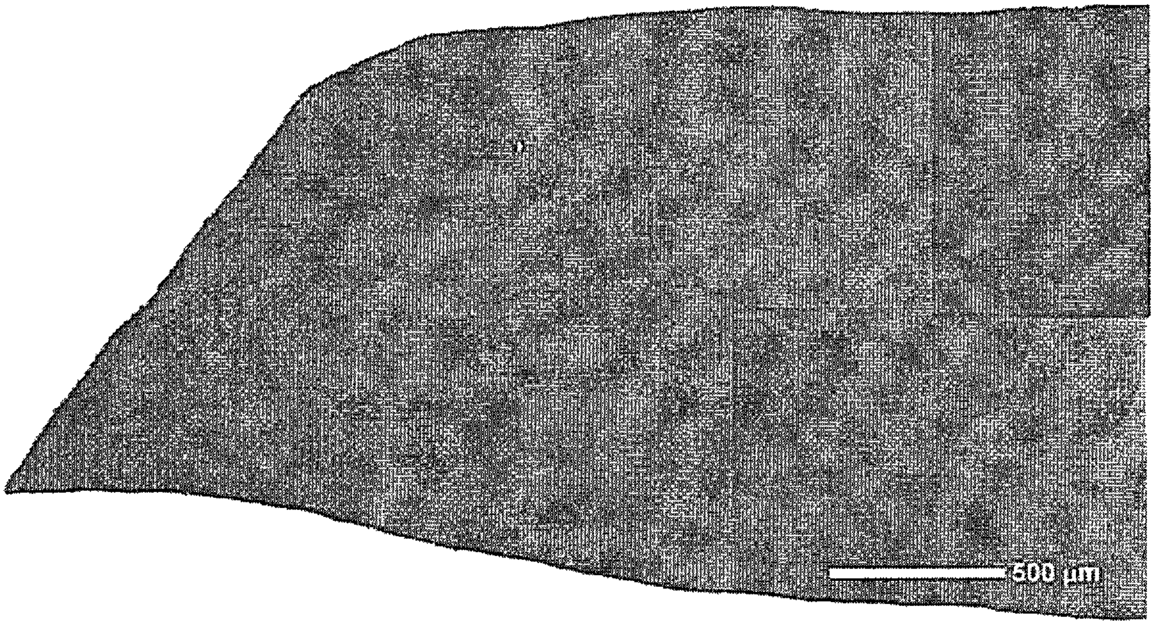

Figure 4.32: Composite image of the necked region of the low-Fe 6111 T4 alloy tested at 0.1 MPa showing shear MVC failure.

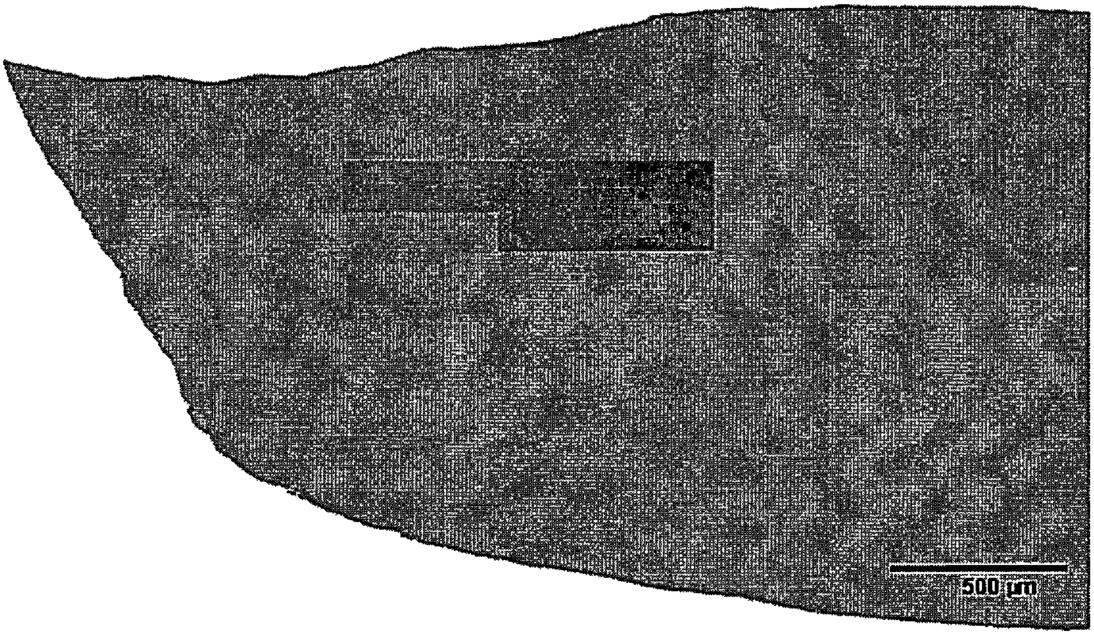

Figure 4.33: Composite image of the necked region of the low-Fe 6111 T4 alloy tested at 125 MPa showing shear MVC failure.

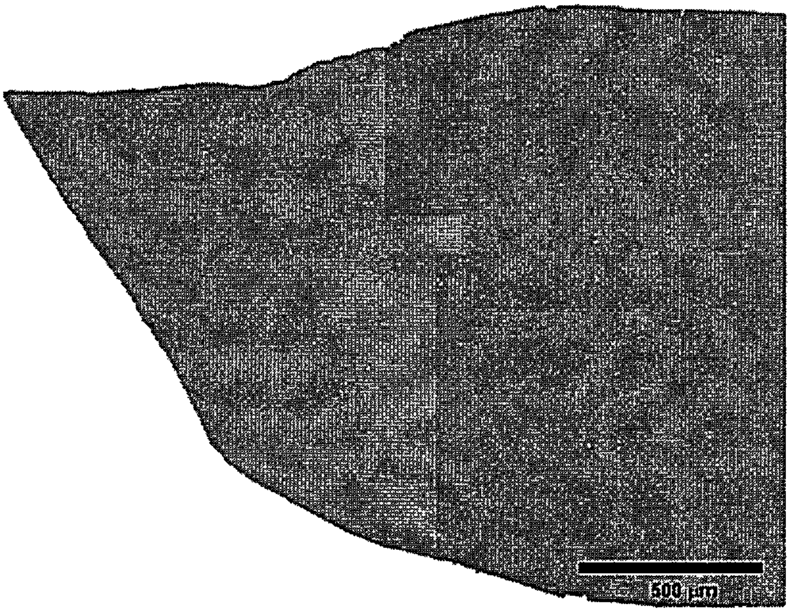

Figure 4.34: Composite image of the necked region of the low-Fe 6111 T4 alloy tested at 250 MPa showing shear MVC failure.

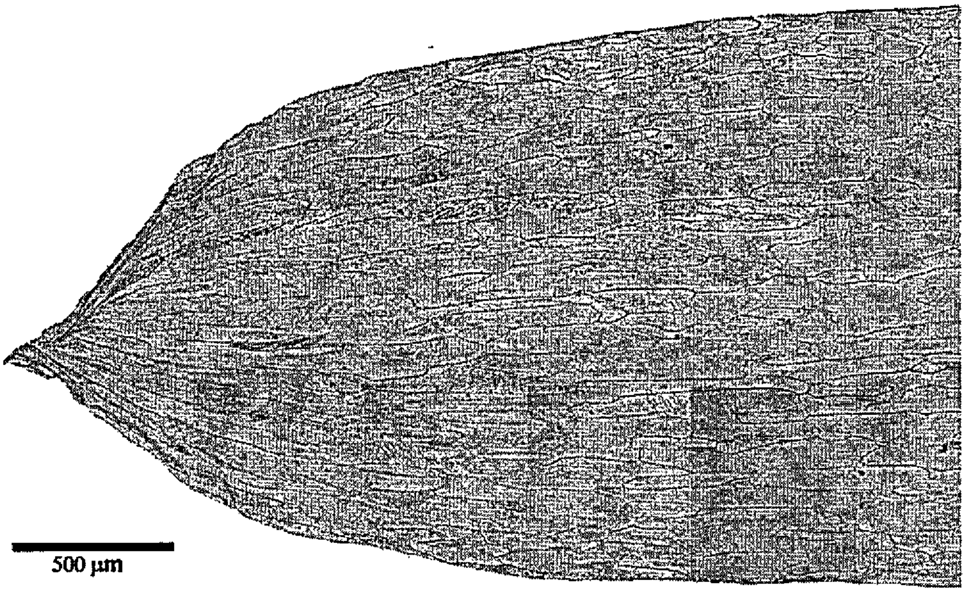

Figure 4.35: Composite image of the necked region of the low-Fe 6111 T4 alloy tested at 500 MPa showing ductile rupture failure.

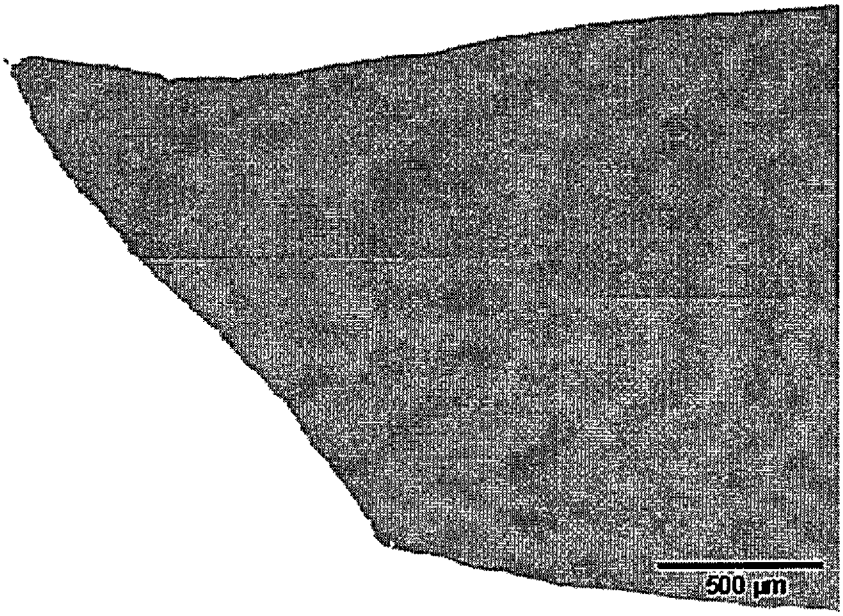

Figure 4.36: Composite image of the necked region of the high-Fe 6111 T4 alloy tested at 0.1 MPa showing shear MVC failure.

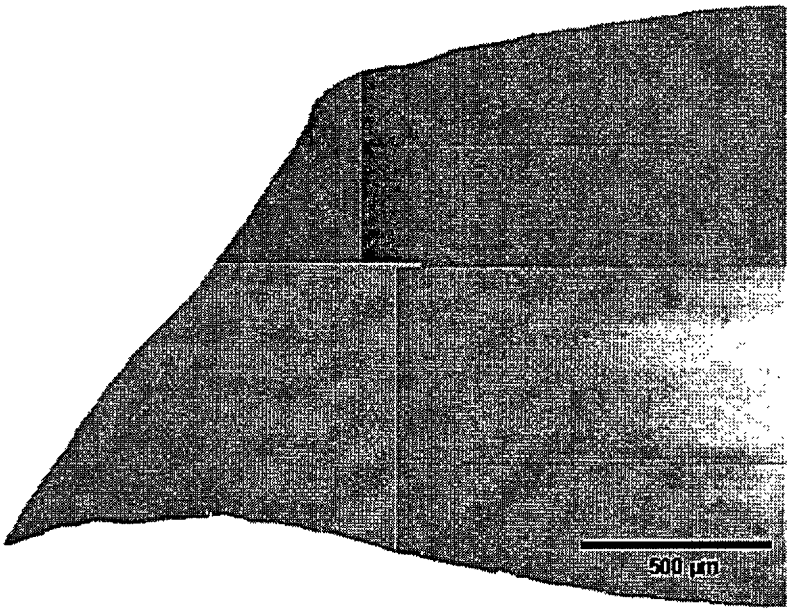

Figure 4.37: Composite image of the necked region of the high-Fe 6111 T4 alloy tested at 125 MPa showing shear MVC failure.

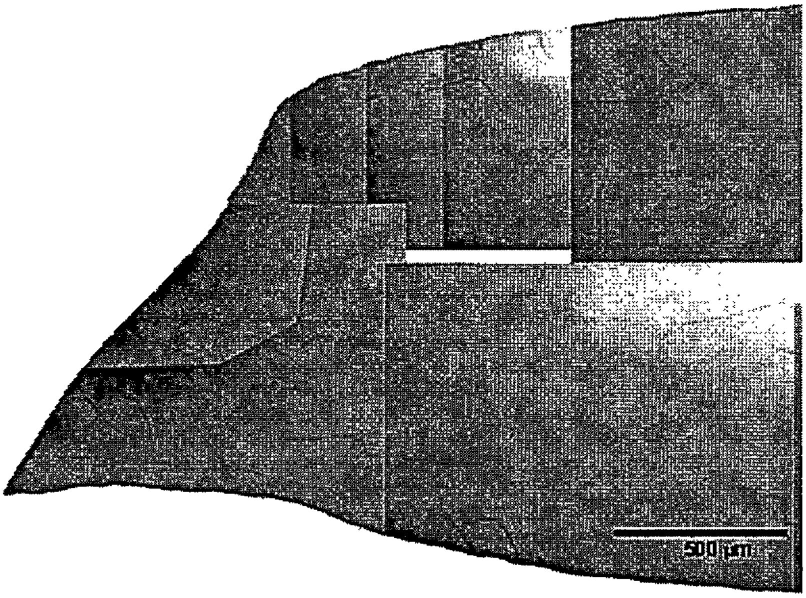

Figure 4.38: Composite image of the necked region of the high-Fe 6111 T4 alloy tested at 250 MPa showing shear MVC failure.

Figure 4.39 and Figure 4.40 show SEM micrographs of the fracture surfaces of both the T4 samples tested at 0.1 and 125 MPa. Both show extensive voiding, with an apparent reduction in the average void size with increasing superimposed hydrostatic pressures, indicating a reduction in void growth and damage in the samples. Sheeting of the voids is clearly visible for the high-Fe sample tested at 125 MPa, though some directional elongation of voids is visible for all samples. In Figure 4.41, the presence of shear is clearly evident, appearing as rows of horizontal lines running up the side of the sample, corresponding to grain scale slip intruding on the outer surface. Of note is the degree of ductility of the voids in the low versus the high-Fe samples, where the low-Fe samples have much more highly developed voids on the fracture surface.

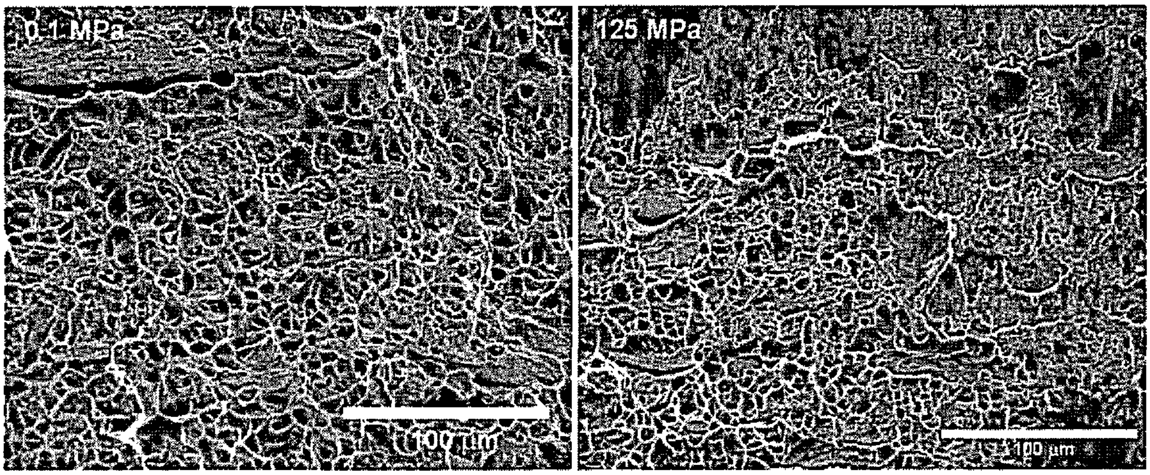

Figure 4.39: SEM image of the low-Fe 6111 T4 alloy tested at 0.1 and 125 MPa. Extensive voiding on the fracture surface is apparent, along with a reduction in void size with pressure.

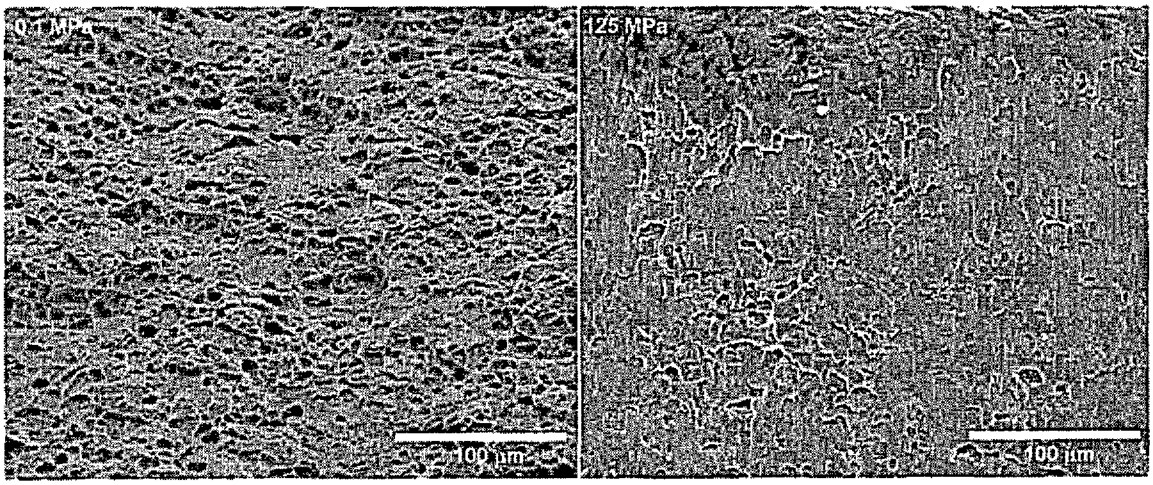

Figure 4.40: SEM image of the high-Fe 6111 T4 alloy tested at 0.1 and 125 MPa. Extensive voiding on the fracture surface is apparent, along with a reduction in void size with pressure and more severe shearing.

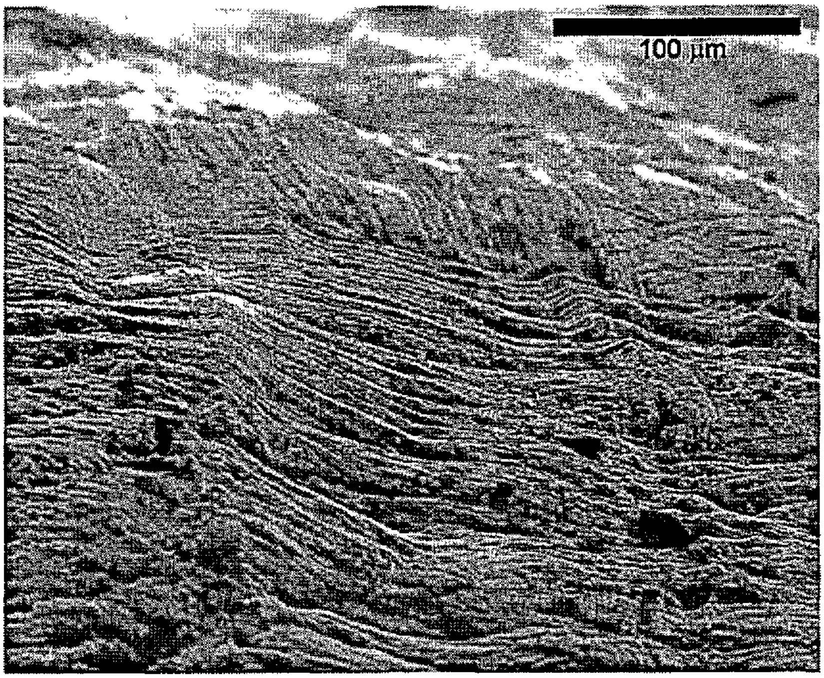

Figure 4.41: SEM image of the low-Fe 6111 T4 alloy tested at 500 MPa.

A major change in fracture is evident for the low-Fe samples when tested in the T6 condition where the heat treatment causes a transition from shear MVC to intergranular fracture, Figure 4.42 and Figure 4.43. Necking is almost non-existent in the sample. Ductility in the form of voids, is apparent at the edges of fractured grains, indicating they are likely the origin of the failure, as is the presence of grain scale shearing, Figure 4.44. Figure 4.45 shows the penetration of intergranular cracks into the sample. Evident is the redirection of these cracks along grain boundaries, and significant grain boundary separation.

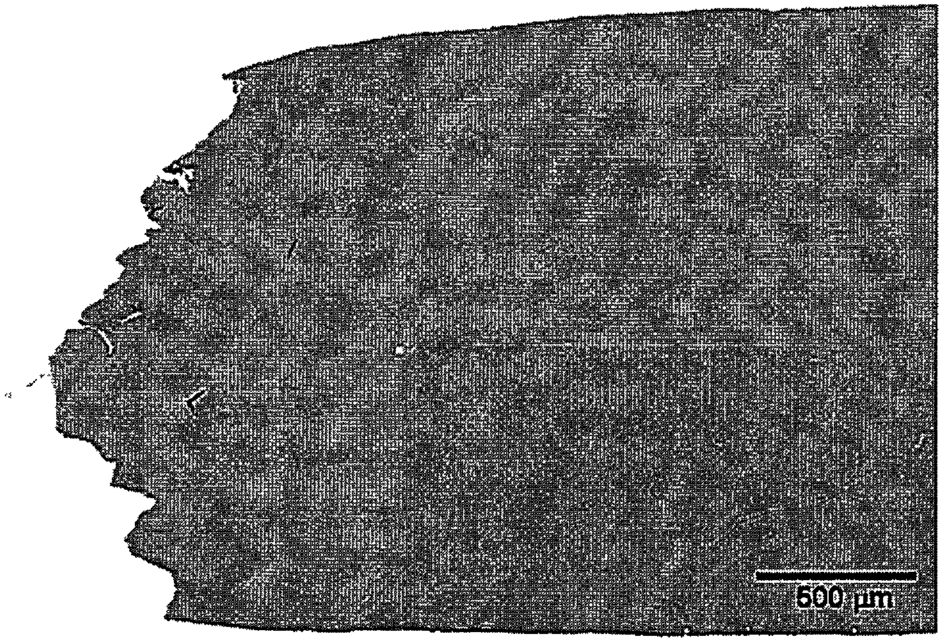

Figure 4.42: Composite image of the necked region of the low-Fe 6111 T6 alloy tested at 0.1 MPa showing intergranular failure.

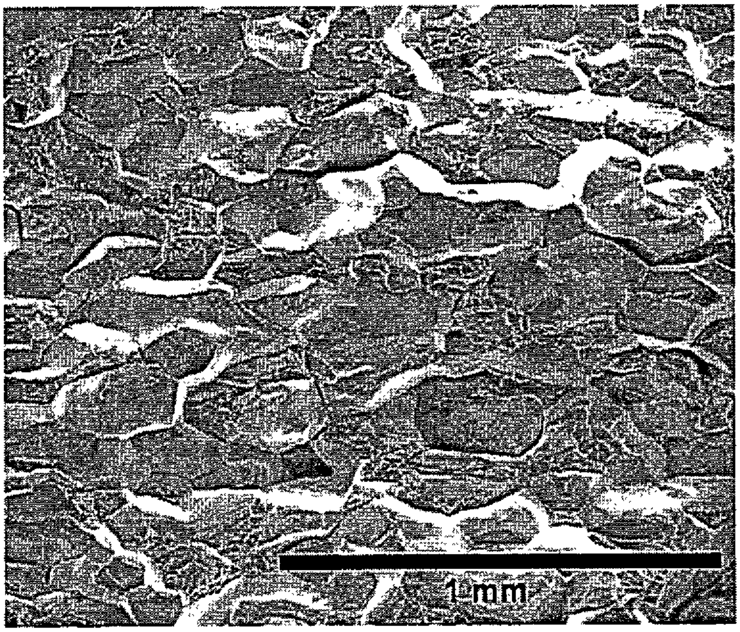

Figure 4.43: SEM image of the low-Fe 6111 T6 alloy tested at 0.1 MPa.

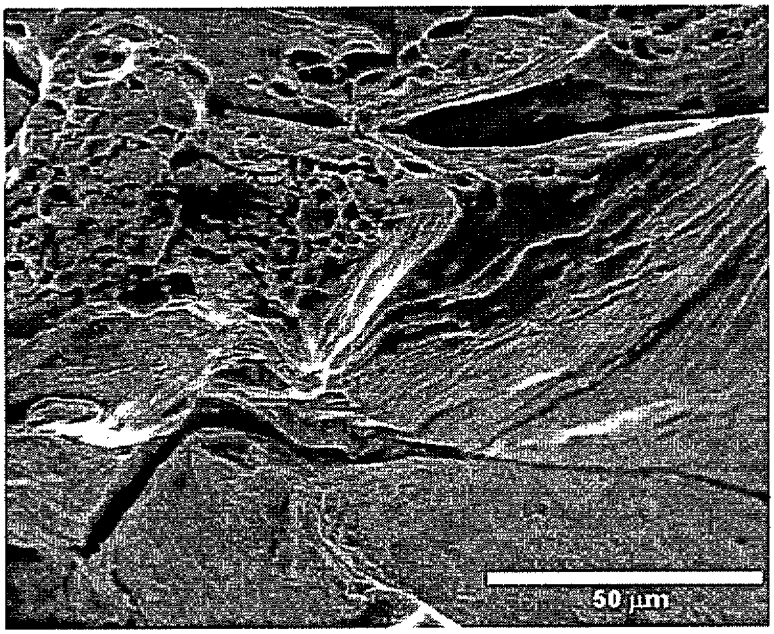

Figure 4.44: SEM image of the low-Fe 6111 T6 alloy tested at 0.1 MPa. Evidence of grain scale shearing and voiding at edge of grains and on grain surfaces is visible.

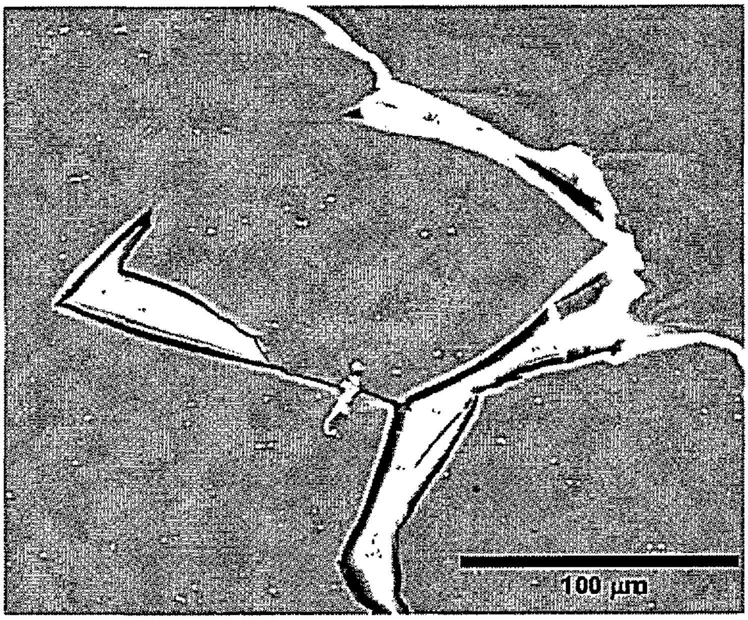

Figure 4.45: SEM image of the low-Fe 6111 T6 alloy tested at 0.1 MPa showing intergranular cracks penetrating in from the fracture surface.

With increasing pressure, a transition from intergranular to shear MVC occurred. At 125 MPa, the fracture surface starts to transition from failing perpendicular to the tensile axis to a shear failure, Figure 4.46. Intergranular cracking within the sample was not as pronounced, nor were cracks observed penetrating into the sample from the fracture surface. The grains were less clearly delineated than in the sample tested at 0.1 MPa, and more voiding was apparent on grain boundaries, Figure 4.47. At 250 MPa, Figure 4.48, the transition to a shear failure is complete, though the irregularity of the fracture surface indicates some intergranularity still remains. Figure 4.49 shows the fracture surface of the 250 MPa sample. Significantly less intergranular fracture is apparent, with a corresponding increase in the presence of voiding, where the fracture surface is heterogeneous, showing distinct regions of intergranular fracture and regions of voids sheeting.

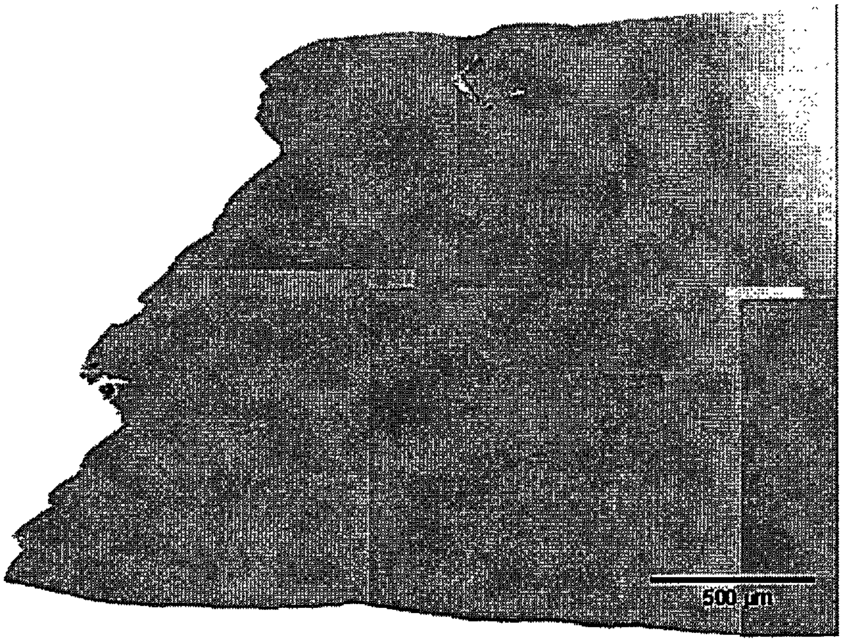

Figure 4.46: Composite image of necked region of the low-Fe 6111 T6 alloy tested at 125 MPa showing intergranular and shear failure.

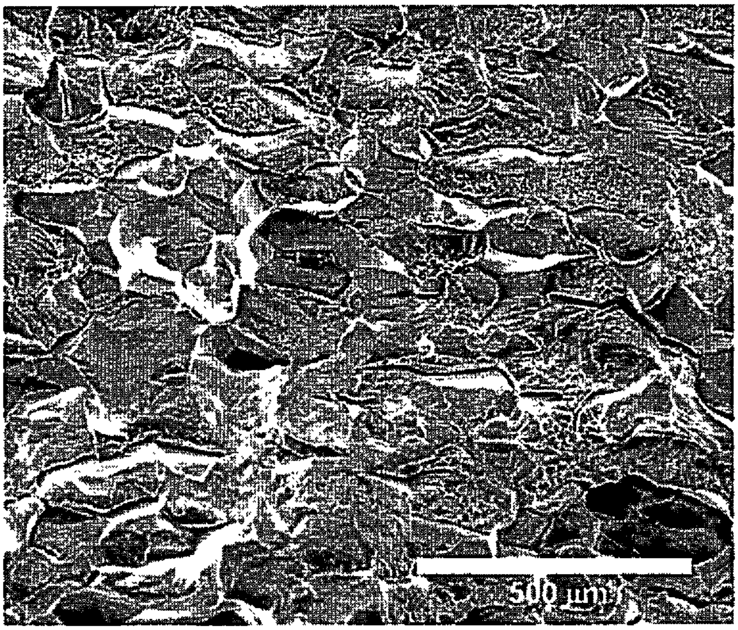

Figure 4.47: SEM image of the low-Fe 6111 T6 alloy tested at 125 MPa.

Figure 4.48: Composite image of the necked region of the low-Fe 6111 T6 alloy tested at 250 MPa showing shear MVC failure with some intergranularity

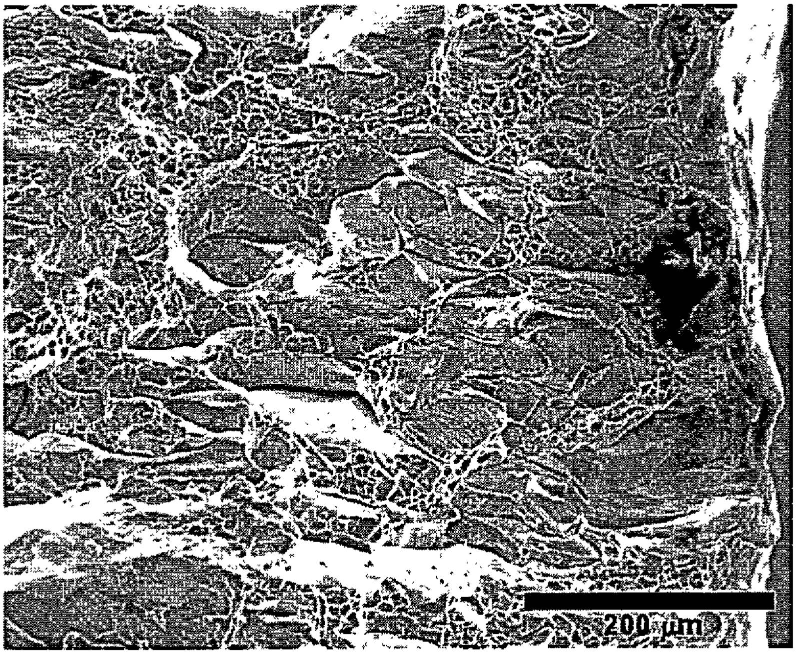

Figure 4.49: SEM image of the low-Fe 6111 T6 alloy tested at 250 MPa.

The high-Fe T6 alloy consistently showed shear MVC failure at all pressures tested, except for the 125 MPa test where it failed by a cup and cone mode, Figure 4.50 to Figure 4.53. Necking of the samples became more severe with increasing pressures, and it is interesting to note how much more the high-Fe samples necked in comparison to the low-Fe samples, the high-Fe samples appearing significantly more ductile. An examination of the fracture surface reveals little noticeable difference between any of the high-Fe T6 samples in terms of void size, Figure 4.54 to Figure 4.57. All samples showed directional void growth, corresponding to a void sheeting process.

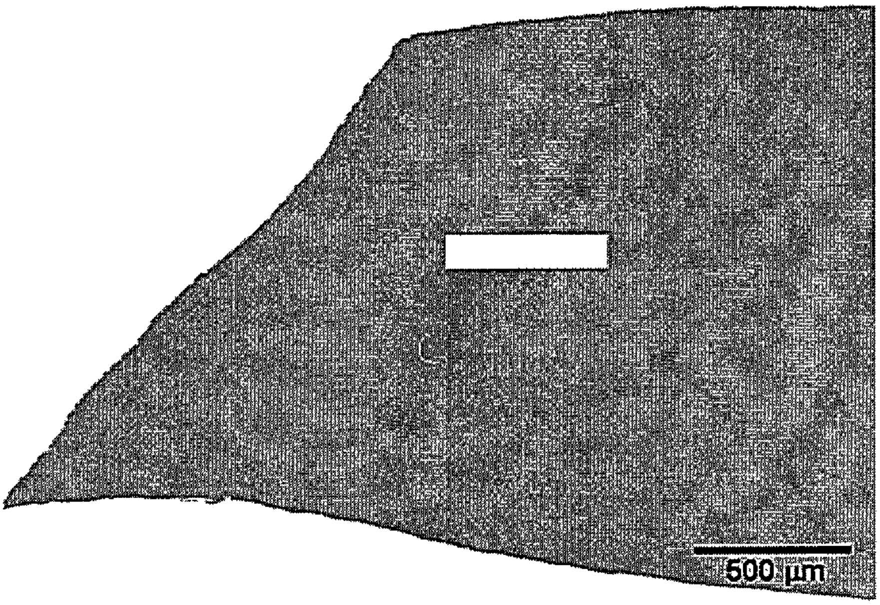

Figure 4.50: Composite image of necked region of the high-Fe 6111 T6 alloy tested at 0.1 MPa showing shear MVC failure.

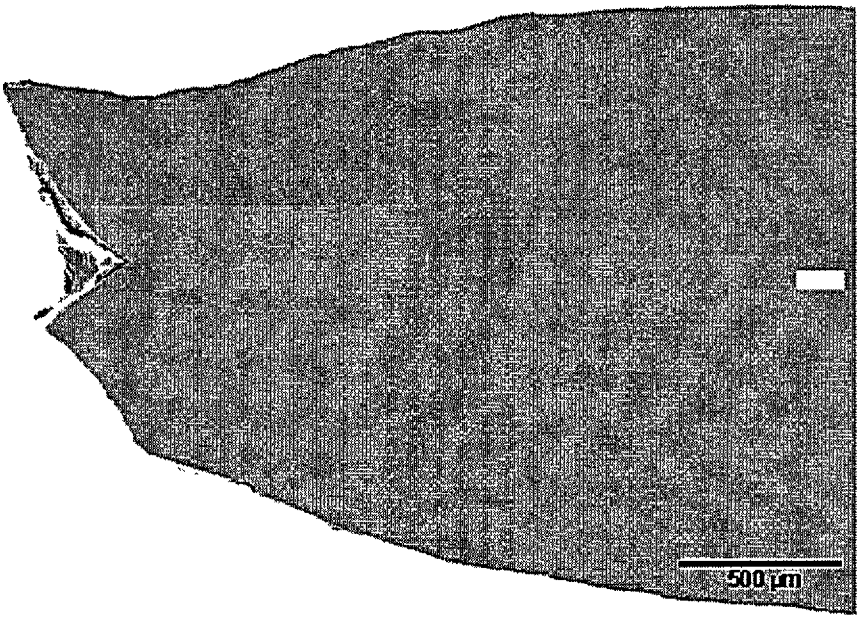

Figure 4.51: Composite image of the necked region of the high-Fe 6111 T6 alloy tested at 125 MPa showing shear MVC and cup and cone failure.

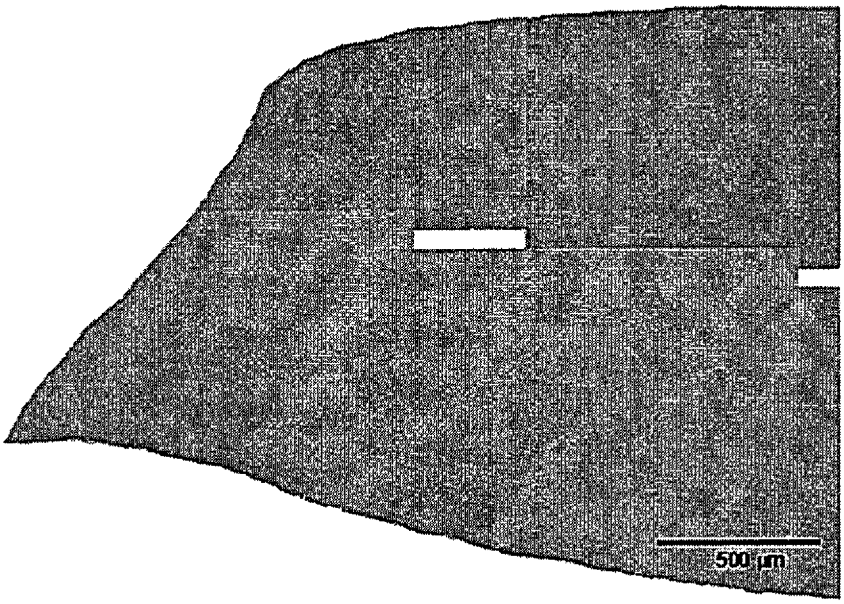

Figure 4.52: Composite image of the necked region of the high-Fe 6111 T6 alloy tested at 250 MPa showing shear MVC failure.

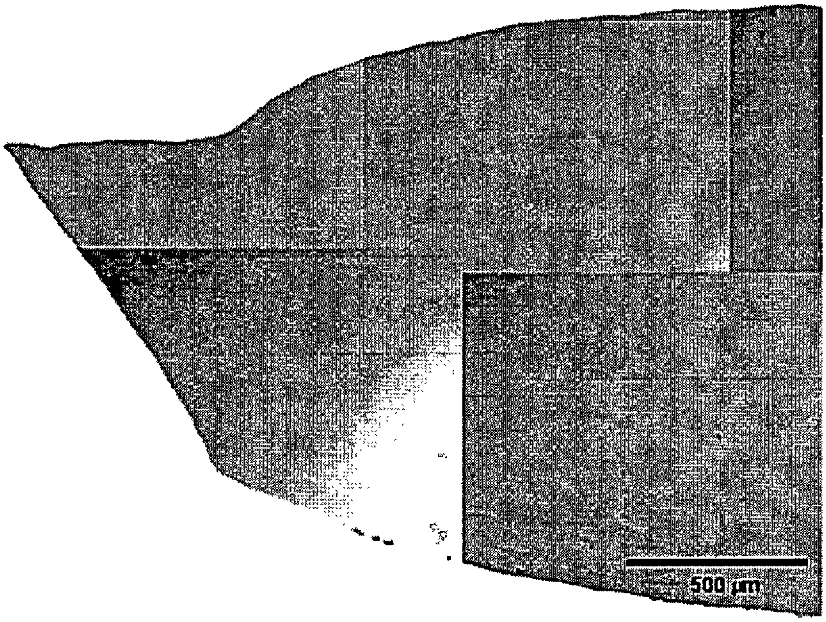

Figure 4.53: Composite image of the necked region of the high-Fe 6111 T6 alloy tested at 500 MPa showing shear MVC failure.

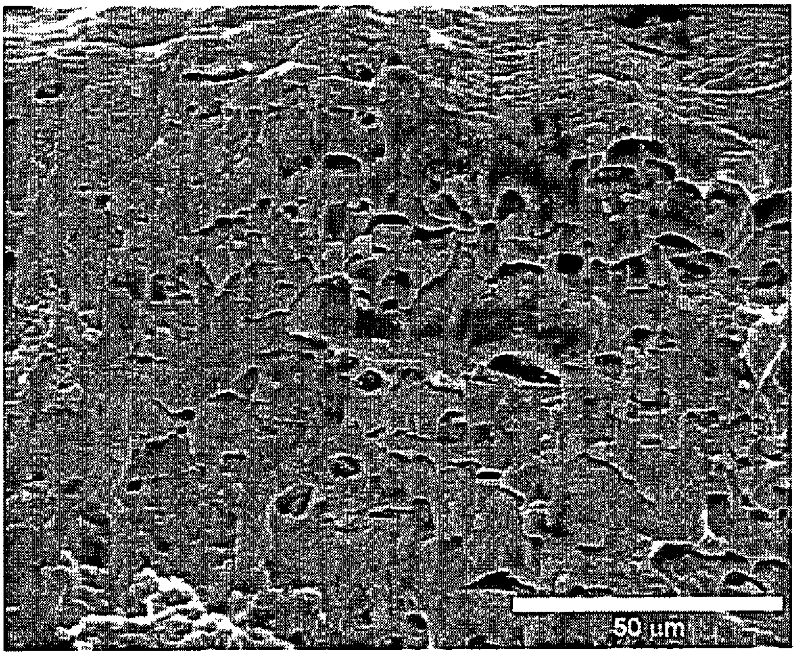

Figure 4.54: SEM image of the high-Fe 6111 T6 alloy tested at 0.1 MPa.

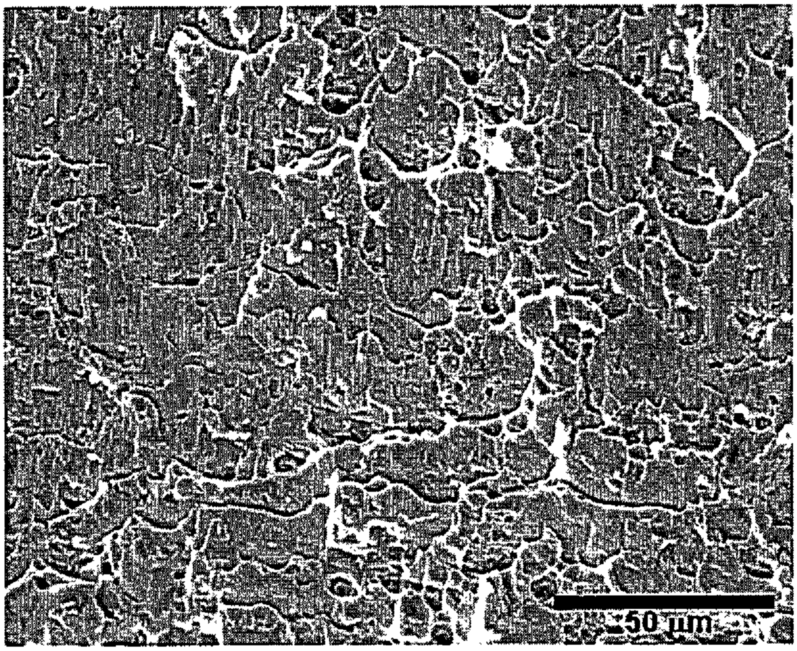

Figure 4.55: SEM image of the high-Fe 6111 T6 alloy tested at 125 MPa.

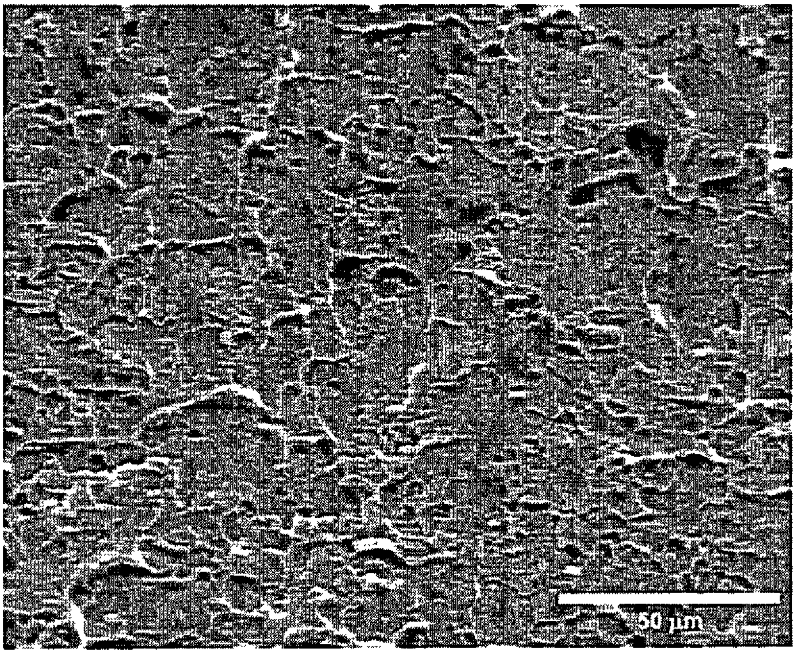

Figure 4.56: SEM image of the high-Fe 6111 T6 alloy tested at 250 MPa.

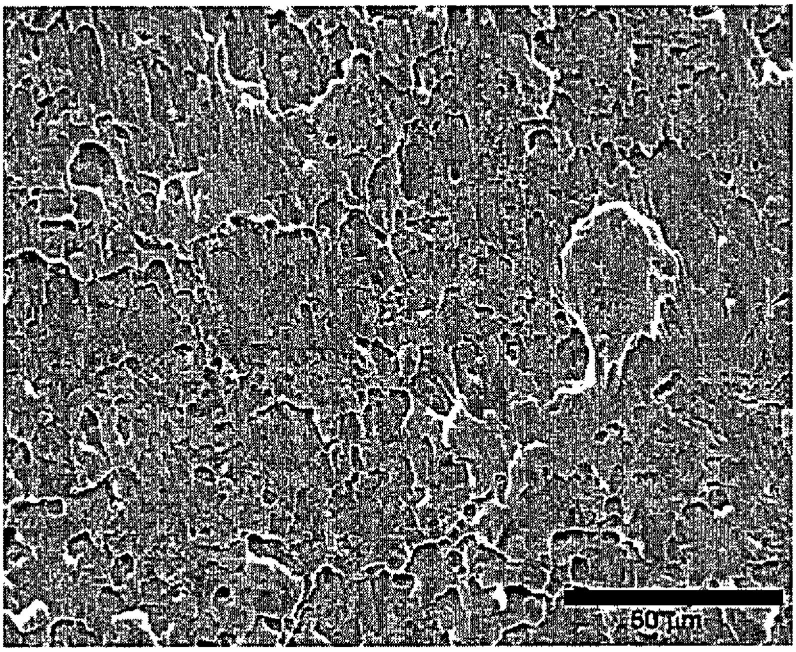

Figure 4.57: SEM image of the high-Fe 6111 T6 alloy tested at 500 MPa.

A summary of the various fracture modes and associated test conditions for the 6111 alloys tested is shown in Table 4.6.

Table 4.6: Summary of the tests performed on the 6111 alloy and the associated fracture modes

Material	Pressure (MPa)	Failure Mode
Low-Fe T4	0.1	Shear MVC
Low-Fe T4	125	Shear MVC
Low-Fe T4	250	Shear MVC
Low-Fe T4	500	Ductile Rupture
High-Fe T4	0.1	Shear MVC
High-Fe T4	125	Shear MVC
High-Fe T4	250	Shear MVC
Low-Fe T6	0.1	Intergranular
Low-Fe T6	125	Intergranular/Shear MVC[1]
Low-Fe T6	250	Shear MVC/Intergranular[1]
High-Fe T6	0.1	Shear MVC
High-Fe T6	125	Shear MVC
High-Fe T6	250	Shear MVC
High-Fe T6	500	Shear MVC

1 Order represents overall predominance

4.2.4 Reduction in Area (RA) measurements

Reduction in area measurements for all 6111 samples tested are presented in Table 4.7. Error values have been calculated as described in the Damage Analysis section for the 5754 alloy.

Table 4.7: Reduction in area measurements for 6111 alloys

Materials	Pressure (MPa)	Reduction in Area (%)
Low-Fe T4	0.1	53 ± 0.34
Low-Fe T4	125	61 ± 0.34
Low-Fe T4	250	69 ± 0.32
Low-Fe T4	500	100 ± 0
High-Fe T4	0.1	44 ± 0.36
High-Fe T4	125	52 ± 0.35
High-Fe T4	250	64 ± 0.33
Low-Fe T6	0.1	29 ± 0.37
Low-Fe T6	125	39 ± 0.36
Low-Fe T6	250	64 ± 0.33
High-Fe T6	0.1	43 ± 0.36
High-Fe T6	125	59 ± 0.34
High-Fe T6	250	62 ± 0.34
High-Fe T6	500	70 ± 0.33

The results demonstrate the expected trend of an increasing reduction in area with increasing superimposed pressure. The T4 samples showed an overall decrease in ductility with increasing iron content. The opposite held true for the T6 samples for which the low-Fe samples showed lower ductility than the high-Fe samples, due to the presence of the intergranular fracture mode. A sharp jump in ductility occurred for the low-Fe T6 material between 125 and 250 MPa, corresponding to the transition from intergranular failure to shear MVC as the predominant fracture mode. Consistent increases in ductility were seen for the high-Fe T6 alloy with pressure, however it never achieved ductile rupture as was observed for the low-Fe T4, this a result of its higher yield strength.

4.2.5 Damage Analysis

Figure 4.58 to Figure 4.61 show the measurements of damage for the 6111 alloys as a function of strain. As with the 5754 alloys, the estimated error in the value of damage was 10% and 1% for the strain measurements.

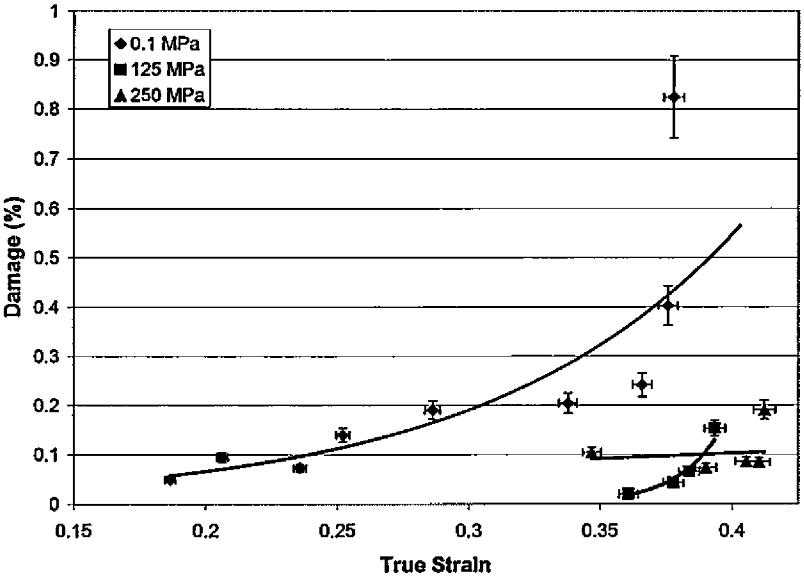

Figure 4.58: Damage (%) as a function of strain in low-Fe 6111 T4 alloys.

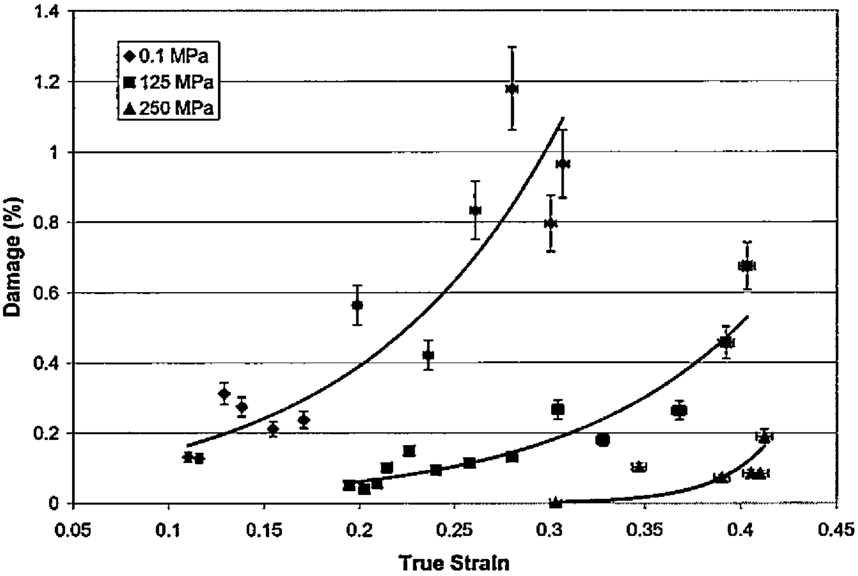

Figure 4.59: Damage (%) as a function of strain in high-Fe 6111 T4 alloys.

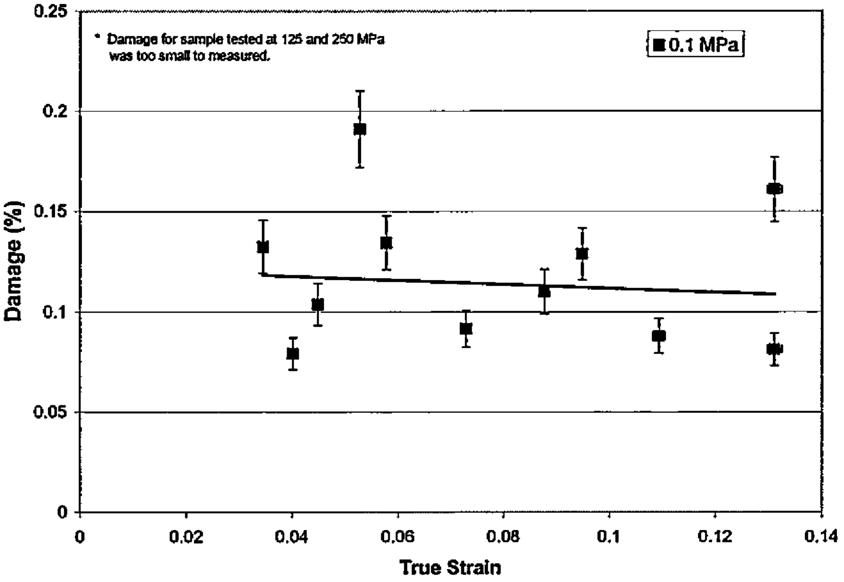

Figure 4.60: **Damage (%) as a function of strain in low-Fe 6111 T6 alloys.**

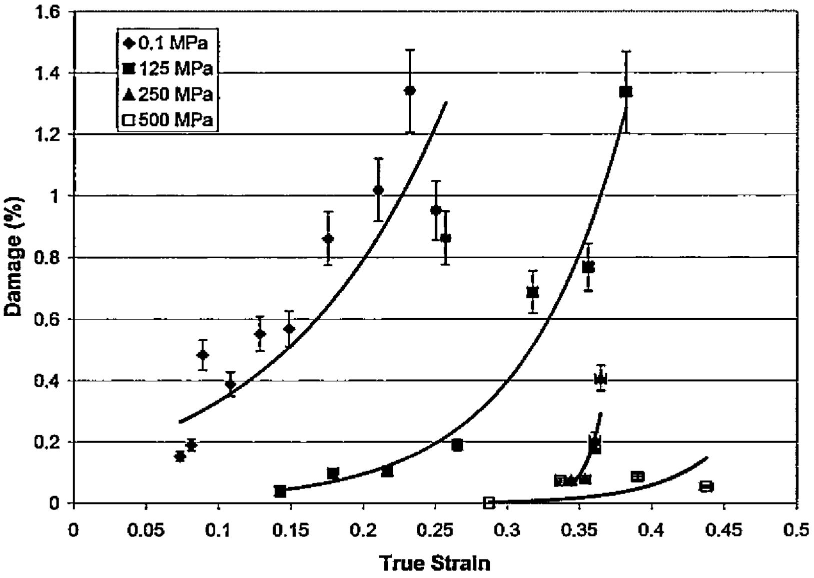

Figure 4.61: Damage (%) as a function of strain in high-Fe 6111 T6 alloys.

All of the samples tested showed a decrease in the amount of damage with increasing superimposed hydrostatic pressure. The low-Fe T4 samples showed almost no damage at 125 and 250 MPa, indicating damage mechanisms within the material are being suppressed. A steady increase in the amount of post-necking strain (true strain) is exhibited with increasing pressure. Much higher levels of damage were present in the high-Fe T4 samples for the 0.1 and 125 MPa tests, a result of the higher intermetallic content. Damage values for both low and high-Fe T4 samples at 250 MPa are very similar indicating this is the above the cut-off pressure that will allow damage to form. In addition, the post-necking strain in the high-Fe samples appears to be more sensitive to the presence of damage, with a more drastic increase in necking with increasing superimposed pressure than seen in the low-Fe T4 samples.

Little damage was observed in the low-Fe T6 materials at any pressure tested, though it should be noted that the results presented did not include the presence of the large intergranular cracks. When these are included the results are heavily skewed, with a large increase in the amount of damage present for the 0.1 MPa sample, Figure 4.62. Post-necking strain in the sample did not increase for tests between 0.1 and 125 MPa. However, a sharp jump occurred at 250 MPa, corresponding to the change in fracture mode from intergranular to shear MVC.

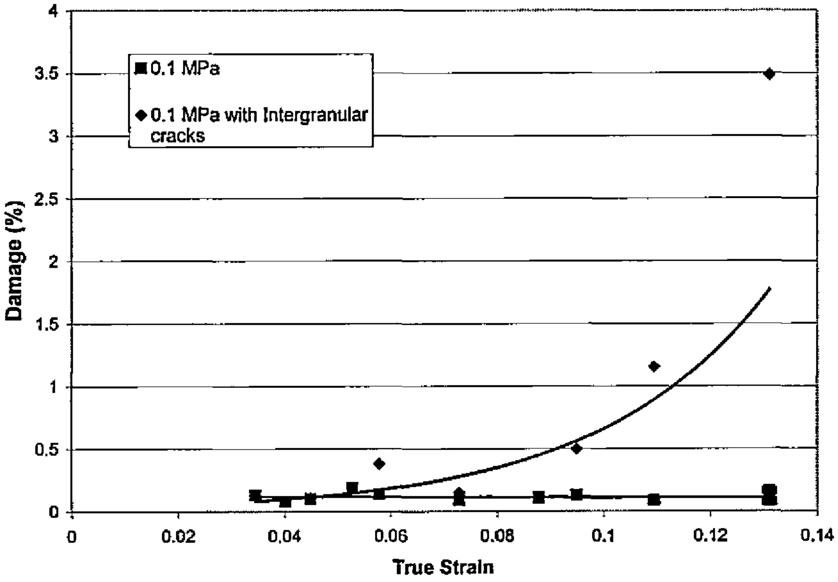

Figure 4.62: Damage (%) as a function of strain in the low-Fe 6111 T6 alloy, showing values both including and not including the intergranular cracks.

The high-Fe T6 materials showed extensive damage, typically higher than that exhibited by the high-Fe T4 material. Damage levels remained consistent for both 0.1 and 125 MPa, but decreased with increasing superimposed pressure to 500 MPa, where damage was almost immeasurable. Post-necking strain steadily increased with pressure to a maximum value occurring at 500 MPa.

Figure 4.63 to Figure 4.67 show images of damage for the 6111-T4 samples. Clearly delineated voids and associated particles are visible in both the low and high-Fe variants however, the iron intermetallic content is noticeably greater in the high-Fe alloy. Shearing of the voids in a characteristic "S" pattern can be seen in the low-Fe alloy tested at 0.1 MPa, Figure 4.63. In Figure 4.64, a small amount of damage in comparison to the sample tested at 0.1 MPa can be seen for the sample tested at 250 MPa. Large quantities of damage are visible in the high-Fe T4 sample tested at 0.1 MPa, with voids tending to form in regions of particle clusters, particularly on large particles or those with sharp facets, Figure 4.65. Cracking of large particles is also clearly evident. The distinct "S" pattern of void shearing seen in the low-Fe alloys is not apparent. However, directional elongation of voids is clearly evident parallel to the fracture surface, corresponding to a shearing process.

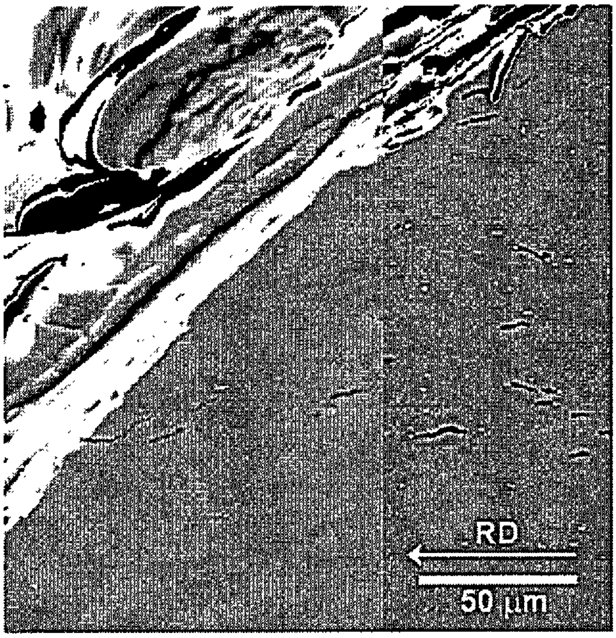

Figure 4.63: SEM image of damage near the fracture surface of the low-Fe 6111 T4 alloy tested at 0.1 MPa.

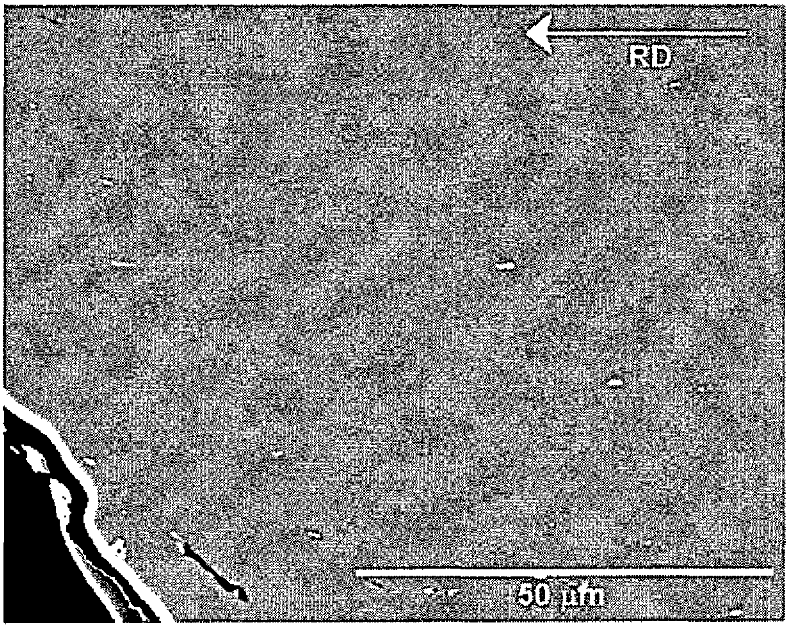

Figure 4.64: SEM image of damage near the fracture surface of the low-Fe 6111 T4 alloy tested at 250 MPa.

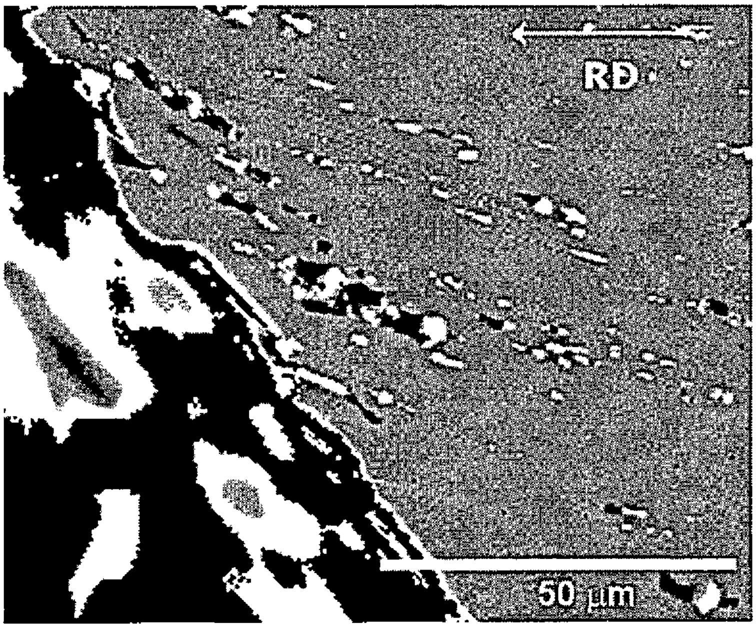

Figure 4.65: SEM image of damage near the fracture surface of the high-Fe 6111 T4 alloy tested at 0.1 MPa.

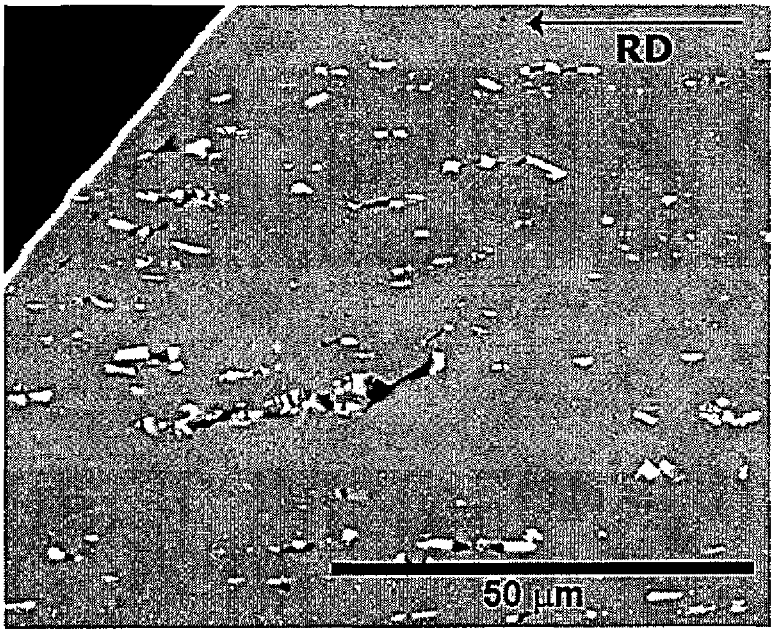

Figure 4.66: SEM image of damage near the fracture surface of the high-Fe 6111 T4 alloy tested at 125 MPa.

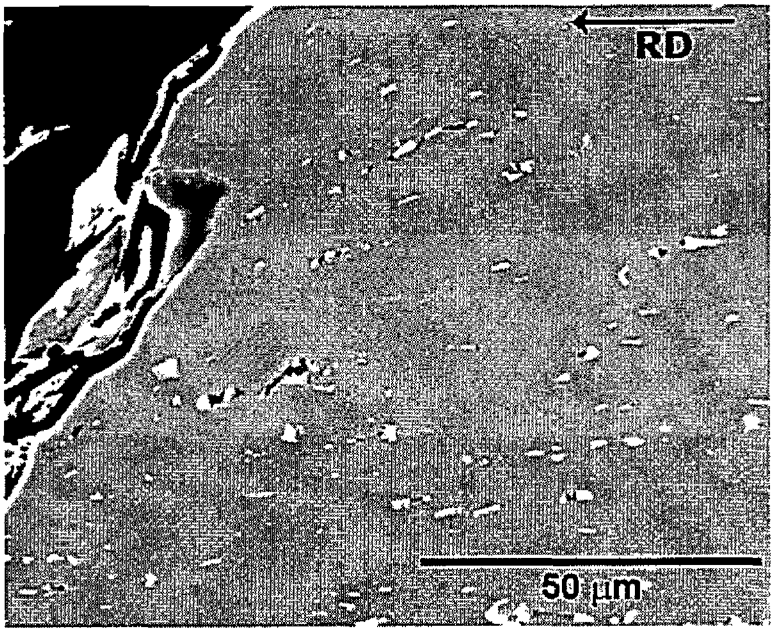

Figure 4.67: SEM image of damage near the fracture surface of the high-Fe 6111 T4 alloy tested at 250 MPa.

Damage in the low-Fe T6 sample is predominantly the result of large intergranular cracks which are typically between 100 to 200 µm in size, on the order of the grain size. Damage at second phase particles is slight, almost immeasurable as shown in the damage analysis section, Figure 4.68 and Figure 4.69. Grain scale shearing is evident adjacent to a crack as shown in the enlarged section of Figure 4.70.

With increasing pressure, the damage is reduced to even lower levels than that present at 0.1 MPa. Alignment of the particle stringers is visible in the sample tested at 250 MPa, along with elongation of the particles in shear related directions, a result of the more extensive deformation undergone by the sample.

Damage is much more severe in the high-Fe T6 samples due to the higher overall iron intermetallic content, Figure 4.71 to Figure 4.74. As with the T4 samples, voids are predominantly associated with larger and/or more angular particles, which have either cracked or decohered from the matrix. The sample tested at 125 MPa shows a large central void that has bifurcated, indicating operation of conjugate shear systems. Damage levels are reduced with increasing pressure, with the sample tested at 500 MPa, showing little damage. Definite reorientation of particle stringers is apparent in both the 250 and 500 MPa samples (note that typically higher magnifications were required to capture damage as pressure was increased, due to the decrease in both the amount and the overall size of voids).

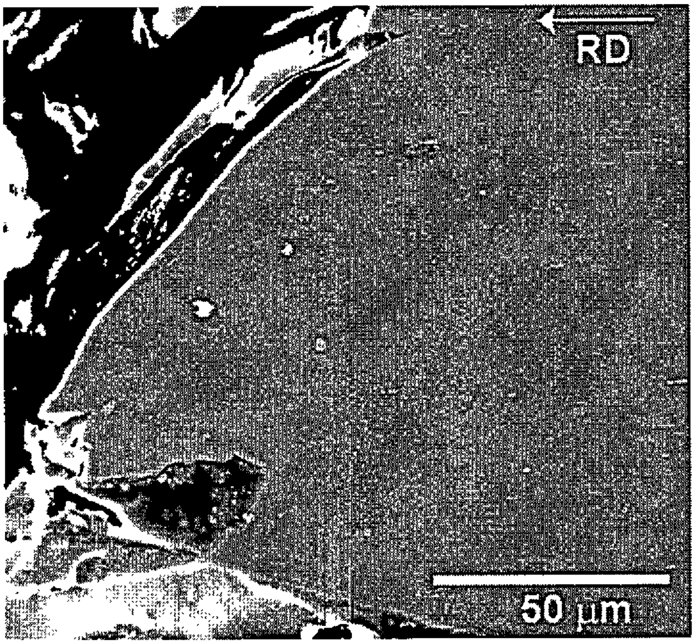

Figure 4.68: SEM image of damage near the fracture surface of the low-Fe 6111 T6 alloy tested at 125 MPa.

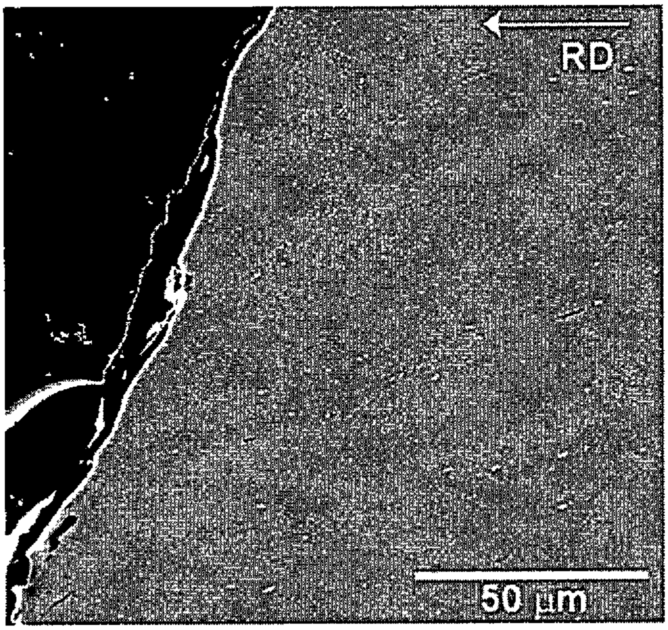

Figure 4.69: SEM image of damage near the fracture surface of the low-Fe 6111 T6 alloy tested at 250 MPa.

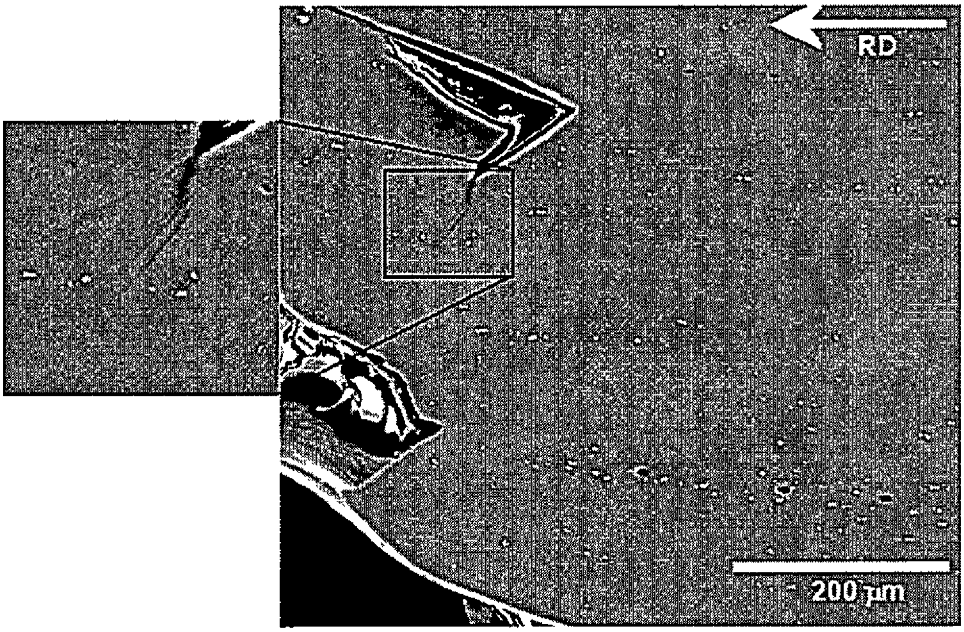

Figure 4.70: SEM image of damage near the fracture surface of the low-Fe 6111 T6 alloy tested at 125 MPa showing shearing at the crack tip.

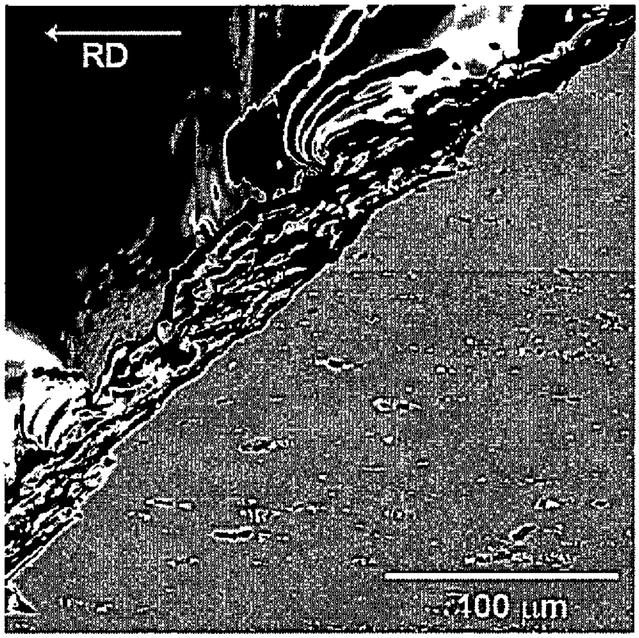

Figure 4.71: SEM image of damage near the fracture surface of the high-Fe 6111 T6 alloy tested at 0.1 MPa.

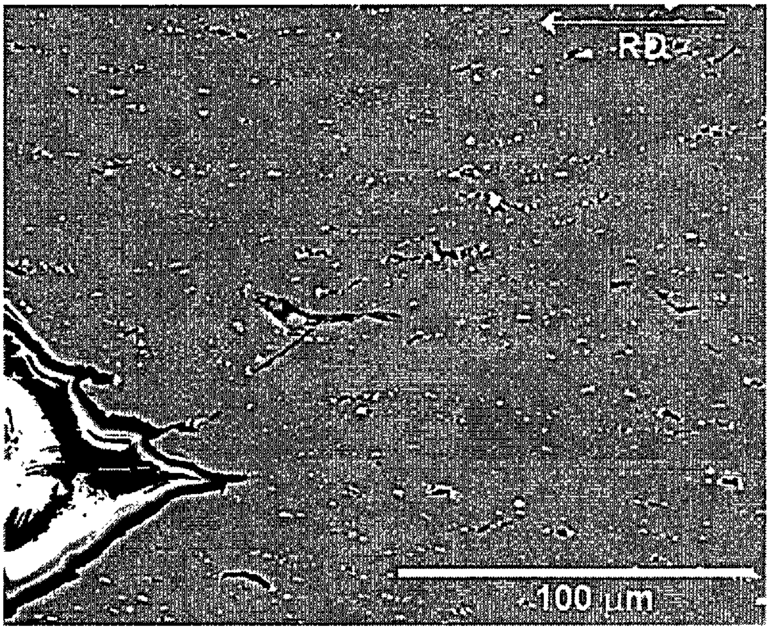

Figure 4.72: SEM image of damage near the fracture surface of the high-Fe 6111 T6 alloy tested at 125 MPa.

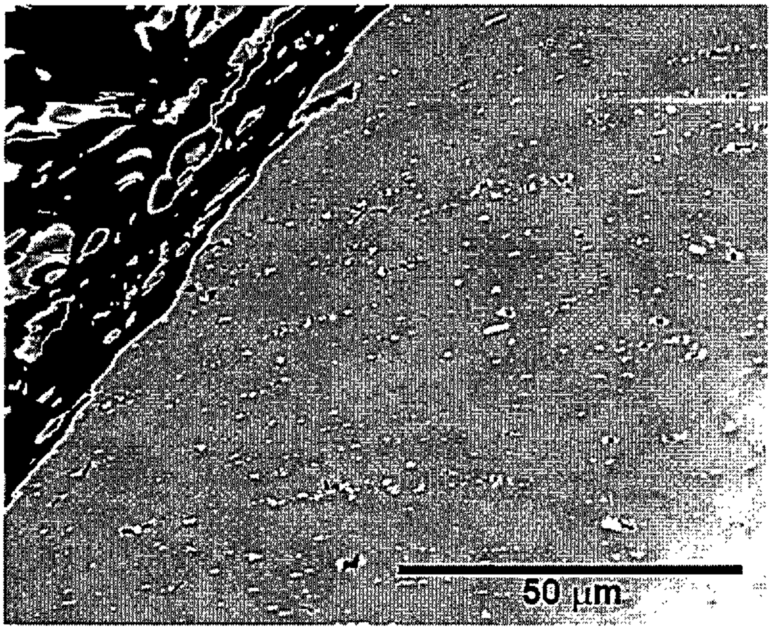

Figure 4.73: SEM image of damage near the fracture surface of the high-Fe 6111 T6 alloy tested at 250 MPa.

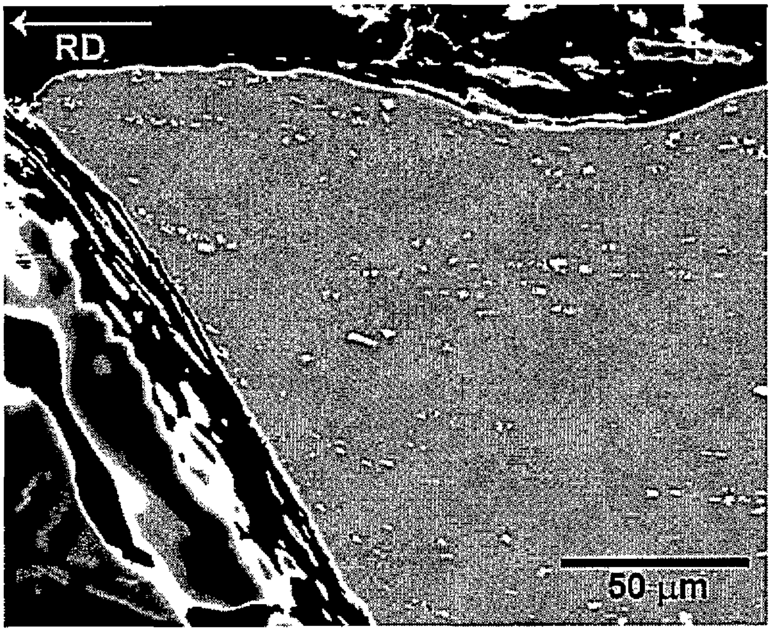

Figure 4.74: SEM image of damage near the fracture surface of the high-Fe 6111 T6 alloy tested at 500 MPa.

4.2.6 Shearing Behaviour

An extensive study was undertaken to identify both the grain-scale and large scale shearing behaviour of this alloy, with particular focus on identifying the strain at which the coordination of slip bands into sample-scale shear bands occurs. Optical micrographs were taken of samples etched to reveal the shearing when observed under Nomarski polarized light, and composite images of the entire necked region were constructed. These images will be presented in the following section, along with more magnified views when elucidation of important features is required.

Figure 4.75 to Figure 4.77 show full composite micrographs of the necked regions of the low-Fe T4 samples tested at various pressures. Figure 4.78 to Figure 4.80 show magnified views of the same samples, both near the fracture surface within the necked region, and out of the necked region. It is apparent with increasing pressures that the severity of shear on the grain scale within the necked region increases, with the 250 MPa showing the most severe grain scale shearing. At 250 MPa, the coordination of grain scale slip into macroscopic shear bands occurred, corresponding to a true strain of approximately 0.4, slightly higher than the maximum shear obtained by the 125 MPa sample, indicating this is the critical shear for shear band formation. No apparent difference in shearing within the uniformly strained region of the samples are evident, showing pressure does not have an appreciable effect on the shearing behaviour prior to necking.

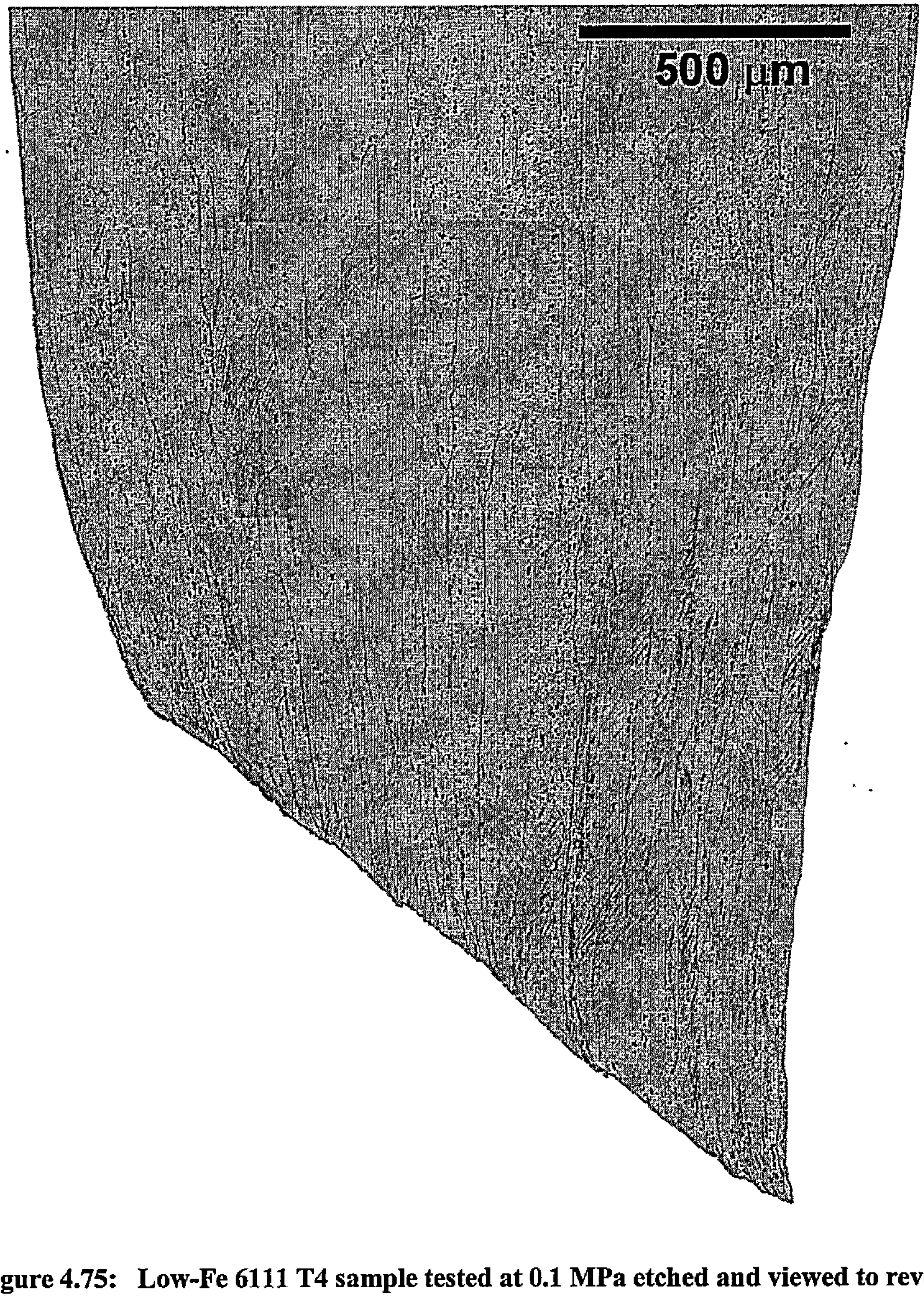

Figure 4.75: Low-Fe 6111 T4 sample tested at 0.1 MPa etched and viewed to reveal shearing and slip.

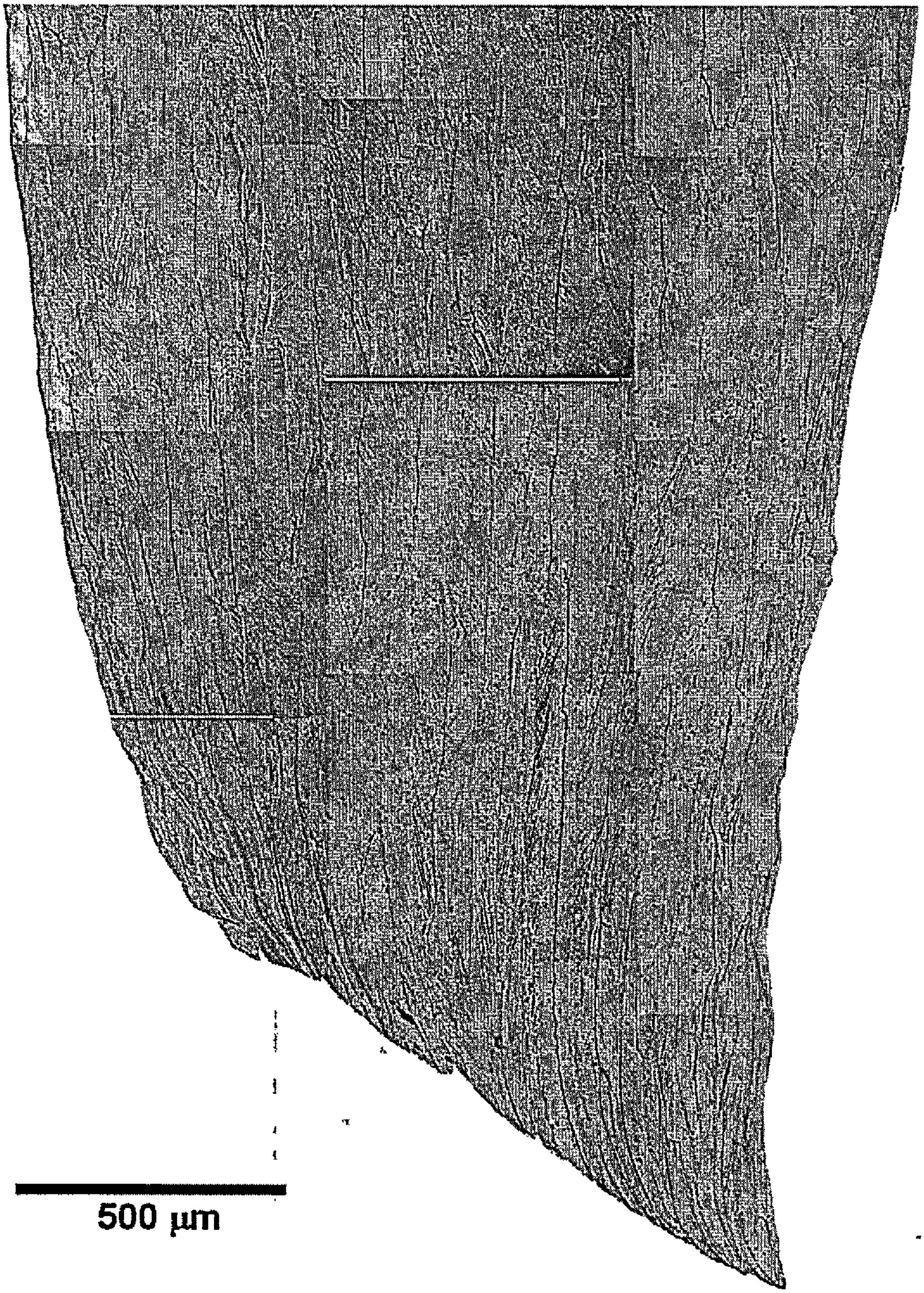

Figure 4.76: Low-Fe 6111 T4 sample tested at 125 MPa etched and viewed to reveal shearing and slip.

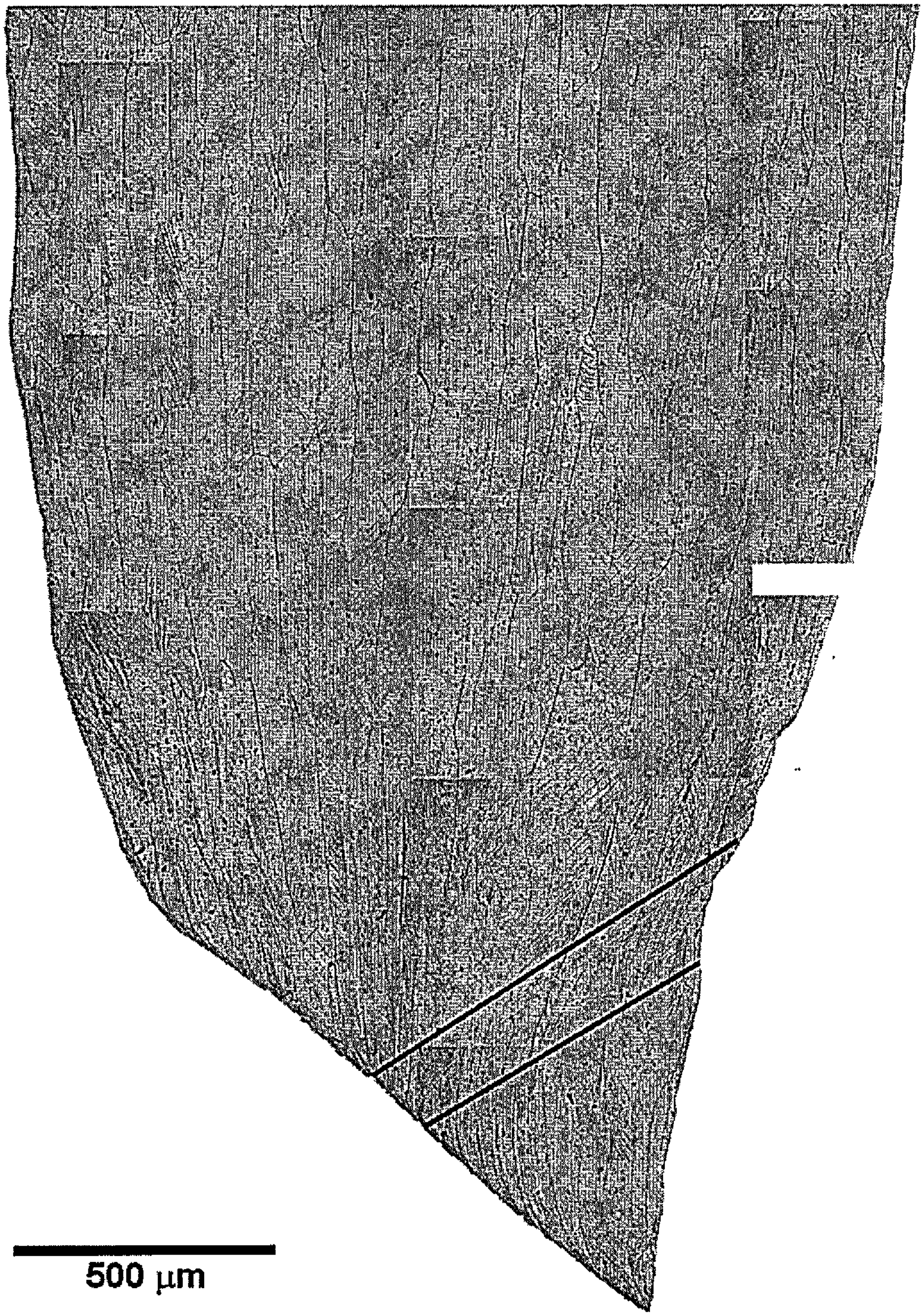

Figure 4.77: Low-Fe 6111 T4 sample tested at 250 MPa etched and viewed to reveal shearing and slip. Macroscopic shear band outlined with black lines.

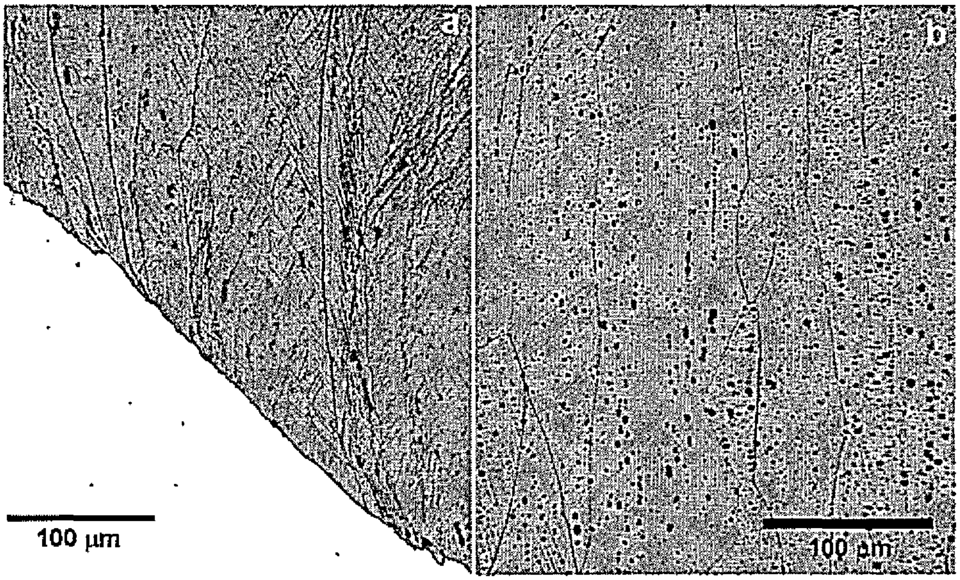

Figure 4.78: Low-Fe 6111 T4 sample tested at 0.1 MPa etched and viewed to reveal shearing and slip. a) adjacent to fracture surface, b) uniformly strained region.

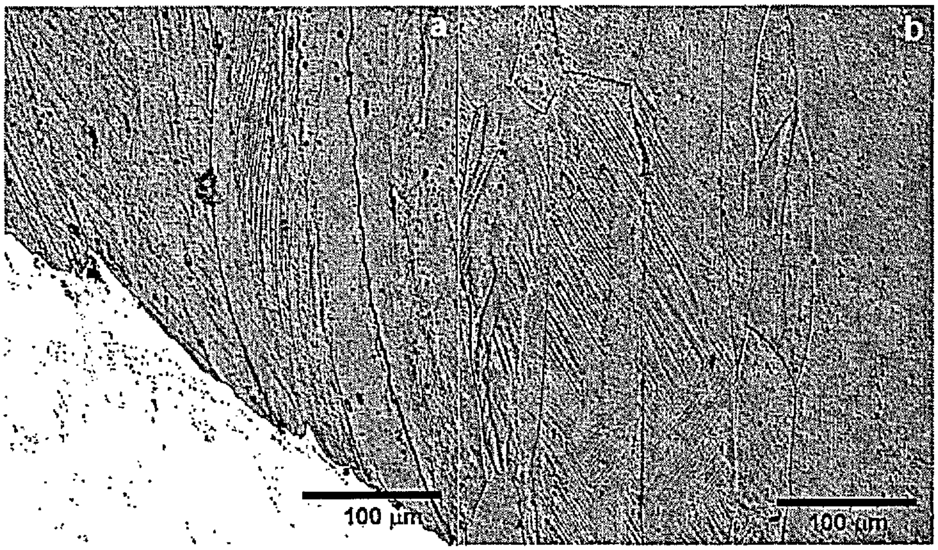

Figure 4.79: Low-Fe 6111 T4 sample tested at 125 MPa etched and viewed to reveal shearing and slip. a) adjacent to fracture surface, b) uniformly strain region.

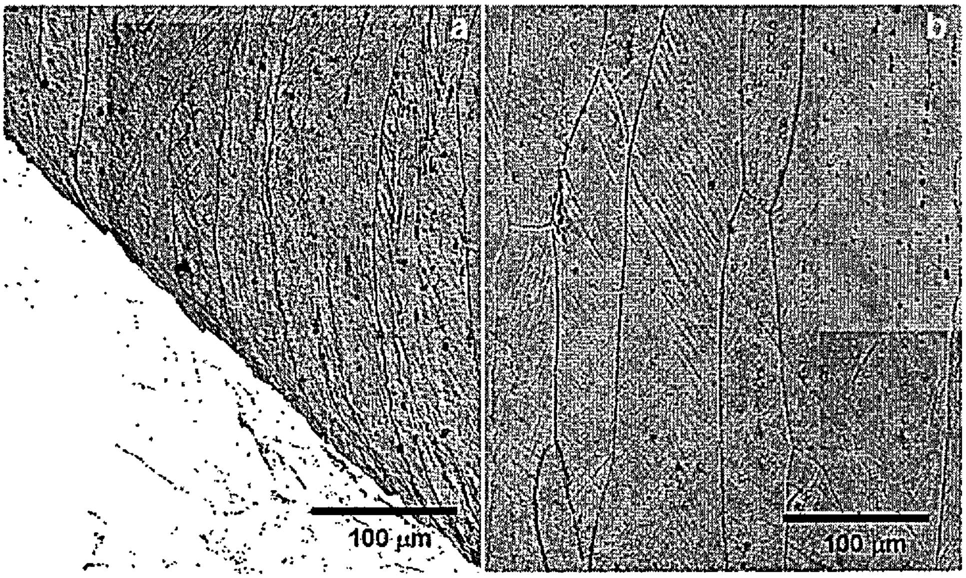

Figure 4.80: Low-Fe 6111 T4 sample tested at 250 MPa etched and viewed to reveal shearing and slip. a) adjacent to fracture surface, b) uniformly strained region.

Figure 4.81 to Figure 4.83 show full composite micrographs of the necked regions of high-Fe T4 samples tested at various pressures. Shearing on the grain scale is difficult to resolve in the samples in comparison to the low-Fe samples due to the large decrease in grain size associated with the higher iron content. However, it can be resolved at higher magnifications, Figure 4.84 and Figure 4.85. No apparent macroscopic shear bands appear to have developed, indicating the coordination of grain scale slip into shear bands is being interrupted, though some slipping across grain boundaries can be seen in the 125 MPa and 250 MPa samples.

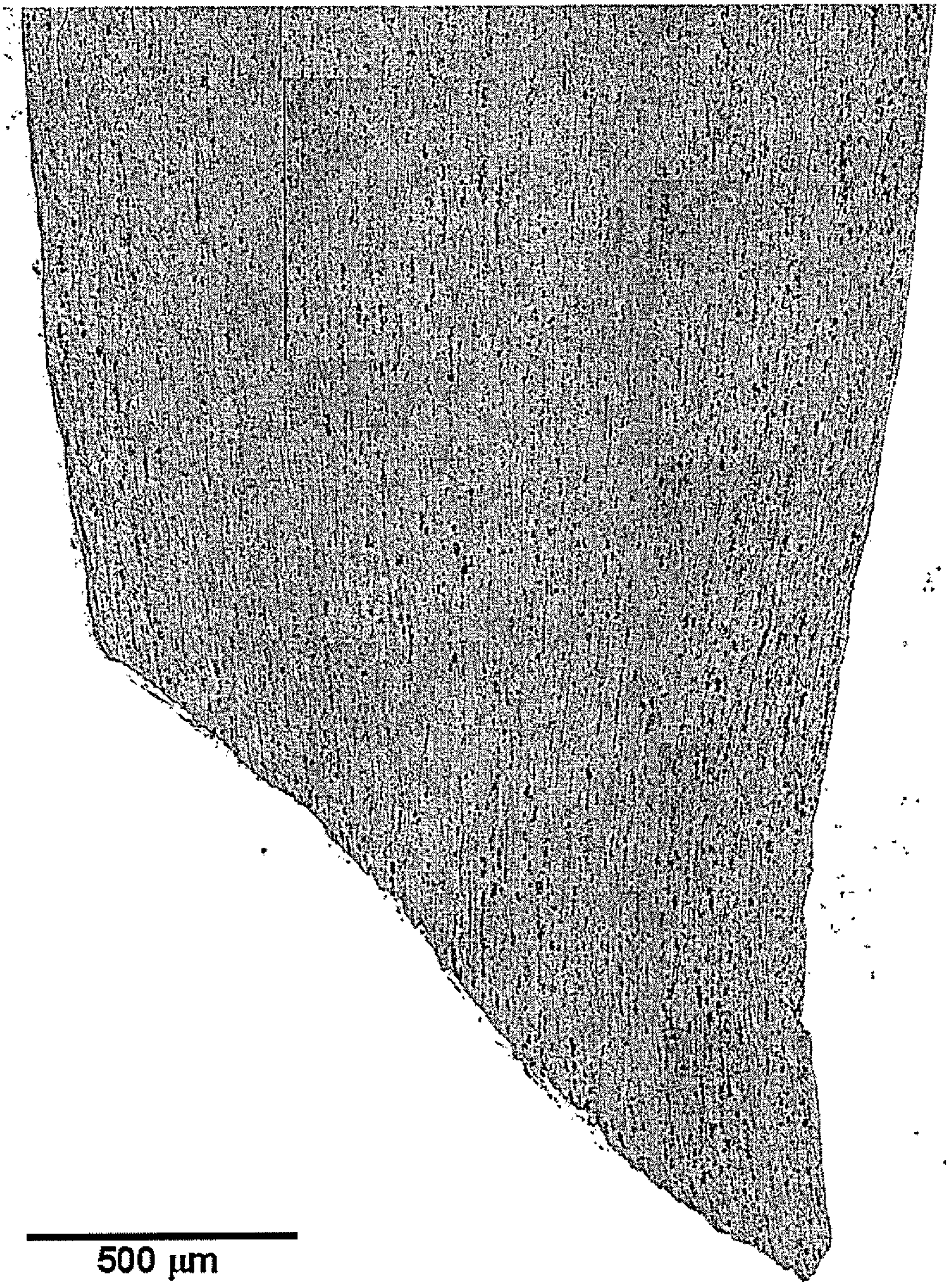

Figure 4.81: High-Fe 6111 T4 sample tested at 0.1 MPa etched and viewed to reveal shearing and slip.

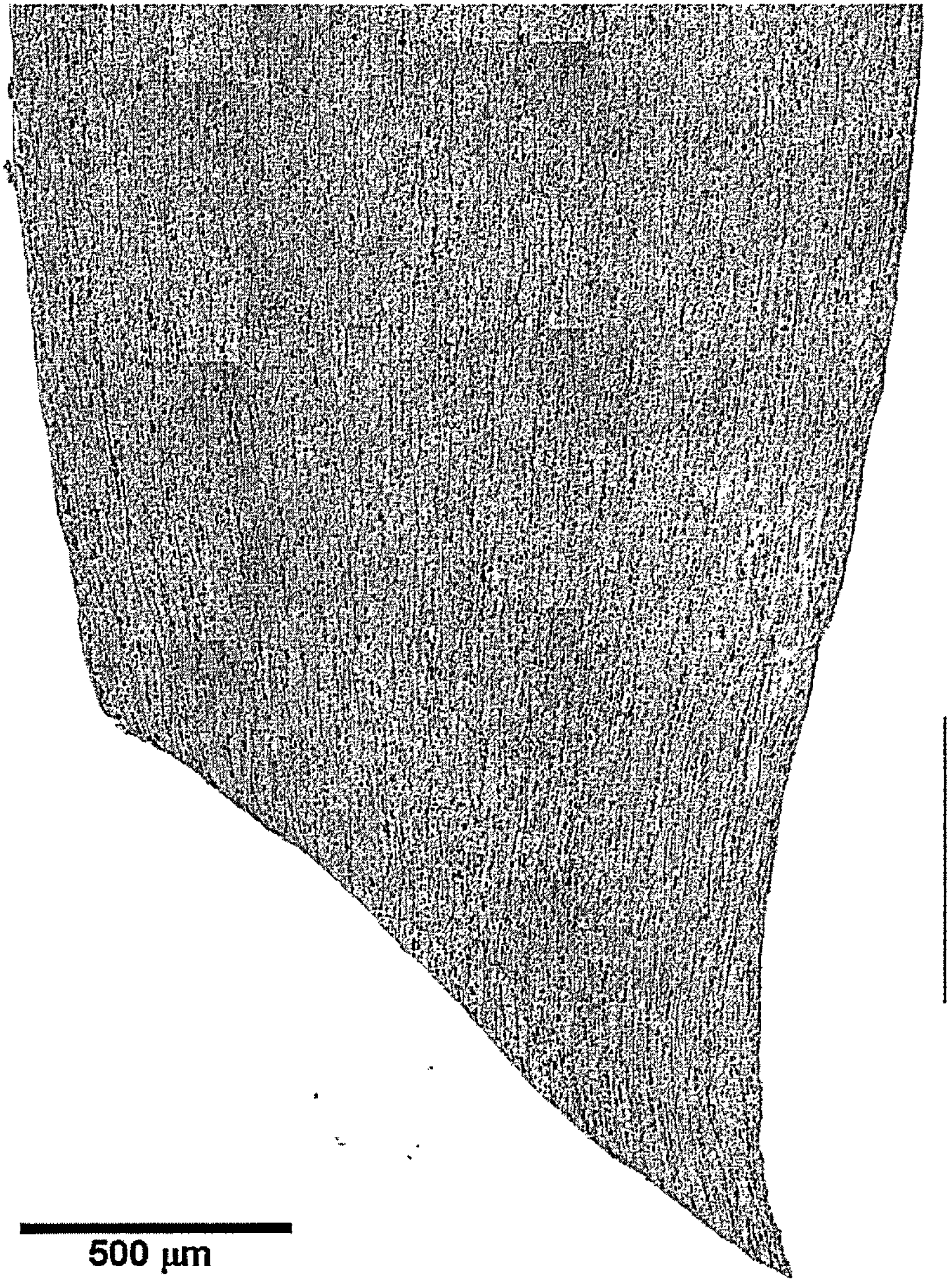

Figure 4.82: High-Fe 6111 T4 sample tested at 125 MPa etched and viewed to reveal shearing and slip.

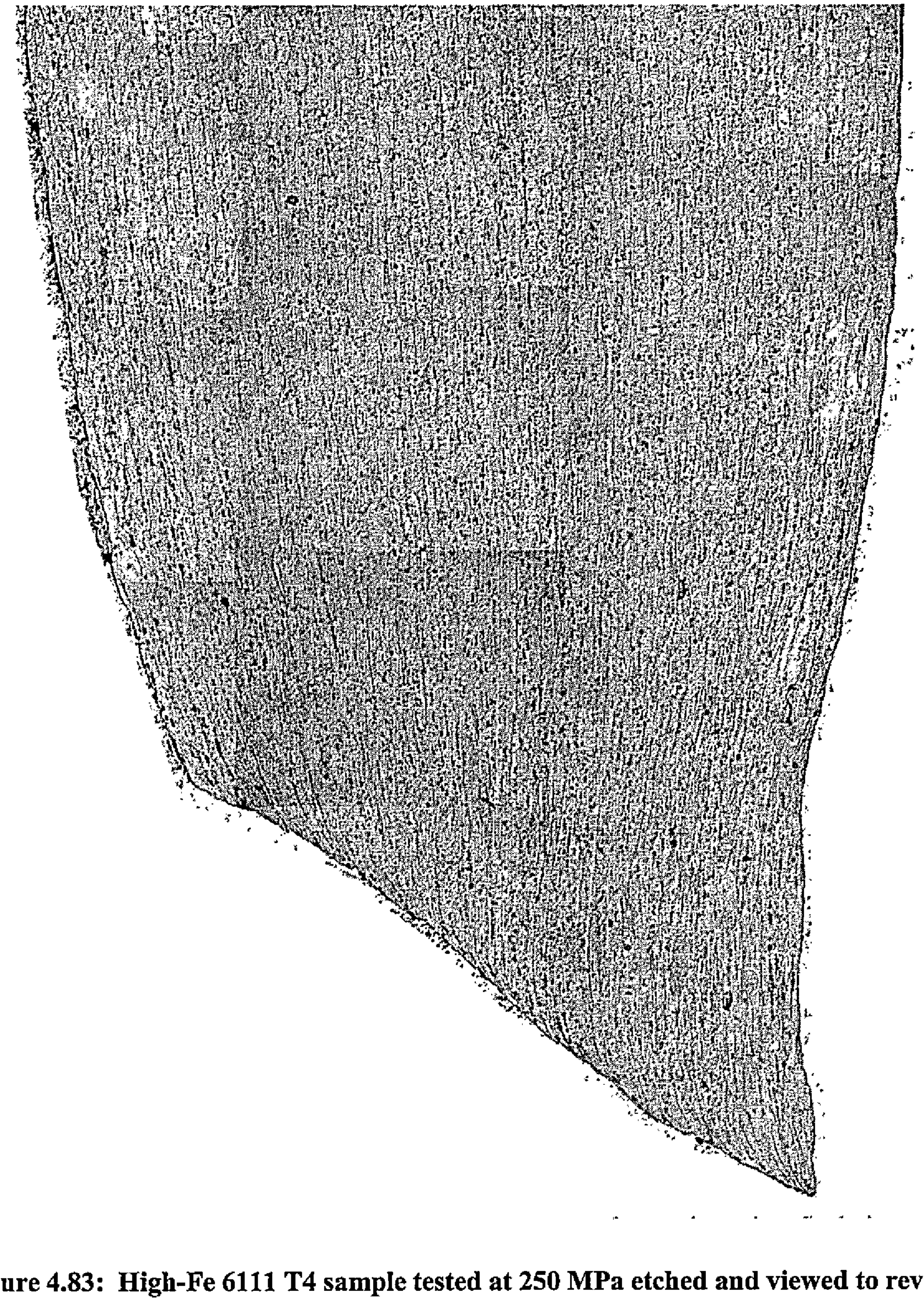

Figure 4.83: High-Fe 6111 T4 sample tested at 250 MPa etched and viewed to reveal shearing and slip.

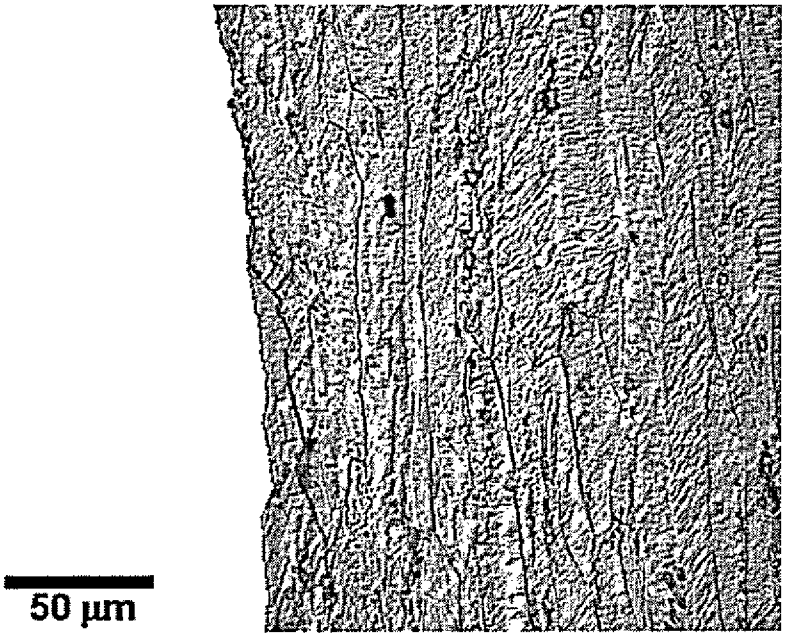

Figure 4.84: High-Fe 6111 T4 sample tested at 125MPa etched and viewed to reveal shearing and slip.

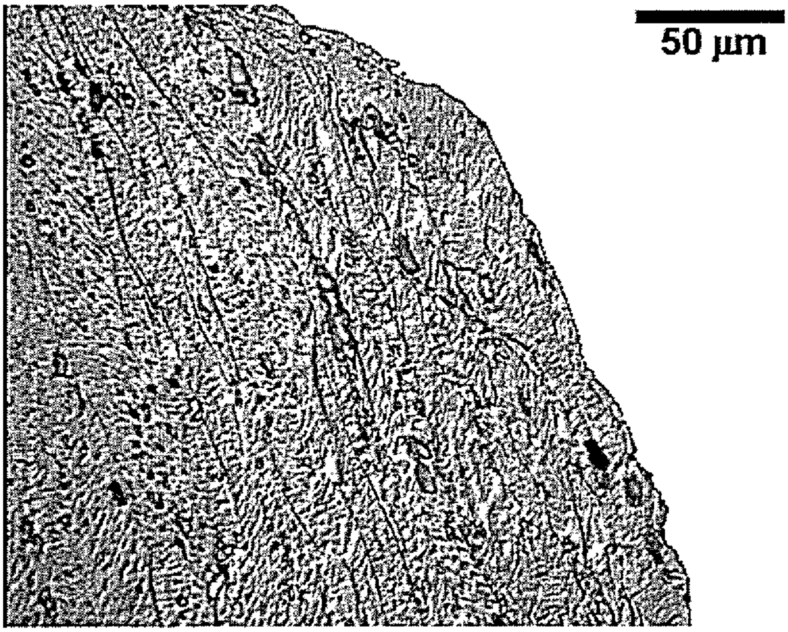

Figure 4.85: High-Fe 6111 T4 sample tested at 250 MPa etched and viewed to reveal shearing and slip.

The intergranular nature of the failure in the low-Fe T6 alloys is made evident by the cracks present on grain boundaries, Figure 4.86 to Figure 4.88. The size and number of these cracks decreases with pressure indicating that intergranular fracture is being suppressed. This is further supported by the steady transition from a fracture surface perpendicular to the tensile axis to one of approximately 50°. Figure 4.89 to Figure 4.90 show higher magnification views of areas near the fracture surface within the necked region, and areas outside the necked region. At low pressures, shearing is limited to the one or two grains nearest the fracture surface, with little grain scale shearing visible back from the necked region. With increasing pressure, the shearing becomes less localized, corresponding to the increased ductility and greater post-necking strains, and can be seen for several grains back from the fracture surface. Grain scale shearing appears to be only slightly higher at this pressure in the uniformly strained region of the sample however, shear in the low-Fe T6 samples at all locations is significantly lower than that seen in the low-Fe T4 samples. No macroscopic shearing was evident at any pressure tested.

Figure 4.86: Low-Fe 6111 T6 sample tested at 0.1 MPa etched and viewed to reveal shearing and slip.

Figure 4.87: Low-Fe 6111 T6 sample tested at 125 MPa etched and viewed to reveal shearing and slip.

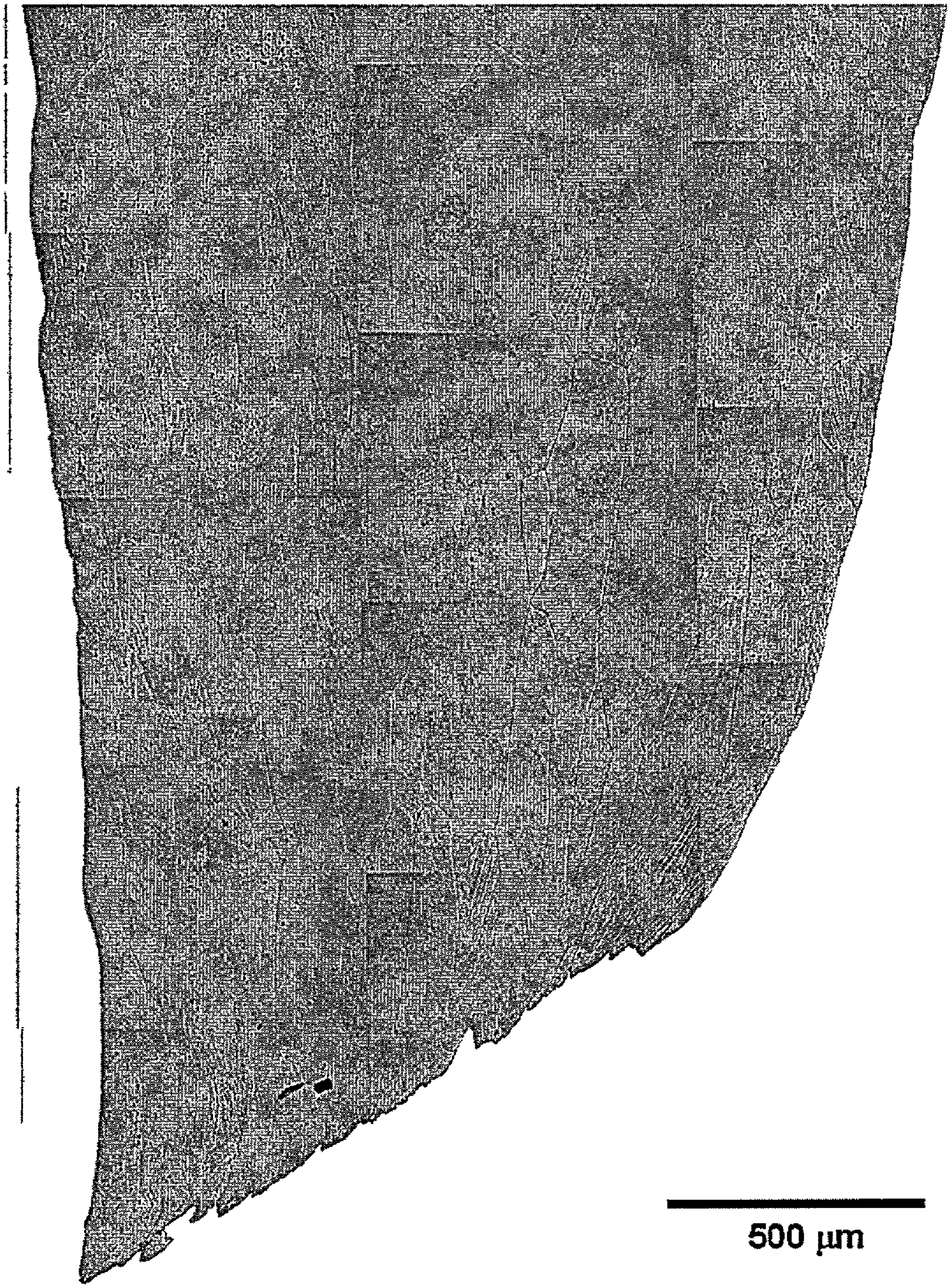

Figure 4.88: Low-Fe 6111 T6 sample tested at 250 MPa etched and viewed to reveal shearing and slip.

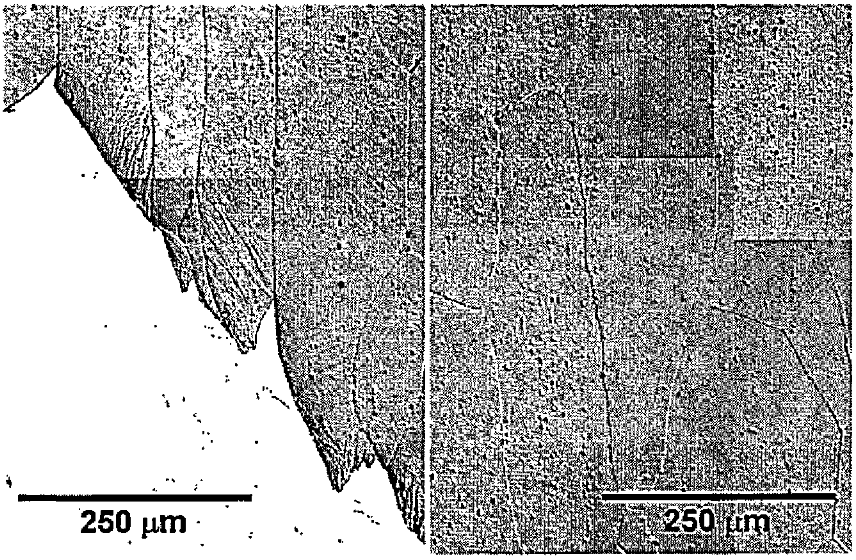

Figure 4.89: Low-Fe 6111 T6 sample tested at 0.1 MPa etched and viewed to reveal shearing and slip. a) adjacent to fracture surface, b) uniformly strained region.

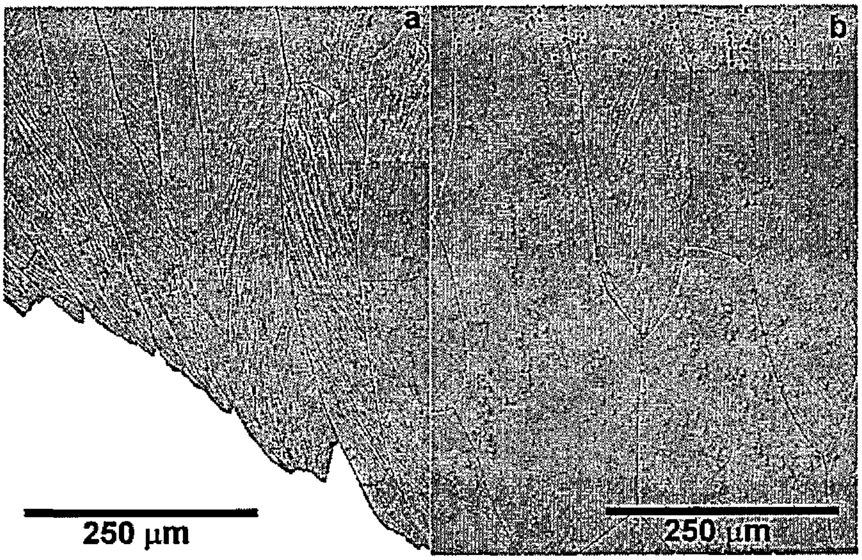

Figure 4.90: Low-Fe 6111 T6 sample tested at 250 MPa etched and viewed to reveal shearing and slip. a) adjacent to fracture surface, b) uniformly strained region.

Figure 4.91 to Figure 4.94 show full composite micrographs of the necked regions of high-Fe T6 samples tested at various pressures. As with the high-Fe T4 samples, it is difficult to resolve shear processes within grains due to the fine grain scale however, the general features can be seen by observing the shearing of grain boundaries. No macroscopic sample-scale shearing is evident in either the 0.1 of 250 MPa samples, However, the formation of a clear shear band is visible in the sample tested at a pressure of 500 MPa, corresponding to a true necking strain of 0.44, a level not reached by any samples tested at lower pressures.

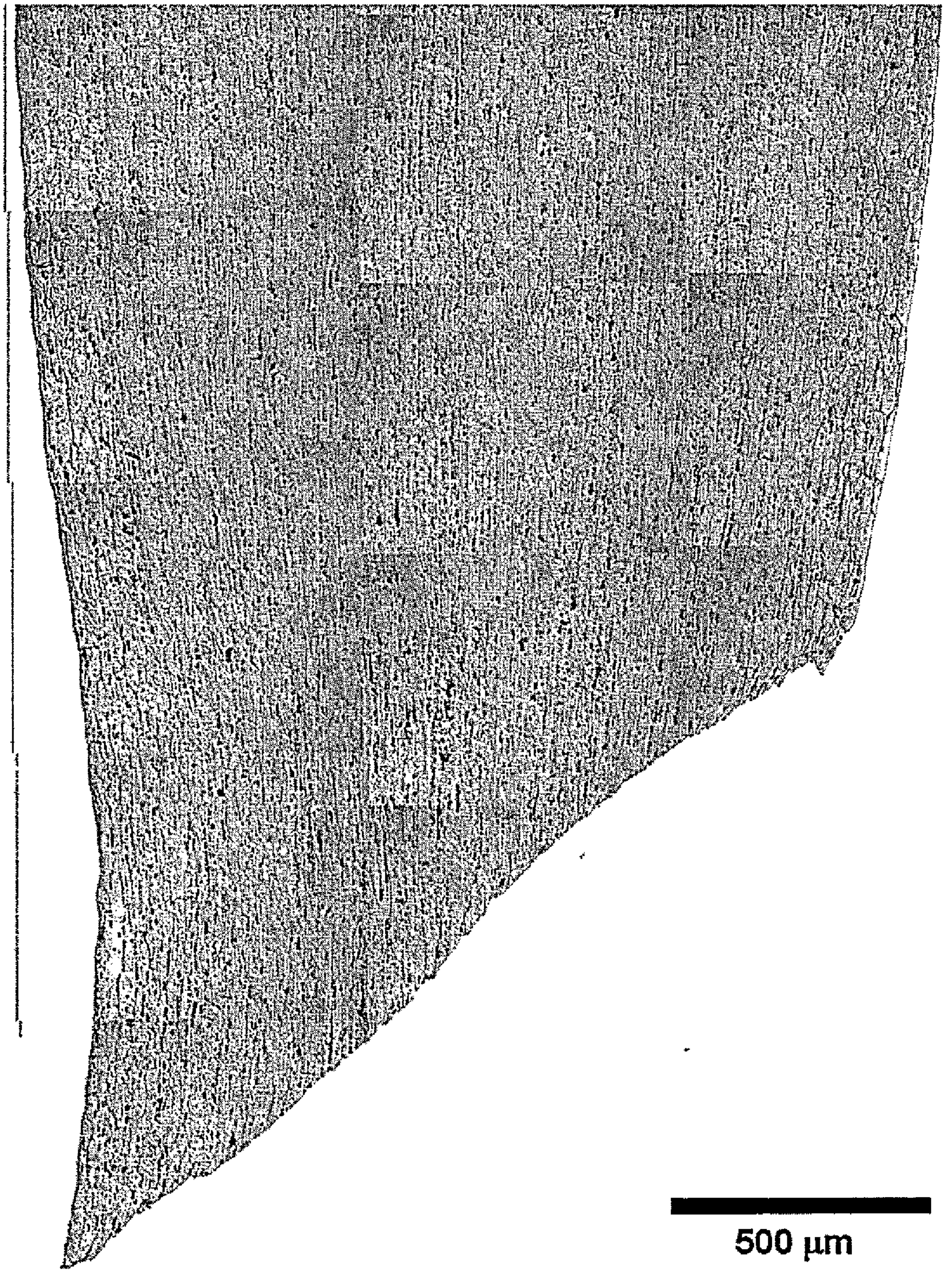

Figure 4.91: High-Fe 6111 T6 sample tested at 0.1 MPa etched and viewed to reveal shearing and slip.

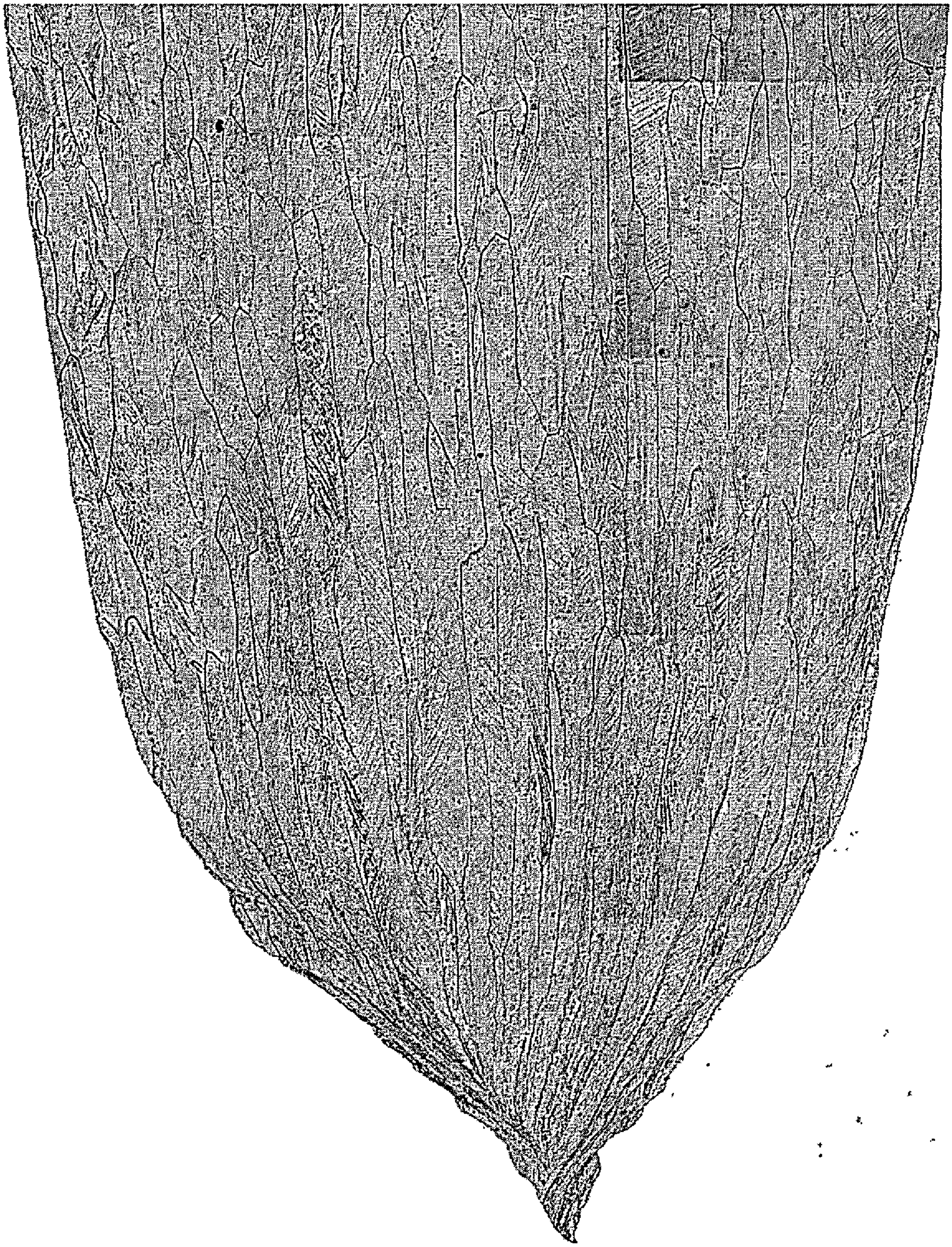

Figure 4.92: High-Fe 6111 T6 sample tested at 125 MPa etched and viewed to reveal shearing and slip.

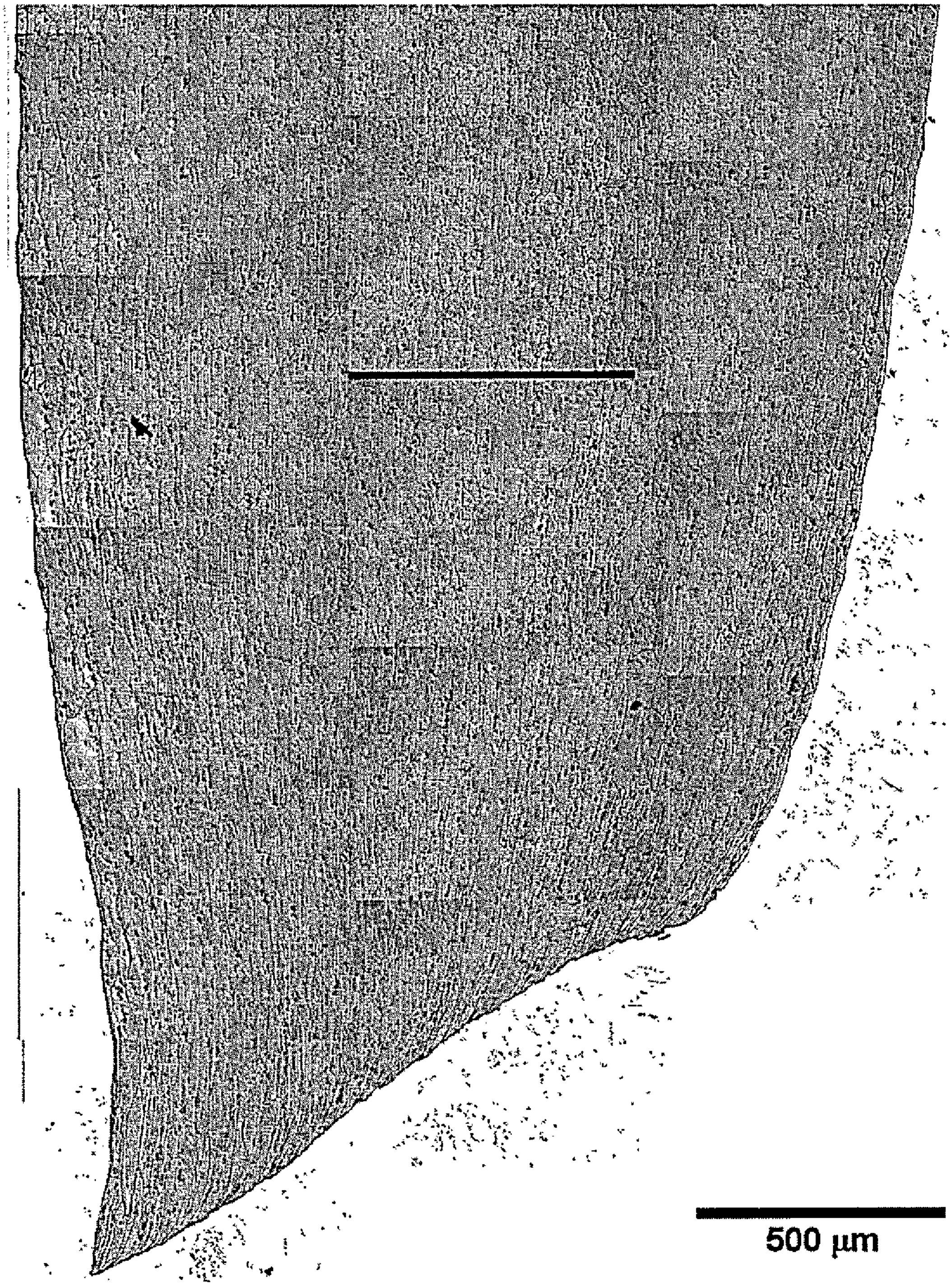

Figure 4.93: High-Fe 6111 T6 sample tested at 250 MPa etched and viewed to reveal shearing and slip.

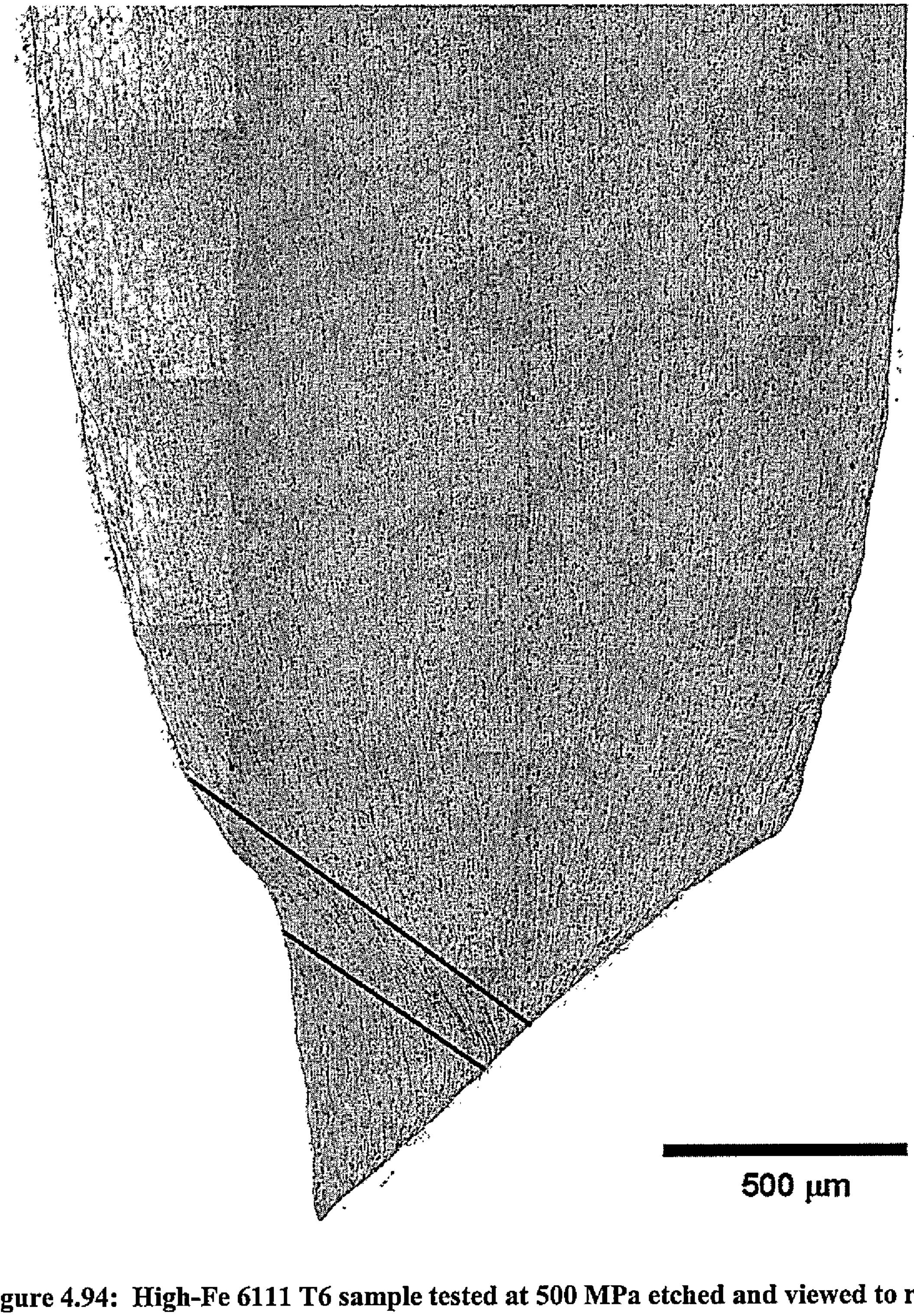

Figure 4.94: High-Fe 6111 T6 sample tested at 500 MPa etched and viewed to reveal shearing and slip. Macroscopic shear band outlined with black lines.

4.3 REVIEW OF OBSERVATIONS

4.3.1 AA 5754 Alloys

It was observed that both iron variants of the 5754 alloys were very sensitive to the application of superimposed hydrostatic pressure, with large increases in post-necking strains occurring. In addition, large increases in uniform elongation were seen when the material was tested at 77 K, along with a corresponding decrease in the amount of grain and large scale shearing. The ductility of the material, as evaluated from reduction in area measurements was seen to be very dependent on both the iron content of the material, and level of superimposed pressure applied during the tensile testing, with a decrease in ductility with increasing iron contents, and conversely, an increase in ductility with increasing superimposed pressure. In addition the Fe content was shown to cause a change in fracture mode with the low-Fe alloy failing by a double cup and cone mode, and the high-Fe alloy failing by shear MVC. Pressure was shown to severely restrict the growth of damage, however it did not appear to appreciably effect the formation of shear bands within the material.

4.3.2 AA 6111 Alloys

In the T4 temper, increasing iron content was shown to cause a decrease in both uniform elongation and reduction in area. Both the low and the high-Fe alloys were observed to fail by the shear MVC mode, and the only change in fracture mode occurred when the low-Fe alloy was tested at 500 MPa, where it failed by ductile rupture. As with the 5754 alloys, the application of superimposed pressure was shown to severely retard the growth of damage.

A significant change in fracture mode was observed for changing iron contents in the T6 alloys, where the low-Fe alloy fails intergranularly, and the high-Fe alloy fails by a shear MVC process. No change in fracture mode with increasing pressure was observed for the high-Fe samples when tested with superimposed pressure, however the low-Fe samples showed a transition from intergranular fracture to shear MVC failure with increasing superimposed pressures. Both iron variants demonstrated an increase in reduction in area with increasing superimposed pressure and a corresponding decrease in the measurable damage.

5 DISCUSSION

5.1 FLOW BEHAVIOUR FOR AA 5754 ALLOYS UNDER UNIAXIAL TENSION AT AMBIENT PRESSURE

When examining the flow behaviour of the 5754 alloys in uniaxial tension, it is useful to consider the pertinent variables, which influence the material response. The major difference distinguishing the alloys tested in this study is the four-fold increase in iron content between the low-Fe variant relative to the high-Fe variant. This increase in Fe content has two major impacts. Firstly, there is an increase in the density of iron-based intermetallic inclusions, clearly seen in SEM images of polished samples for both alloys, Figure 4.17 and Figure 4.20. Secondly, the presence of these intermetallics, which are formed in the melt, act both as grain refiners and pinning sites causing a decrease in the grain size by a factor of 2, from 48 μm to 24 μm with increasing iron content.

When tested at ambient pressure and temperature, the low-Fe variant fails in a cup and cone mode. The fracture surface is characterized by a cone with voiding present at the centre, and relatively featureless shear lips running up the sides, Figure 4.5. An examination of this image, etched to reveal shear banding, shows heavy shearing of the region associated with the shear lips, indicative of a system of conjugate shear bands being formed prior to failure, Figure 4.23. Due to the low-Fe content, the material is allowed to deform to the point at which a central void is formed at the intersection of the conjugate shear bands, corresponding to a region of severe deformation and high hydrostatic tension associated with necking. Once this central void is formed, conjugate shearing of the sample continues within the two remaining ligaments and the sample effectively necks down to two knife edges. While some damage is measurable within the shear bands, it appears that the amount is insufficient to cause local softening of any single shear system, which would result in the localized shear MVC failure seen in the high-Fe variant.

The high-Fe material shows considerably different fracture behaviour due to damage initiation at the iron intermetallics during the growth of shear bands in the sample. As can be seen in the image of the high-Fe alloys which has been etched to reveal shear bands, Figure 4.25, a set of conjugate shear systems has developed within the sample neck, similar to that seen in the low-Fe alloy. However as reported by Spencer (2000), the shearing within the neck does not appear symmetric as is seen in the low-Fe alloys, indicating softening events are occurring which result in localization onto one shear band. Damage was shown to first nucleate in the centre of the sample along the most active shear band, due to the combination of shearing and the hydrostatic tension associated with the neck. As the iron intermetallic content is high, the interparticle spacing is proportionally low. Thus, with the localized shearing, very little normal strain is required to cause void linkage within the active shear band, and the resultant failure occurs by shear MVC. It should be noted that the results clearly indicate that very little damage is required to trigger the final failure as indicated by the very low level of measurable damage observed in the samples.

Lloyd et al. (1997) have reported a significant Hall-Petch effect for this alloy, corresponding to an approximately 15% decrease in yield strength for an increase in grain size by a factor of 2. No such effect was seen in the present work however, with no significant change in the measured yield or ultimate tensile strength. While it was not determined why this was not observed in this study, it may be the result of the effects of texturing with straining offsetting the grain size differences.

Examination of the samples tested at ambient pressure, but at 77K show a large increase in the uniform elongation for both iron contents samples in comparison to those tested at ambient temperature. The reduction in area of the low-Fe alloy sample was shown to decrease by about 10% at 77K. However, it stayed about the same for the high-Fe sample. Of primary interest is the overall decrease in the PLC effect for most of the strain history of both samples. At 77K, the low temperature serves to slow the diffusion of the Mg in the alloy, which suppresses the PLC effect and hence removes the negative strain rate sensitivity exhibited by the samples. This, along with the marked increase in work hardening rate at 77 K allows the samples to continue to strain to much greater uniform elongations, without shear localization that would cause unstable flow and fracture of the sample. As the samples continue to strain, measurements show that damage continues to form, at higher levels than that seen for samples tested at ambient temperature, particularly for the high-Fe alloys. It would appear then that at a critical combination of damage and flow stress, flow localizes to the plane of maximum shear and the sample fails by catastrophic coalescence of voids. The transition of the low-Fe alloy from a double cup and cone failure to one of shear MVC, can be simply explained as a result of the elimination of the intense shear necessary to form the initial central void. As there is a lower iron intermetallic content in the low-Fe alloy, the greater reduction in area comes as expected, due to the higher strain required to cause void coalescence, in comparison to the high-Fe alloy. This argument is further supported by the distinct lack of shear bands visible in the images etched to reveal shear bands with only minor grain shearing evident, mostly localized near the fracture surface, Figure 4.24 and Figure 4.26. The suppression of the PLC effect and corresponding increases in uniform elongation have been reported for Al-Mg-Zn by Chung et al (1977). In their work, shear localization of samples tested at room temperature was observed, corresponding to a negative strain rate sensitivity. When tested at 77K, the PLC effect was completely eliminated, as was the propensity of the material to fail by localized shear.

5.2 THE EFFECT OF PRESSURE ON THE FRACTURE BEHAVIOUR OF AA 5754 ALLOYS

Changes in superimposed hydrostatic pressures for the 5754 samples, while not producing drastic changes in the sequence of damage and fracture, do provide useful verification to the arguments presented for the ambient pressure tests.

The general trend observed for both the low and the high-Fe samples was a greater reduction in area for increasing applied pressure. As has been reported elsewhere (J.J. Lewandowski, et al., 1998; French et al., 1975; Liu et al, 1993; Brownrigg et al, 1993), the application of superimposed pressure has the effect of reducing or eliminating damage by reducing of even reversing the hydrostatic tensions generated within the neck of a sample undergoing tensile deformation. Damage measurements indicate that in fact consistent reductions in damage are shown for all samples with increasing superimposed pressure.

In considering the low-Fe samples, the superimposed pressures effect on the fracture behaviour should be isolated to only the damage processes, as it has been shown in both this work and others, (Lewandowski, et al, 1998), that pressure has little to no effect on pre-necking behaviour. The sequence of events leading to failure of the low-Fe sample are then as follows. The sample yields and begins to deform similarly to the sample tested at ambient pressure. Necking occurs in the sample along with the formation of a conjugate shear system as seen in Figure 4.23. The generation of damage within the sample is suppressed due to the presence of the superimposed pressure, which delays the formation of the central void to greater strains, allowing for the increased reduction in area observed for the sample tested at 125 MPa. With continued straining, the intense shear in combination with an increasing hydrostatic tension, a result of the more severe post-necking deformation, becomes sufficient to allow voids to form and nucleate the central cavity. Shearing then continues within the remaining ligaments until the sample fails. The result is a similar fracture process to that at ambient pressure however, with more severe deformation due to the delay of the central void formation.

A similar situation occurs for the high-Fe sample. It was shown that it is the presence of the damage within a shear band that cause the final localization of strain to one shear band leading to shear MVC failure. When tested under superimposed pressure, damage is suppressed, as confirmed by the damage measurements, allowing for more extensive shearing of the sample before catastrophic failure occurs, as can be clearly seen in Figure 4.27 and Figure 4.28. At sufficiently high pressures, the damage process is completely suppressed, and the material simply fails via a process of conjugate shearing down to a knife-edge, again indicating it is the nucleation and growth of the damage that leads to the catastrophic shear MVC failure of this alloy.

Figure 5.1 and Figure 5.3 show fracture maps illustrating the progression of the fracture process for both the low and high-Fe alloys under all conditions tested. The figures were constructed as follows. When available (i.e. when sample did not neck to 100% RA), a final load value and reduction in area was taken and from these a final true stress and strain was calculated and plotted on the original true stress-strain curve. An assumption of linear work hardening after the initiation of necking was made, and a linear extrapolation was made through the plotted true stress-strain values. Although the assumption of linear work hardening was approximate, the results show it provided a reasonable fit. Examination of the curves shows that the linear extrapolation has a slightly lower slope than the end of the actual stress strain curve. This is a result of ignoring the hydrostatic tension generated within the neck of the sample, which would raise the calculated failure stress.

In the event that no final load or RA measurements could be made (i.e. sample necked down to 100% RA), hardness measurements were made and compared to those of a sample which did not neck down to 100% RA. The stress was calculated from the ratio of these hardnesses giving a failure load for the 100% RA sample. The failure strain was then back calculated from a linear fit of available final stress and strain points. While this is not an ideal procedure, the results show a reasonable fit.

Several regions are plotted on these figures including the various strains at which damage, macroscopic shear bands, and a central void forms. The strain was calculated assuming a state of plane strain. Then the area at which the feature occurs is just the original sample width multiplied by the measured thickness at initiation of the particular feature. From this, the true strain was calculated. In many cases, it was very difficult to distinguish the initiation of damage. In these cases it was assumed that damage was formed sometime after the formation of macroscopic shear bands.

From Figure 5.1, the differences in strain hardening exponents between ambient and low temperatures are evident for the low-Fe samples. It can be seen that the pressure has little effect on the shear behaviour of the material, where the strain required to form macroscopic shear bands appears as the grey line. The major effect appears in the shifting of the strain required for formation of the central void by a true strain of approximately 0.5, a result of the suppression of damage processes within the material. The increase in strain of 0.5, corresponds to an increase in stress of 95 MPa, reasonably close to the superimposed pressure, showing that the damage process has a fairly direct relationship with pressure.

In Figure 5.2, the results for the high-Fe alloy are shown. As with the low-Fe alloy, the difference in strain hardening exponents between the ambient and 77 K samples are clearly evident. Large increases in ductility are evident with increasing pressures up to a 100% RA. The associated stress increase for the sample tested at 0.1 MPa to that tested at 250, and 500 MPa is approximately 240 MPa, and 190 MPa and respectively. Considering the previous linear relationship of pressure to damage processes seen in the low-Fe alloys, it is apparent that the high-Fe samples will fail at 100% RA at pressures lower that 250 MPa.

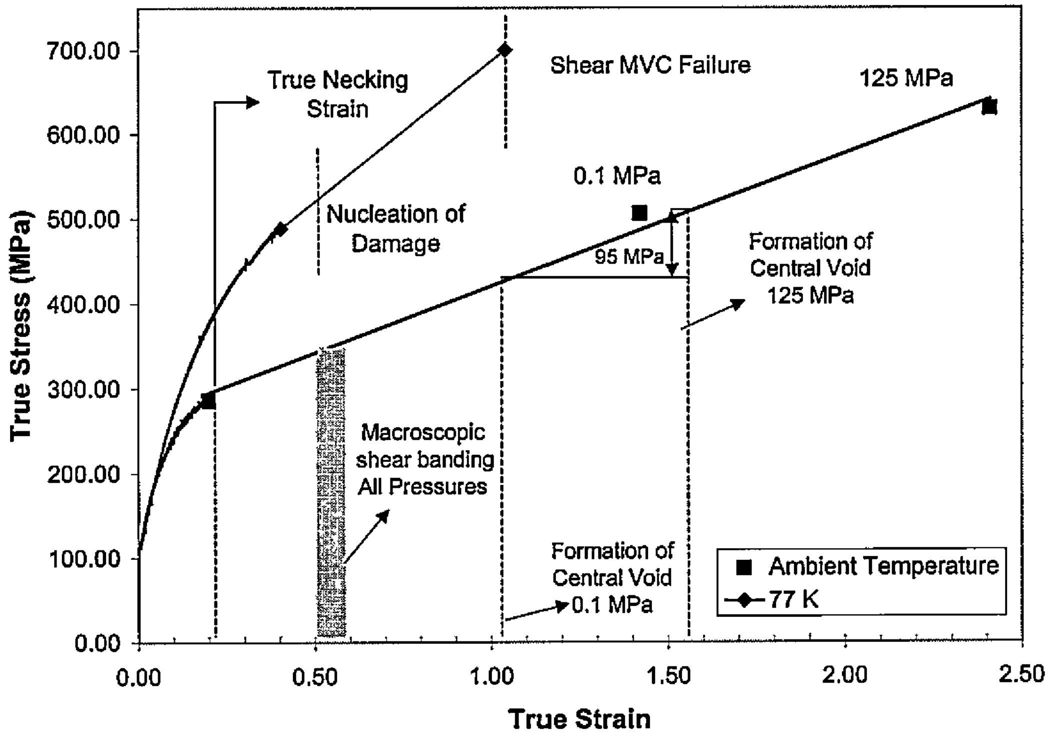

Figure 5.1: Fracture map for the low-Fe 5754 alloy.

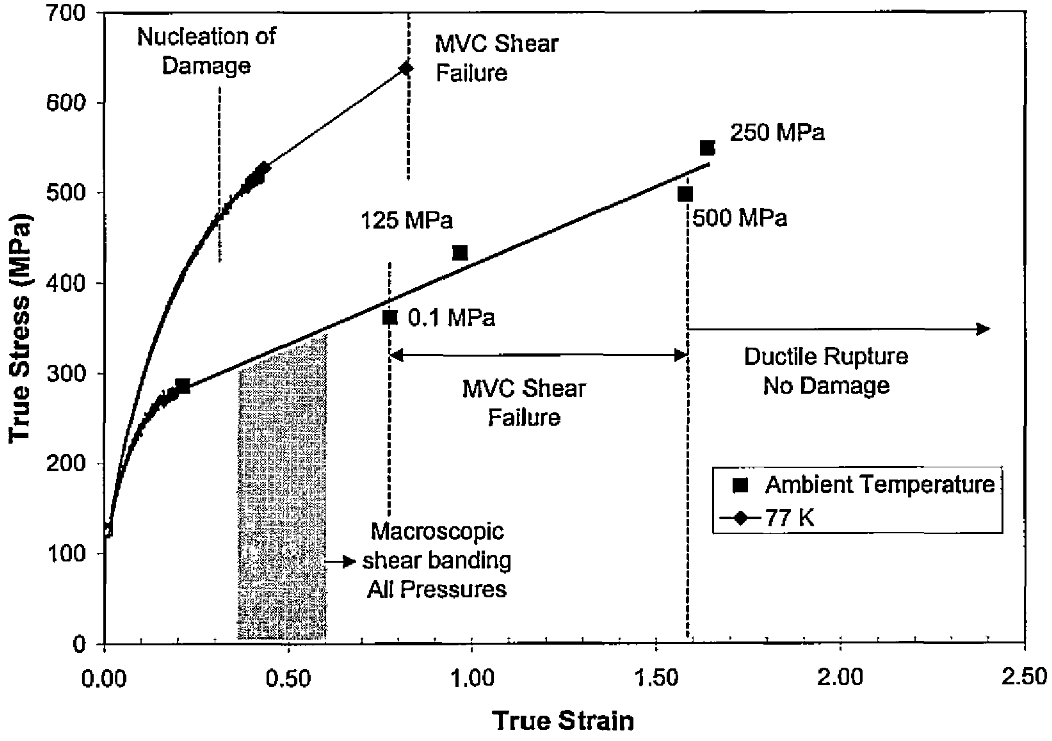

Figure 5.2: Fracture map for the high-Fe 5754 alloy.

The two extrapolated stress-strain curves for the low and high-Fe samples tested at ambient temperature are shown together in Figure 5.3. Here it can be seen that the strain required for initiation of macroscopic shear are similar for both alloys, and pressure had little effect on the either the shearing or the macroscopic deformation, confirming previous arguments. The plots are almost identical, indicating that the iron content does not affect the overall flow behaviour of these alloys. The influence of iron level occurs only on the mechanism of initiating the final catastrophic failure, either as a result of the formation of the central void in the low-Fe alloy, or the rapid coalescence of damage within shear bands for the high-Fe alloy.

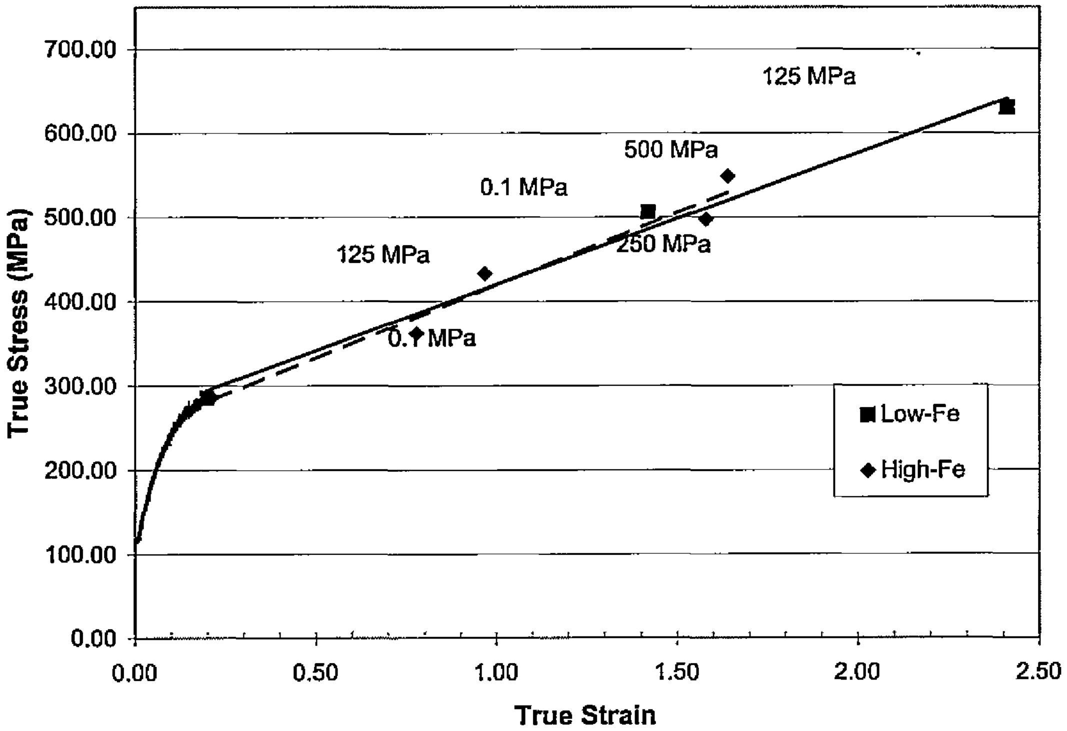

Figure 5.3: Extrapolated stress-strain curves for the low and high-Fe 5754 alloys tested at ambient temperature.

5.3 WORK HARDENING BEHAVIOUR FOR AA 5754 ALLOYS

Figure 5.4 shows plots of the $(d\sigma/d\varepsilon)/\mu$ versus $(\sigma- \sigma_y)/\mu$ for both the low and high-Fe alloys tested at 77 K and 298 K in addition to data for pure aluminum, where μ is the temperature corrected modulus. Figure 5.3 showed that there appeared to be little discernable difference in the flow behaviour due to the different iron contents, and corresponding grain size difference. However, Figure 5.4 shows a small change in the work hardening behaviour due to the finer grain size. This could be a result of the increased iron intermetallic constituents acting to tie up Mg, though this was not confirmed. The important contribution to the work hardening rate due to the presence of the Mg in solution is clearly visible for both iron contents tested at 298 K, with the intrinsic work hardening of the 5754 alloy being significantly higher than the pure aluminum. Lastly the work hardening behaviour of the 5754 alloys tested at 77 K is shown, where the increased work hardening rate is due to the suppression of the PLC effect, resulting in much higher achievable stresses and strains. The sensitivity of the work hardening rate to grain size differences appears to be slightly greater at lower temperatures.

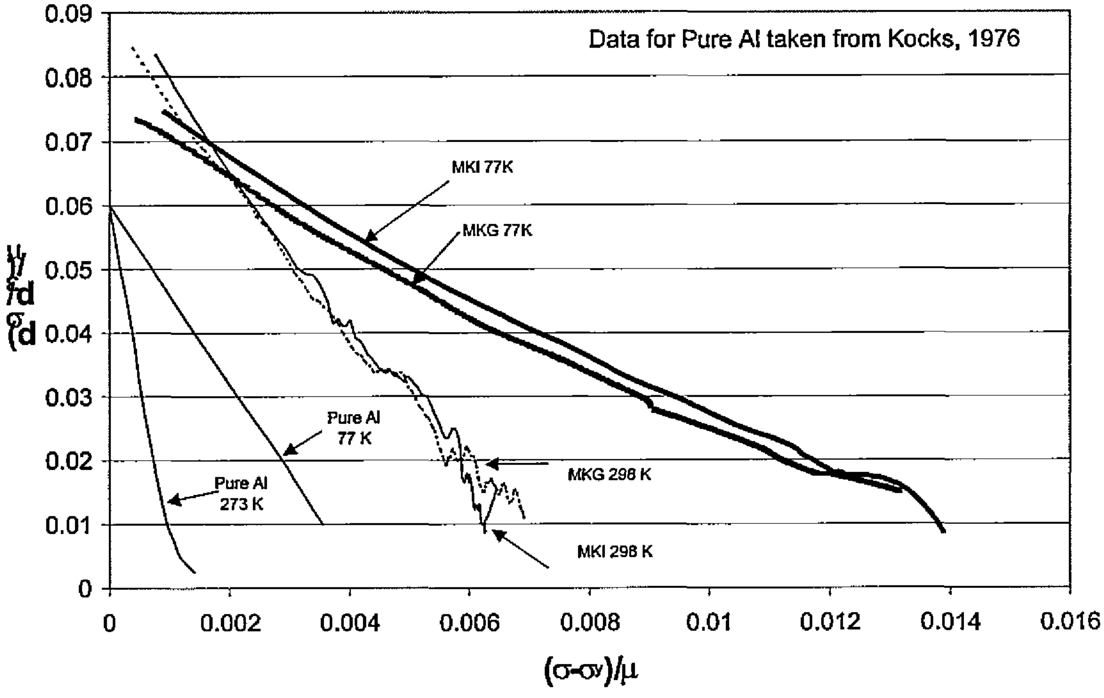

Figure 5.4: Plot showing the work hardening behaviour for pure Al and both 5754 alloys at 77 K and 298 K.

5.4 FLOW BEHAVIOUR FOR AA 6111 ALLOYS UNDER UNIAXIAL TENSION AT AMBIENT PRESSURE

5.4.1 T4 Temper

The results of the fractography and metallography showed no change in fracture behaviour with increasing iron contents with both materials failing by the shear MVC fracture mode. However, a significant reduction in uniform strain for the high-Fe sample over the low-Fe sample, 0.22 to 0.27 respectively, was observed indicating that the higher iron content is detrimental to the overall ductility. Confirming these results, the reduction in area measurements for the high-Fe are proportionally lower than for the low-Fe sample.

The overall fracture behaviour of the alloys can be described as follows. At ambient pressures, both materials exhibit significant amounts of grain scale slip steps. However, the slip never coalesces into macroscopic shear bands. As shown in Figure 4.58 and Figure 4.59, damage rapidly accumulates within the neck of the sample with continued straining. At a critical amount of damage, approximately 1.1 % and 0.85 % area fraction for the high and low-Fe alloys respectively, voids coalesce to form the observed shear MVC failure. As the high-Fe variant has a lower interparticle spacing, the void linkage process requires proportionally less strain than that required for the low-Fe alloy. In this regard it is useful to recall the model put forward by McClintock (1967) for the localization of flow into shear bands due to the presence of voids. In his work, the simplified condition for instability is given as:

$$\left(1-\frac{\pi ab}{\mathrm{lalb}}\sqrt{\frac{2}{(1+{}^{a^2}\!/_{b^2})}}\right)\Bigg/\left(1-\frac{4}{3}\pi\frac{a}{l_b}\left(\frac{b}{l_b}\right)^2\right)<\frac{\sqrt{3}}{2} \qquad \text{Eqn. 5.1}$$

where a and b are the major and minor void axes, and l_a and l_b are the interparticle spacing perpendicular and parallel to the tensile axis respectively. It is clear that the increase in iron content and the associated increase in particle size observed in addition to a reduction in the interparticle spacing will result in the satisfaction of this criterion at an earlier stage. Hence, the high-Fe material is predicted to localize to shear at lower strains than the low-Fe variant, as is observed.

5.4.2 T6 Temper

The data presented in the results section show a large variation in fracture behaviour in the T6 alloys for the two different iron contents studied. In order to understand this, it is important to consider the primary effects of iron on the material microstructure. With increasing iron content, two consequences of major importance occur. Firstly the iron-aluminide intermetallic content increases accordingly, and secondly, similar to that seen with the 5754 alloys, these intermetallics exhibit a strong grain refining effect, resulting in an observed decrease in grain size of a factor of ~3, from 122 μm to 41 μm for increasing iron content. It is this difference in grain size, which is believed to cause the change in fracture mode from intergranular fracture to shear MVC for the low and high-Fe samples respectively.

The change can be understood by examining the work of Evensen et al. (1975). In their study, the competition between continued plasticity and intergranular fracture in an Al-Mg-Si alloy was examined, with a focus on the role grain size plays. They showed that the intergranular fracture stress was a linear function of the inverse root of the grain size ($d^{-1/2}$). A model was proposed which attempts to define a critical intergranular fracture condition based on the intrinsic resistance to slip σ_o, the width of slip bands W, the grain size L and the critical stress required to initiate grain boundary fracture σ_{crit}:

$$\sigma_{app} > \sigma_o + \left(\frac{1}{L^{1/2}}\right)\left(\sigma_{crit} W^{1/2}\right) \qquad \text{Eqn. 5.2}$$

The model then predicts an inverse square root dependence on the grain size. Applying this model to the materials studied in this work, several assumptions can be made. First, the intrinsic resistance to slip of the low and high-Fe samples can be assumed to be similar, as the slip in this model is considered to occur on the grain scale and this process is primarily affected by the presence of age hardening particles. Since both materials have received identical age hardening heat treatments, the intrinsic resistance can be assumed to be equivalent. By a similar argument, the width of the slip bands will likely be similar, as the Fe content has been shown to have little effect on the shearing behaviour, (Spencer, 2000), and will be assumed as such. Lastly, as there is no evidence of preferential grain boundary segregation of iron based intermetallics which could cause grain boundary embrittlement, thus there is no apparent reason to believe that the critical stress required to nucleate a crack would be different for either material. This then simplifies the model to the applied stress required for intergranular fracture being proportional to the inverse square root of the grain size:

$$\sigma_{app} \approx \left(\frac{1}{L^{1/2}} \right) \qquad \text{Eqn. 5.3}$$

Considering the grain size difference between the low and the high-Fe variants, 141 μm and 41 μm respectively, the applied stress required to cause intergranular fracture will be approximately twice that for the high-Fe alloy over the low-Fe indicating intergranular failure becomes more difficult at smaller grain sizes. This will be discussed further with the presentation of a fracture map based on fracture stress as a function of pressure, and grain size.

5.5 THE EFFECT OF PRESSURE ON THE FRACTURE BEHAVIOUR OF 6111 ALLOYS

5.5.1 T4 Temper

Changes in superimposed pressure, resulted in a steady increase in ductility for both the low and high-Fe samples. Additionally, at higher pressures, deformation was sufficient within the low-Fe alloys to allow coordination of slip into macroscopic, sample scale shear bands.

The changes in ductility can be understood using a similar argument as to that proposed for the 5754 alloys. It is apparent from the extensive voiding observed on the fracture surfaces, Figure 4.39 and Figure 4.40, that damage plays a key role in initiating final sample failure. With increasing superimposed pressures, the amount of damage consistently decreases to almost immeasurable amounts at sufficiently high pressures.

This decrease in damage is also seen as a decrease in the void size on the fracture surfaces for both the low and high-Fe T4 alloys with increasing applied pressure.

Considering again the model of McClintock (1967) for the localization of flow to shear, it is noted that the criterion depends not only on the void spacing, l_a and l_b, but also on the void size, a and b. Under superimposed pressure, the growth of the voids will be slowed or eliminated altogether reducing the values of a and b for any given strain with respect to a sample tested at a low pressure. The result of this then, is a delayed onset of shear MVC failure, allowing for greater post necking strains and the associated increase in RA observed.

Figure 5.5 shows the stress-strain data for both iron contents that have been extrapolated as described in section 5.2. The curves can be effectively superimposed, with the only significant difference being the larger strains achieved by the low-Fe alloy. Similar to that seen in the 5754 alloy, the difference in the iron content between the two materials does not appear to substantially alter the flow behaviour of the T4 materials. Rather, it is seen that it only effects the final catastrophic failure process.

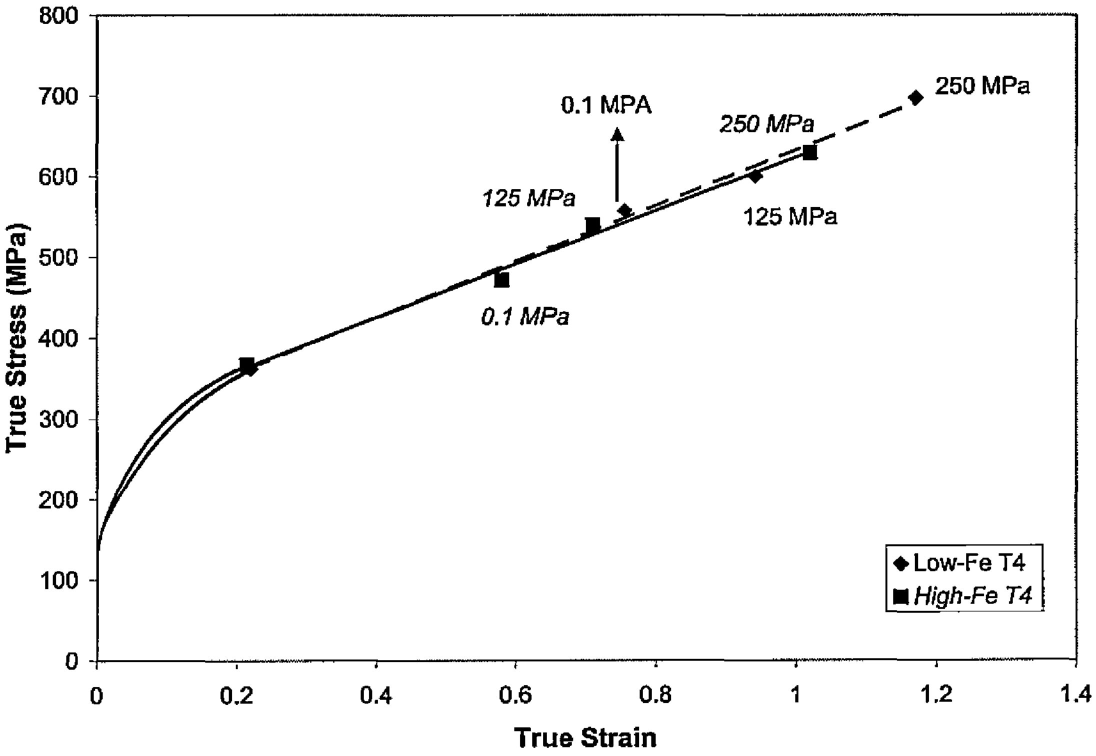

Figure 5.5: Extrapolated stress-strain curves for the low and high-Fe 6111 T4 alloys.

5.5.2 T6 Temper

Pressure was shown to have the most significant effect on the low-Fe alloy in the T6 condition, where a transition from intergranular fracture to shear MVC was observed with increasing imposed hydrostatic pressures. In order to understand this change it is useful to first identify the critical step in the intergranular fracture process, this being either the nucleation or the propagation of the crack. Examination of the polished section for the low-Fe T6 sample tested at 0.1 MPa, shows the presence of cracks below the fracture surface. Since the conditions for crack propagation are met upon nucleation of a crack for nucleation controlled failure, were the failure critically dependent on the nucleation of the crack, these internal cracks would not be present. Therefore it must be that the propagation of the crack is the critical step, which controls the failure process. It has been proposed that for propagation-controlled brittle fracture, the condition required for crack propagation is the attainment of a critical constant maximum principle stress, (Lewandowski et al, 1998). For this mechanism, the fracture condition can be described by:

$$\bar{\sigma} = \sigma_f + P \qquad \text{Eqn. 5.4}$$

where $\bar{\sigma}$ is the effective stress, σ_f is the brittle fracture stress in tension, and P is the superimposed pressure. This implies a linear relationship between the effective stress required for fracture and the applied pressure. Figure 5.6 shows the extrapolated stress-strain curve for the low-Fe 6111 T6 alloy. The intergranular fracture condition for the three superimposed pressures are represented by the three horizontal lines, which intersect the y-axis. The lowest line is drawn at a stress of 451 MPa, corresponding to the fracture strength of the sample tested at 0.1 MPa which failed intergranularly. The other lines are then drawn at stresses of 125 MPa and 250 MPa higher respectively, representing the linear relationship proposed in Eqn. 5.4. For a sample to fail by intergranular failure then, its fracture stress must meet or exceed the intergranular fracture condition plotted. At 0.1 MPa, it of course meets the intergranular fracture condition, as this is the reference point. The fracture stress for the sample tested at 125 MPa falls below the intergranular condition indicating it should have failed predominantly by shear. It is noted however, that the actual fracture process was a combination of both intergranular and shearing. This implies that at these stresses both modes are operating competitively. The sample tested at 250 MPa failed predominantly by shear, though exhibiting some limited intergranular fracture. As this data point falls below the critical intergranular failure condition this is as expected.

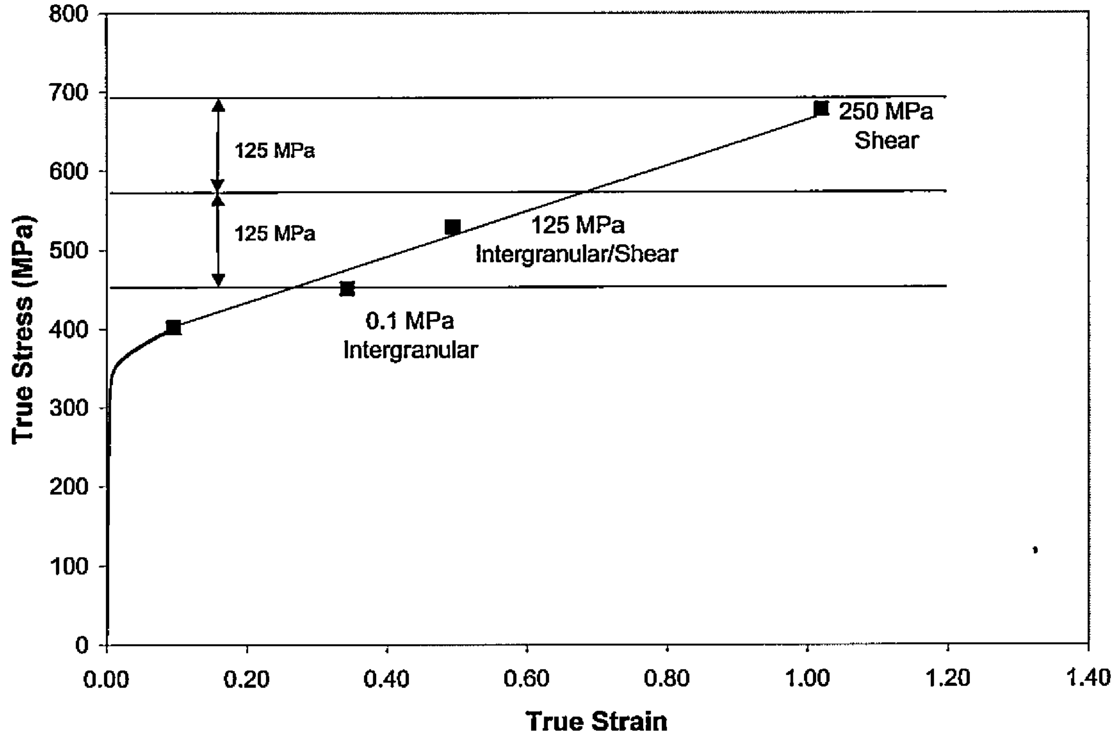

Figure 5.6: Fracture map for the low-Fe 6111 alloy in the T6 Temper. The intergranular fracture conditions are plotted as horizontal lines.

A further factor in the suppression of the intergranular fracture process is the effect of grain shape as it has been shown that the grain shape plays a large role on the stress required initiate intergranular fracture. In the work by Boyle et. al (2000), the intergranular fracture stress was modeled as a function of the grain shape. It was shown that once a crack was nucleated, its propagation was dependent on its ability to deflect at a triple point junction in order to follow the grain boundary. The intergranular fracture stress was given as:

$$\sigma_f = \frac{k_{cr}}{Q_1\sqrt{\pi a}} \qquad \text{Eqn. 5.5}$$

where k_{cr} is the critical stress intensity factor to propagate a crack through a kink of angle ϕ, a is the half crack length, and Q_1 is a function of the applied stress and is dependent on the strain path, Figure 5.7.

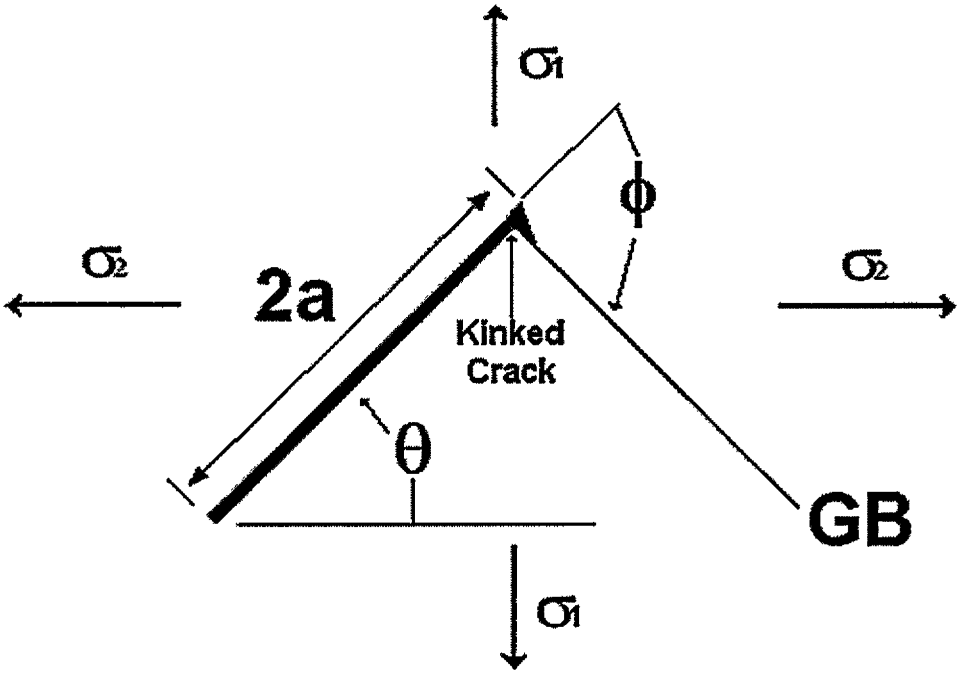

Figure 5.7: Geometry for the kinked crack intergranular model.

With increasing strain, the grains will elongate, and the angle ϕ will increase. As k_{cr} is dependent on ϕ, as it increases there will be an increase in the stress required to cause brittle intergranular fracture. In terms of the materials tested under pressure, this grain shape dependence will tend to increase the stress required for intergranular fracture to higher values with increasing strains. This then implies that a direct linear relationship between fracture stress and pressure is not appropriate, as it does not describe the full situation. A more realistic approach would be to take into account the effect of the change in grain shape with strain, such that:

$$\overline{\sigma} = \sigma_f(\phi) + P \qquad \text{Eqn. 5.6}$$

where σ_f will be dependent on the crack deflection angle ϕ, and $\phi \approx \phi(\varepsilon)$. Calculation of the length to width ratio for the grains near the fracture surface of the 0.1 and 250 MPa samples, gives values of 3.83 ± 0.14 and 7.82 ± 0.51 respectively. While these do not have a direct relationship with the crack deflection angle, ϕ, this change in aspect ratio will cause a significant increase in ϕ, and hence this effect will likely become important at the larger strains developed with the application of superimposed pressure.

When tested under superimposed pressures, no change in fracture mode is observed for the high-Fe samples. However, with the increase in ductility observed for the samples tested under pressure, there was a corresponding significant increase in fracture stress. It is interesting then to consider why with these large increases in fracture stress, do the high-Fe samples not fail by intergranular fracture. As with the tests at ambient pressure, the lack of a transition can be understood to be a result of the smaller grain size of the high-Fe alloy. In order to illustrate this effect, a plot of fracture stress versus the inverse root of grain size is shown in Figure 5.8. Of interest is the grain size dependence of the intergranular fracture stress. As this data wasn't available from this study, data for an Al-Mg-Si alloy was used (Evenson et al, 1975). This results in a series of lines of slope 2.37 MPa•m$^{-1/2}$, where the first line is drawn using the low-Fe T6 sample tested at 0.1 MPa as the reference. The remaining lines are then drawn, recalling the linear relationship of intergranular fracture stress with pressure. It can be seen that at all pressures tested, the high-Fe T6 samples fall well below their critical intergranular failure stresses. While the data presented is only approximate, it appears to be reasonably representative of the behaviour observed.

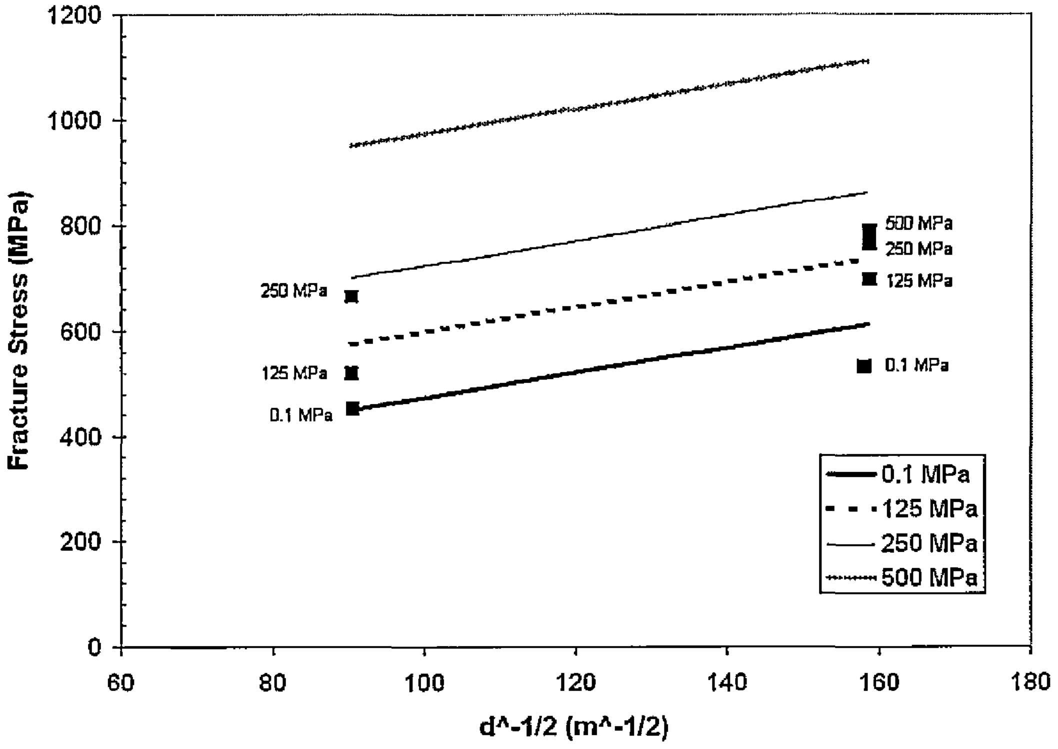

Figure 5.8: Plot showing the variation of fracture stress with grain size for the high-Fe6111 T6 alloys.

5.6 THE WORK HARDENING BEHAVIOUR FOR THE AA 6111 ALLOYS

Figure 5.9 shows plots of the $(d\sigma/d\varepsilon)/\mu$ versus $(\sigma - \sigma_y)/\mu$ for the 6111 alloys in both the T4 and T6 temper. At low strains, a difference in the work hardening rate is present for the samples in the T4 temper. With increasing strains however, the curves converge indicating that at large strains the work hardening becomes approximately the same for both materials, as observed in the extrapolated stress-stress curves for these samples, Figure 5.5. A more definite difference between the work hardening rates of the low and high-Fe T6 alloys is apparent, indicating the more pronounced effect grain size at higher yield strengths.

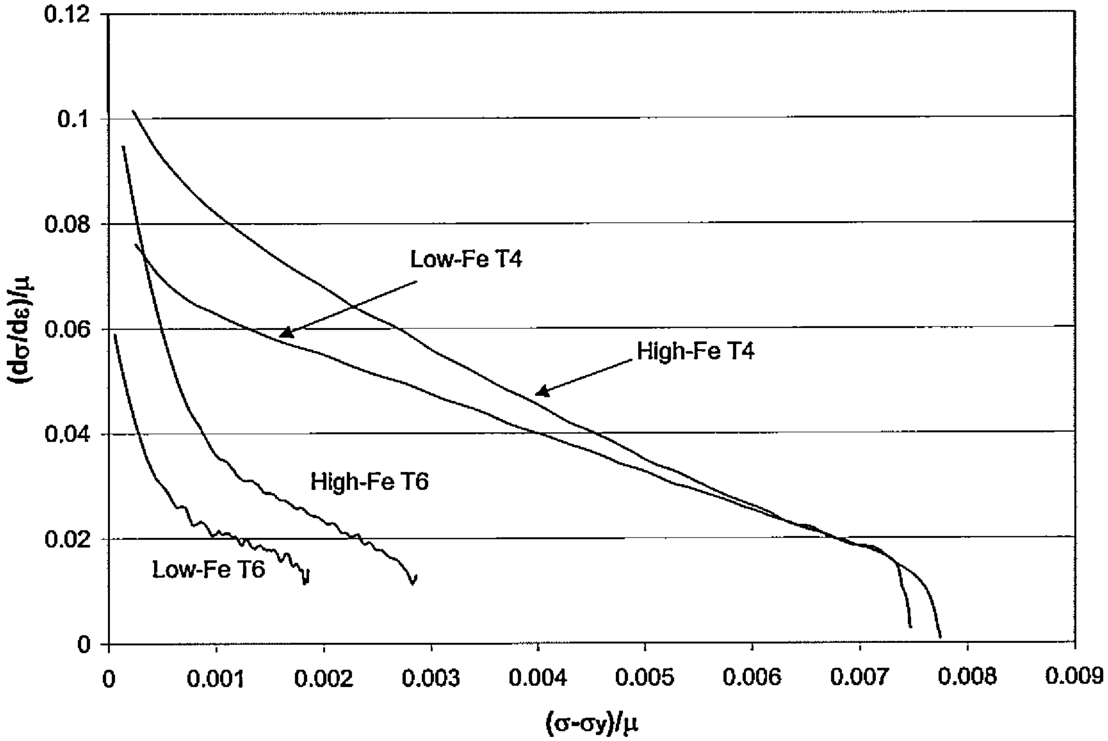

Figure 5.9: Plot showing the work hardening behaviour for 6111 alloys in the T4 and T6 temper.

6 CONCLUSIONS

The objective of this study was to characterize the damage evolution and fracture behaviour of AA 5754 and AA 6111 alloys with respect to their iron content, heat treatment and stress state.

The AA 5754 alloys demonstrated differences in fracture mode depending on the iron content tested, with the higher iron content exhibiting a reduced ductility. This was shown to be the result of the propensity of the high-Fe material with its corresponding high inclusion content to generate damage at lower strains, and as a result have localization occur in the form of coalescence of voids on a single shear band. When tested at 77K, the material was found to exhibit significantly less shearing and large sample scale shear bands were not observed. In addition, the uniform elongation for both iron contents when tested at 77 K increased by more than a factor of two. The change in fracture mode from cup and cone to shear MVC for the low-Fe sample when tested at 77 K shows the importance of the formation of macroscopic shear bands. Pressure was found to severely retard the formation of damage in these alloys, where at sufficient pressure, damage was all but eliminated.

The AA 6111 alloys tested in the T4 temper both failed by the shear MVC mode, with the low-Fe variant showing higher ductility. Ductility was found to increase with the application of superimposed pressure for both iron contents tested, corresponding to a reduction in the observable amount of damage. At sufficient pressures, damage was shown to be completely suppressed, and the samples failed by ductile rupture.

In the T6 temper an increasing iron content was observed to cause a change in fracture mode from intergranular to shear MVC when tested at ambient pressure. This was shown to be due to the difference in grain sizes between the two iron contents. When tested under pressure, the low-Fe variants fracture mode was observed to transition from intergranular fracture to shear MVC. Using a critical stress model for intergranular failure, it was shown that the flow stress level increases due to work hardening were insufficient to overcome the level of suppression on crack growth imposed on the material with superimposed pressure. In addition, the damage level was shown to decrease, which also delayed the nucleation of cracks allowing for increased deformation, resulting in more elongated grain geometry which is not conducive to intergranular fracture. In contrast, the high-Fe variant failed by MVC shear at all pressures. This was found to be the result of the more extensive damage formation due to the high-Fe-aluminide inclusion content, which allowed for localization to occur before a critical intergranular fracture stress was reached.

REFERENCES

Argon, A.S. and Im, J. (1975) Met. Trans. 6A, 839.

Ashby, M.F. (1966) Phil. Mag. 14, 1157.

Ashby, M.F. (1970) Phil. Mag. 21, 399.

Atkinson, J.D. (1973) Ph.D. Thesis, Cambridge University, England.

Baker, T.J. and Charles, J.A. (1971) in "Effects of Second Phase Particles on the Mechanical Properties of Steel", ISI Conf., Scarborough, England, 68.

Blum, J.I. and Morissey, R.J. (1966) Proc. 1st Int. Conf. on Fract., Sendai, Japan 3 1739.

Bridgman, P.W. (1952), Studies in Large Plastic Flow and Fracture, McGraw-Hill, New York.

Broek, D. (1971) in "A study of Ductile Fracture", Ph.D Thesis and NLR report TR 71021 U.

Brown, L.M. (1976) Proc. Conf. On Mech. And Phys. Of Fracture, Cambridge, England.

Brown, L.M. and Embury, J.D. (1973) Proc. 3rd Int. Conf. Strength of Metals and Alloys, Cambridge, England, 164.

Brown, L.M. and Stobbs, W.B. (1971) Phil. Mag. 23, 1201.

Brown, L.M. and Stobbs, W.B. (1976) Phil. Mag. 34, 351.

Brownrigg, A, Spitzig, W.A, Richmond, O, Teirlinck, D, and Embury J.D., (1983), Acta. Met, v. 31, n 8, 1141-1150.

Boyle, K.P, Embury, J. D., Perovic, D.D., Hood, J.E., (2000), Mathematical Modeling in Metals Processing and Manufacturing, METCOM.

Brooks, C. R. (1991) in "ASM Handbook Volume 4: Heat Treating", ASM International, Ohio, USA.

Burger, G.B., Gupta, A. K., Jeffrey, P. W., Lloyd, D. J. (1975) Materials Characterization, v. 35, n. 1, 23.

Carle, D. and Blount, G. (1999) Materials and Design, v. 20, 267.

Chin, G.Y., Hosford, W.F. and Backofen, W.W. (1964) Trans AIME, 230, 437.

Chung, N., Embury, J.D., Evensen J.D., Hoagland R.G., and Sargent C.M., (1977), Acta Met., v25, 377-381.

Dowling, J. M. and Martin, J.W. (1973) Proc. 3rd Int. Conf. Strength of Metals and Alloys, Cambridge, England, 170.

Esmaeili, S, Lloyd, D. J. and Poole W. J. (1999) TMS Annual Meeting and Exhibition, San Diego, California.

Evensen, J.D, Ryum, N., and Embury, J.D., (1975), Materials Science and Engineering, v. 18, 221-229.

Fisher, J.R. and Gurland, J. (1981) Met. Sci. 15, 185.

I.E. French and P.F. Weinrich, (1975), Metallurgical Transaction A, v. 6.

Ghandi, C. and Ashby, M.F. (1979). Acta Met.. 27, 1565.

Goods, S.H. and Brown, L.M., (1979), Acta Met., v27, page 1-15.

Gurland, J. and Plateau, J. (1963) Trans. ASM, 56, 442.

Hancock, J.W. and Mackenzie, A.C. (1976) J. Mech. Phys. Solids 24, 147.

J.J. Lewandowski, and P. Lowhaphandu, (1998), International Materials Reviews, v. 43, n. 4, 145-187.

LeRoy, G.H. (1978) Ph.D. Thesis, McMaster University, Hamilton, Canada.

D.S. Liu and J.J. Lewandowski, (1993), Metallurgical Transaction A, v. 24A.

Lloyd, J. and Gupta, A.K., Thermec '97, TMS.

Kawabata, T. and Izumi, O. (1976) Acta. Met. 24, 817.

Knott, J.F., and Cottrell, (1963), J. Iron Steel Inst., 201, 249.

Knott, J.F., (1966a), J. Iron Steel Inst., 204, 104.

Knott, J.F., (1966b), J. Iron Steel Inst., 204, 1014.

Knott, J.F., (1967), J. Iron Steel Inst., 205, 288.

Kocks, U. F., (1976) Journal of Materials Science and Engineering, v.98, 76-85

Martin, N. (1982) Master of Engineering Thesis, McMaster University, Hamilton, Canada.

McClintock, F.A., in "Ductility", Oct 14-15, 1967, 255-279.

McClintock, F.A. (1968) J. Appl. Mech. 35, 363.

Melander, A. (1980) Acta. Met. 28, 1799.

Miller, W.S., Zhuang, L., Bottema, J., Wittebrood, A.J., De Smet, P., Haszler, A. and Vieregge, A. (2000) Materials Science and Engineering, v. a280, 37.

Palmer, I.G. and Smith, G.C. (1966) in "Oxide dispersion strengthening", Gordon and Breach, New York, 253.

Pugh, H.L.D. and Green, D. (1964). Proc. Inst. Mech. Engrs. 179, 415.

Puttick, K.E. (1959). Phil. Mag. 4, 964.

Rice, J.R. and D.M. Tracy, (1969) Journal of the Mechanics and Physics of Solids, v17, 201.

Rogers, H.C. (1960) Trans. AIME 218, 498.

Rogers, H.C., in "Ductility", Oct 14-15, 1967, 31.

Rosenfield, A.R. (1968) Metall. Reviews, I3, 29.

Ryder, R. A. and Smale, A. C. (1963) in "Fracture of Solids", eds. DC Drucker and J. J. Gilman, Interscience, New York.

Sarkar, J., Kutty, T.R., Wilkinson, D.S., Embury, J.D., Lloyd, D. J., (2000) Materials Science Forum, v. 331-337, part 1, 583.

Schmitt, K.H. and Jalinier, J.M. (1982) Acta. Met. 30, 1789

K. Spencer, (2000) Masters thesis, University of Waterloo, Ontario, Canada.

Tanaka, K., Mori, T. and Nakamura, T. (1970) Phil. Mag. 21, 267.

D. Teirlinck, (1983) Ph.D. thesis, McMaster University, Ontario, Canada.

Thomason, P.F. (1968) J. Inst. Metals, 98, 360.

Thomason, P.F. (1971) Metal Science Journal, 5, 64.

Thomason, P.F. Ductile Fracture of Metals, Pergamon Press, Toronto, 1990.

Vasudevan, A.K. and R.D. Doherty, (1987) Acta Met., v35, no.6, page 1193-1219.